Hybridisatie van snelle multipooltechnieken en geometrische optica
voor het modelleren van grote elektromagnetische problemen

Hybridization of Fast Multipole Techniques and Geometrical Optics
for the Modeling of Large Electromagnetic Problems

Giorgos Karagounis

Promotoren: prof. dr. ir. D. De Zutter, prof. dr. ir. D. Vande Ginste
Proefschrift ingediend tot het behalen van de graad van
Doctor in de ingenieurswetenschappen: toegepaste natuurkunde

UNIVERSITEIT
GENT

Vakgroep Informatietechnologie
Voorzitter: prof. dr. ir. D. De Zutter
Faculteit Ingenieurswetenschappen en Architectuur
Academiejaar 2016 - 2017

ISBN 978-90-8578-934-5
NUR 928, 959
Wettelijk depot: D/2016/10.500/65

Hybridization of Fast Multipole Techniques and Geometrical Optics for the Modeling of Large Electromagnetic Problems

Giorgos Karagounis

Dissertation submitted to obtain the academic degree of
Doctor of Engineering Physics

Publicly defended at Ghent University on September 30th, 2016

Research funded by Research Foundation Flanders (FWO)

Supervisors:

prof. dr. ir. D. Vande Ginste
prof. dr. ir. D. De Zutter
Electromagnetics group
Department of Information Technology
Faculty of Engineering and Architecture
Ghent University
Technologiepark-Zwijnaarde 15
Ghent, Belgium
intec.ugent.be

Members of the examining board:

prof. dr. ir. H. Van Landeghem (chairman)	Ghent University, Belgium
prof. dr. ir. J. Fostier (secretary)	Ghent University, Belgium
prof. dr. ir. D. Vande Ginste (supervisor)	Ghent University, Belgium
prof. dr. ir. D. De Zutter (supervisor)	Ghent University, Belgium
prof. dr. dipl. ing. T. Eibert	Technische Universität München, Germany
prof. dr. ir. C. Craeye	Université Catholique de Louvain, Belgium
prof. dr. ir. J. Beeckman	Ghent University, Belgium

FACULTY OF ENGINEERING AND ARCHITECTURE

INTEC

UNIVERSITEIT GENT

"Clarity and consistency are not enough:
the quest for truth requires humility and effort."

Tariq Ramadan

Acknowledgment

After four years of academic research, with the end clearly in sight, it is important to answer the question what a PhD has been to me and has encompassed for me. Most importantly, it is not a study program at the university, the only similarity being obtaining a degree at the end. It all started by addressing a rather broad research question. The solution could not be found in a course book that is neatly categorized into chapters by a professor. Instead, there was a tremendous amount of academic literature available, evolving at a pace almost too fast to follow, in which similar questions are partly answered. The strengths I possessed when I started was the knowledge, yet premature for tackling the research question, acquired during my studies and my two very helpful supervisors who guided me to the directly relevant works in between that humongous amount of choices. The gross part of this full-time job consisted of a cyclical process of obtaining some results, directly leading to new challenges, discussing with colleagues about it, meeting with the supervisors, re-evaluating my work and obtaining new results. The few wonderful eureka-moments made it all worth. When the results became sufficiently convincing, I dissipated the newly acquired knowledge among the scientific community through the publication of journal papers and presentations at academic conferences, always supported by my two supervisors and in collaboration with colleagues. Now and then, I got some welcome distraction by assisting exercise classes for undergraduate students. During the last year, I built further on the foundation that was laid during the first three years and I want to believe that I contributed to the quest of others with the knowledge accumulated by my work. In short, it was a struggle that resulted in the creation of new knowledge, continuously in collaboration with different people. The people around me have been very important and therefore I would like to thank them here in more detail.

First and foremost, I would like to thank my two supervisors, prof. Daniël De Zutter and prof. Dries Vande Ginste. Both were always prepared to listen to concerns about the research and actively helped where needed. I am very happy to have had the chance to work with prof. De Zutter, an authority in electromagnetics. This work would not have been possible without your input, especially on the theoretical part. Moreover, the speed with which I received your comments on my reports and articles is exceptional. For all my immediate concerns, I could count on the readiness of prof. Vande Ginste. Even for minor questions I could count on your help. Your comments on the wording used in our journal papers proved valuable lessons to me for life.

I had the chance to work within a pleasant group of young scientists. Special

thanks goes to my genius colleague and friend Zdravko. You always had a paper or book in mind to refer to when I posed you a question. Even when I challenged your knowledge of mathematics, you carefully listened and provided me with a novel vision on the issue. Besides your professional excellence, I discovered in you a kind-hearted and sociable person. You entertained us with your company, when you debated about subjects ranging from the philosophy behind Kung-Fu Panda to Russian politics. The days you and your friends showed us Belgrade were unforgettable. Further, I wish you all the best with your grand personal ambitions.
Marco, you were undoubtedly the social glue during and after the working hours. I enjoyed the daily coffee, the snooker evenings and the REAL Italian dinners followed by board games. Not only this, but you have also influenced for the better my inner world by your literary suggestions.
My sincere respect goes to Gert-Jan. You were always available for questions related to math or even to debugging. You are a great listener and an even better problem solver, which was also an important asset during the robot competition we participated in. I wish you all the best in your new professional life.
Nickolay, you are one of the most exceptional persons I have ever met. You consistently endorsed the positive aspects of many colleagues, while challenging some deeply rooted conceptions in our world view. Even in times of great distress, your good mood remained mostly unaltered. I experienced your discussions as humorous and liberating at the same time. You are the real-life version of prince Myshkin in the best sense. May the universe prove optimal for you.
An old Greek saying goes νοῦς ὑγιής ἐν σώματι ὑγιεῖ, i.e. a sound mind in a sound body. Arne, you are a good example of this saying. I was glad to run the first few hundred meters of the Antwerp 10 miles with you, before you accelerated to end within the top 1% of the runners. At work, our discussions on the implementation of PML layers were valuable.
The regular coffee breaks, on initiative of Marco, proved necessary to remain concentrated for the rest of the day. I would like to thank the people participating: il dottore Luigi, Paolo, Joachim, Sam Agneessens, Domenico, Patrick and Annelies for the very broad and fruitful conversations.
Further I would like to thank all my colleagues for the interesting discussions in the office, during lunch breaks and during the weekly international Thursdays: Freek, Bart Michiels, Ignace, Yves, Dieter, Thomas Cuyckens, Martijn, Michiel, Simon, Berg, Niels, Dries, Thijs, Sam Lemey, Irven, Olivier, Thomas Deckmyn and Bart Coppens. Work, first at the Technicum and then at the iGent tower, would not have been the same without you.

Outside of work, I enjoyed the company of many other friends, for which I am very thankful. Running with Laurens and Kevin has been a great way to move my thoughts when I was facing the many challenges that go together with research. Mathieu, I especially liked our regular running moments. Kristof, thank you for the evenings playing snooker and for the many discussions at

occasion. I also had a pleasant time in the company of many other people during weekend evenings or even weekends on location. Thank you for this Brecht, Ewaut, Kianoush and Elke, Gertjan, Michiel and Evelien, Ann-Sophie, Paulien, Kirsten, Lisa and Stijn, Nele, Barbara, Evy and Alexander, Rinus, Kim, Liselot and Karel, Tinfong and Tom, Thijs and Evelien, and Jelle.

The last words are reserved for the people closest to me, my family. The life-long bond that we have is strong and has forever been one of my driving forces to progress in life and thus also in professional life. First of all, I would like to thank παππούς in memoriam, that nourished my intellectual world with the hour-long, and sometimes day-long, discussions on philosophy and science. My professional choices in life greatly benefited from these moments of unstrained intellectual thinking. Also I would like to thank γιαγιά Mimi for constantly showing interest in the progress of my work and for memorizing the long words in the title of my PhD thesis. Γιαγιά Κουλά, σε ευχαριστώ που πάντα βρίσκω την πόρτα του σπιτιού σου ανοιχτή και που με περιποιείσαι σαν γιο όταν έρχομαι στην Ελλάδα. Κοντά σε σένα, μαζί με την υπόλοιπη οικογένεια, βρίσκω χαρές που αλλού δεν υπάρχουν. Many thanks to you as well, Eddy and Angeline, for the nice moments during barbecues and dinners and for your readiness to help where needed. André, the summers in Tavira and the moments I spent with you and the amazing community you have founded there remain in my memory. Sander and Hilde, thank you for taking care of the library of παππούς, it means a lot to me.
Andreas, even though our interests are very different, you keep being intrigued by my work and you remain critical in our discussions, which helps me keep an open mind. I look forward to many more of these discussions. Evelyn, thank you for the pleasant company during our family gatherings.
Πατέρα, we do not often get a chance to meet, but you have followed me these last few years by regular telephone calls and have been supportive towards my professional choices. I enjoy our conversations, especially during holidays, where I find rest by your side. Many thanks to you too, Liana, for making me feel welcome as your own son in your house. Your witted comments during our discussions have had an important added value for me.
Μητέρα, I lack the words to properly thank you. Your dedication when it comes to Andreas and me has been and still remains remarkable. I can only say that whatever I have achieved and may achieve in the future has been to great extent the result of the education that you provided us. Not in terms of knowledge, but in terms of kindness, generosity and a positive ambition, in short the ingredients of happiness.

The very last sentences are reserved for you Britt. Since I met you, more than eight years ago, we have grown very close. When it comes to my research, you were always prepared to listen to my worries. You comforted me during hard times and helped me with your sharp practical view. Your help, from finding the correct words in my writings to the practical arrangements for the

public defense these days, has been of primordial importance. But of course there is so much more than that. I enjoy your presence at the many events with our friends, in which you often play a central role. Your dedication in making time for the two of us is remarkable. I truly savor both the calmness and the discussions during our walks. Your smile makes me smile. Don't ever lose it.

Ghent, September 2016
Giorgos Karagounis

Contents

Samenvatting

De doelstelling van dit werk is de ontwikkeling van een hybride modelleringstechniek om heel grote elektromagnetische (EM) problemen te simuleren. Hiertoe wordt de vlugge multipooltechniek (*Multilevel Fast Multipole Methods*, MLFMM) gecombineerd met stralentrek. MLFMM is een efficiënte exacte numerieke methode, onder meer geschikt om de oplossing van EM verstrooiingsproblemen die klassiek worden aangepakt aan de hand van randintegraalvergelijkingen (*Boundary Integral Equations*, BIE) en de momentenmethode (*Method of Moments*, MoM) drastisch te versnellen. Maar zelfs met deze efficiënte methode worden voor extreem grote problemen de computationele vereisten, d.i. de tijdsduur van de simulatie en het nodige geheugen, te groot voor de hedendaags beschikbare computerinfrastructuur. In dat geval opteert men vaak om het probleem met stralentrek te bestuderen, zoals door gebruik te maken van uniforme diffractietheorie (*Uniform Theory of Diffraction*, UTD). Hiermee hangen de computationele vereisten niet af van de grootte van het probleem, maar van het aantal objecten dat aanwezig is in het simulatiedomein. Stralentrek is echter slechts een benaderende methode en de foutmarge op de oplossing is onbekend. Hoewel de oplossing belangrijke fysische inzichten kan opleveren, moet ze dus steeds met de nodige voorzichtigheid geïnterpreteerd worden. De combinatie van MLFMM en UTD tot een hybride MLFMM-UTD methode laat toe om kritieke delen in grote simulatiedomeinen, zoals antennes, zeer nauwkeurig in rekening te brengen, terwijl de minder kritieke interacties met grote objecten in de omgeving, bv. muren, andere grote reflecterende objecten of de grond (de zogeheten *canonische objecten*), efficiënt worden benaderd.

Hybride MoM-UTD bestaat reeds tientallen jaren en is aanwezig in commerciële softwarepakketten. Het deel van het probleem dat nauwkeurig moet behandeld worden, wordt in kleine segmenten opgedeeld (*gediscretizeerd*) zoals in klassieke MoM. De onderlinge interacties tussen de segmenten wordt beschreven door een lineair systeem vergelijkingen, gekarakteriseerd door een interactiematrix. Interacties die te wijten zijn aan de aanwezigheid van canonische objecten worden met behulp van UTD in rekening gebracht in de interactiematrix. De MoM-UTD methode kan verder versneld worden door het gebruik van MLFMM. De combinatie van MLFMM met UTD is echter tot op heden slechts beperkt onderzocht. De manier waarop UTD moet toegepast worden op een typisch MLFMM geaggregeerd stralingspatroon is niet duidelijk. Een belangrijke bijdrage hiertoe is geleverd door Tzoulis & Eibert. Zij gebruikten de snelle verre-veld benadering (*Fast Far-Field Approximation*, FAFFA), een hoog-frequente benadering in MLFMM, om het stralingspatroon te reduceren tot een enkele vlakke golf. Hierop kan dan UTD rechtstreeks toegepast worden. Deze hybride methode

leverde reeds goede resultaten op. Het blijft echter moeilijk te voorspellen wat de nauwkeurigheid van deze methode is ten opzichte van een MoM-UTD hybride methode na het doorvoeren van de FAFFA vereenvoudigingen, in het bijzonder wanneer de gediscretizeerde objecten in de schaduw liggen van een groter object dat in rekening wordt gebracht met UTD.

Daarom hebben we in dit werk onderzocht hoe UTD zonder vereenvoudigingen binnen een MLFMM kader kan gebruikt worden. In Hoofdstuk 3 wordt een methode beschreven om UTD te veralgemenen naar willekeurige bronnen. Hiertoe worden equivalente bronnen op de rand rond de willekeurige bron ingevoerd. Door bovendien het bronveld buiten de bronregio en het gediffracteerde veld binnen de regio waarin het gediffracteerde veld gekend moet zijn te expanderen in multipolen, hebben we een nieuwe set coëfficiënten ingevoerd die de koppeling tussen de twee multipoolexpansies beschrijft. Deze UTD methode voor willekeurige bronnen vormt niet alleen een theoretische basis voor de hybridisatie van UTD en MLFMM, het biedt ook de mogelijkheid om de, reeds vaak gebruikte, UTD methode toe te passen op meer realistische problemen. We hebben deze methode gebruikt om de diffractie te bestuderen van (hogere-orde) Hermite-Gaussische bundels aan een perfect elektrisch geleidende (*Perfectly Electrically Conducting* (PEC)) wig en een spleet in een vlakke PEC plaat.

In Hoofdstuk 4 wordt dan een praktische MLFMM-UTD implementatie voorgesteld die reflecties aan het oppervlak en diffracties aan scherpe hoeken van canonische objecten in rekening brengt zonder de canonische objecten te discretizeren. Ten eerste, wat betreft reflecties aan PEC oppervlakken, gebruiken we het principe van beeldbronnen. Deze methode is bruikbaar in MLFMM zonder dat de computationele complexiteit toeneemt en is exact. Ten tweede worden diffracties in rekening gebracht door de toepassing van de veralgemeende UTD methode beschreven in Hoofdstuk 3. Hiervoor wordt een nieuwe MLFMM translatiematrix ingevoerd die gerelateerd is aan de koppelingscoëfficiënten van de veralgemeende UTD methode. Deze translatiematrix is vol, in tegenstelling tot diagonale translatiematrices in traditionele MLFMM implementaties. Door de interactie via diffractie niet te beschrijven op de klassieke MLFMM wijze, maar te laten afhangen van de afstanden van de objecten tot het intermediair diffractiepunt, is het toch mogelijk om de computationele complexiteit laag te houden indien de gediscretizeerde verstrooiers sterk opgevulde volumetrische verstrooiers zijn. Daarenboven kan ook een asymptotische benadering voor de translatiematrix worden doorgevoerd. Op deze manier blijft de computationele complexiteit van MLFMM tevens behouden voor ijle oppervlakteverstooiers. De kost hiervoor is het verlies van nauwkeurigheid vanwege de asymptotische benadering. Interessant is dat de nulde-orde asymptotische benadering opvallende gelijkenissen vertoont met de MLFMM-UTD methode van Tzoulis & Eibert. De goede nauwkeurigheid van onze methode ten opzichte van traditioneel MLFMM is aangetoond voor twee hoornantennes waarvoor de rechtstreekse communicatie wordt versperd door een groot canonisch object. Onze methode

is ook gebruikt om de velden rond twee grote antenne-arrays opgebouwd uit zogeheten *fotonische kristallen* te modelleren, waar opnieuw een groot object het rechtstreekse communicatiekanaal verspert.

De hybride oplossingsmethoden in dit werk zijn uiteraard slechts toepasbaar indien de aanwezigheid van grote objecten in het simulatiedomein in rekening kan worden gebracht met behulp van UTD. Hoewel er aanzienlijke vooruitgang is geboekt om theoretische UTD oplossingen te formuleren voor een aantal canonische objecten, is het aantal configuraties toch nog beperkt. In Hoofdstuk 5 richten we daarom onze aandacht op het ontwikkelen van een methode om UTD oplossingen op numerieke wijze te verkrijgen voor willekeurige configuraties. De grote uitdaging hierbij is dat canonische objecten vaak oneindig uitgestrekt verondersteld zijn in een bepaalde richting en dus getrunceerd moeten worden om ze met een numerieke methode te kunnen behandelen. Dit kan leiden tot onnauwkeurigheid en/of inefficiëntie. Daarom wordt in dit werk voorgesteld om een perfect aangepaste laag (*Perfectly Matched Layer*, PML) in een momentenmethode toe te voegen, zodat de invloed van de getrunceerde zijde zoveel mogelijk gedempt wordt. Het invoeren van de PML laag gebeurt door de gepaste cartesische coördinaten te "strekken" in het complexe vlak. De werking van de code wordt bevestigd aan de hand van het canonische voorbeeld van een wig en tevens toegepast op het bestuderen van de koppeling van bundels met verschillende polarizaties in een polarizatiebundelsplitser. Het numeriek bepalen van UTD oplossingen kan een onderwerp zijn voor toekomstig onderzoek.

De resultaten die in dit werk meegedeeld worden dragen bij tot de kennis over het numeriek oplossen van hoogfrequente verstrooiingsproblemen gebruikmakend van MLFMM. Dankzij de hybridisatie met stralentrek wordt een aanzienlijke vermindering van computationele tijd- en geheugenvereisten bewerkstelligd. De voorgestelde methodes zijn onmiddelijk toepasbaar op grote EM problemen en de nieuwe theoretische inzichten zijn nuttig bij het ontwikkelen van nieuwe simulatiepakketten. De verdere stappen die hiervoor nodig zijn, worden beschreven in het laatste hoofdstuk.

Summary

The aim of this work is the development of a hybrid modeling technique to simulate very large electromagnetic (EM) problems. To this end, the Multilevel Fast Multipole Method (MLFMM) is combined with ray tracing. MLFMM is an efficient exact numerical method, i.a. suitable to drastically accelerate the solution of EM scattering problems that are traditionally dealt with via a Boundary Integral Equation (BIE) and Method of Moments (MoM) approach. But even with this efficient method, when considering extremely large problems, the computational requirements, i.e. the simulation time and the memory consumption, become unacceptably high with the currently available computer architecture. In this case, one often opts to study the problem via ray tracing, e.g. by using the Uniform Theory of Diffraction (UTD). Then, the computational requirements do not depend on the size of the problem, but on the number of objects that are present in the simulation domain. However, ray tracing is only an approximate method and the error on the solution is unknown. Although the solution can yield valuable physical insights, it always needs to be treated with caution. The combination of MLFMM and UTD into a hybrid MLFMM-UTD method allows accounting for critical parts in large simulation domains, such as antennas, in a very accurate way, whereas the less critical interactions with large objects in the environment, e.g. walls, other large reflecting objects or the floor (the so-called *canonical objects*), are efficiently approximated.

Hybrid MoM-UTD already exists for several decades and it is available in commercial software. The part of the problem that needs to be treated accurately is discretized into small segments, similarly to classic MoM. The mutual interactions among these segments are described by a linear system of equations that is characterized by an interaction matrix. Interactions resulting from the presence of canonical objects are taken into account by UTD in the interaction matrix. The MoM-UTD can be further accelerated by use of MLFMM. At present, the number of reported investigations on the combination of MLFMM and UTD is rather limited. It is still unclear how to apply UTD onto a typical MLFMM aggregated radiation pattern. An important contribution has been provided by Tzoulis & Eibert. They used the Fast Far-Field Approximation (FAFFA), a high-frequency approach of MLFMM, to reduce the radiation pattern to a single plane wave. UTD can then be applied directly. Their hybrid method already provides satisfactory results. Nevertheless, owing to the FAFFA approximations, it remains hard to predict the accuracy of this method, compared to a MoM-UTD and in particular when the discretized objects reside in the shadow of a large canonical object.

Therefore, in this work, we investigate how UTD can be leveraged within an MLFMM framework without simplifications. In Chapter 3, a method is described to generalize UTD to arbitrary sources. To this end, equivalent sources are introduced on the boundary surrounding the arbitrary source. Furthermore, by expanding the source field outside the source region and the diffracted field inside the observation region of interest into multipoles, we introduce a new set of coefficients that describe the coupling between the two multipole expansions. This UTD method for arbitrary sources does not only constitute a theoretical basis for the hybridization of UTD and MLFMM, it also offers the possibility to apply the already very popular UTD method to more realistic problems. We use this method to study the diffraction of (higher-order) Hermite-Gaussian beams on a Perfectly Electrically Conducting (PEC) wedge and a slit in a flat PEC plate.

In Chapter 4, a novel MLFMM-UTD method is presented that takes reflections at the surface and diffractions at sharp edges of canonical objects into account without discretization of the canonical objects. First, concerning reflections at PEC surfaces, we use the principle of image sources. This method is applicable in MLFMM without increasing the computational complexity and, furthermore, is exact. Second, diffractions are taken into account by the application of the generalized UTD method described in Chapter 3. A new MLFMM translation matrix is introduced that is related to the coupling coefficients of the generalized UTD method. The translation matrix is full, in contrast to the diagonal translation matrix in traditional MLFMM schemes. However, by not describing the interaction via diffraction in the classical MLFMM sense, but by letting it depend on the distance between the objects and the intermediary diffraction point, it is possible to maintain the low computational complexity for densely filled volume scatterers. Moreover an asymptotic approximation can be introduced for the translation matrix. In this way, the computational complexity of MLFMM is also retained for sparse surface scatterers. This comes at the cost of a decreased accuracy. Interestingly, the zeroth-order asymptotic approximation exhibits remarkable resemblance with the MLFMM-UTD method of Tzoulis & Eibert. The good precision of our novel method, compared to traditional MLFMM, is demonstrated by investigating two horn antennas, for which the direct communication is blocked by a large canonical object. Our method is also used to model the fields in the neighborhood of two large antenna arrays, consisting of so-called *photonic crystals*, where again a large object obstructs the direct communication channel.

The hybrid methods, advocated in this dissertation, are of course only applicable when the presence of large objects can be taken into account by means of UTD. Although considerable progress has been achieved in formulating theoretical UTD solutions for a number of canonical objects, that number still remains limited. Therefore, in Chapter 5 we focus on the development of a method to obtain numerical UTD solutions for arbitrary configurations. The

great challenge here lays in the fact that canonical objects are often assumed to be infinitely extended in one direction and thus need to be truncated so that they can be studied by numerical methods. This may lead to loss of accuracy and/or inefficient simulations. In Chapter 5, we propose to incorporate a Perfectly Matched Layer (PML) in the MoM to damp the influence of the truncated side. The introduction of a PML layer is achieved by "stretching" the pertinent Cartesian coordinates into complex space. The code is validated by means of a canonical example of a wedge and, moreover, it is applied to study the coupling of beams of different polarizations in a polarization beam splitter. The numerical derivation of UTD solutions remains a subject of future research.

The results presented in this work contribute to the knowledge on numerical methods to solve high-frequency scattering problems by means of MLFMM. Thanks to the hybridization with ray tracing, a considerable reduction in computational time and memory requirements is achieved. The presented methods are directly applicable to large EM problems and the theoretical insights are useful for the development of novel simulation methods that may constitute the core of commercial software. The necessary steps to this end are described in the final chapter.

List of Publications

Articles in International Journals

- G. Karagounis, D. De Zutter, and D. Vande Ginste, "Computation of the Diffraction from Complex Illumination Sources in Extended Regions of Space", *Optics Express*, vol. 21, no. 25, pp. 30 379–30 391, 2013.
- G. Karagounis, D. De Zutter, and D. Vande Ginste, "A Hybrid MLFMM-UTD Method for the Solution of Very Large 2-D Electromagnetic Problems", *IEEE Trans. Antennas Propagat.*, vol. 64, no. 1, pp. 224–234, 2016.

Articles in Conference Proceedings

- G. Karagounis, D. Vande Ginste, and D. De Zutter, *Combining MLFMM and UTD for Solving Large 2-D Scattering Problems*, Poster presented at URSI Benelux Forum, November 18^{th}, Université Catholique de Louvain, Belgium, 2014.
- G. Karagounis, D. De Zutter, and D. Vande Ginste, "A Generalized Uniform Theory of Diffraction Method for Complex Illumination Sources Accounting for Multiply-Diffracted Rays", in *Computational Electromagnetics International Workshop (CEM) in Izmir, Turkey*, 2015, pp. 1–2.
- G. Karagounis, D. De Zutter, and D. Vande Ginste, "An Efficient 2-D MLFMM-UTD Hybrid Method to Model Non-Line-of-Sight Propagation", in *International Conference on Electromagnetics in Advanced Applications (ICEAA) in Turin, Italy*, 2015, pp. 82–85.

Articles submitted to International Journals

- G. Karagounis, D. De Zutter, and D. Vande Ginste, "Full-wave Simulation of Optical Waveguides via Truncation in the Method of Moments Using PML Absorbing Boundary Conditions", *Optics Express*, submitted, 2016.

- G. Karagounis, D. De Zutter, and D. Vande Ginste, "Numerical Derivation of Diffraction Coefficients Using a Method of Moments with Incorporated Absorbing Boundaries", *IEEE Antennas Wireless Propag. Lett.*, submitted, 2016.

Hybridization of Fast Multipole Techniques and Geometrical Optics for the Modeling of Large Electromagnetic Problems

1

Introduction

Electromagnetic modeling

It is hard to miss the presence of electronic devices in our daily lives. Antennas are mounted on top of the buildings, inside offices we notice WiFi routers, in the car we absently follow the instructions of the GPS and, last but not least, people are using their smartphones constantly around us.
Due to the complexity of the present electronic devices, computational tools are mandatory to design them and to test their performance in the presence of complex surroundings, preferably even before the production stage. Such computational tools employ the physical laws that govern the device to predict how it will perform in reality. In particular, for the case of electronic devices, this requires the simulation of the electromagnetic fields that are excited by currents and charges and their interaction with the materials surrounding the device. The physical laws describing that interaction are Maxwell's equations [1]. The numerical study of electromagnetic fields by means of computers is called electromagnetic modeling and is the subject of the domain of computational electromagnetics.
Due to the immense diversity in size of the devices and environments under consideration (e.g. a mobile device vs the scattering at a military aircraft), different simulation techniques exist, each with advantages that make it suitable for a particular kind of simulations. In this work, two different simulation techniques are combined to create a novel hybrid scheme. The two classes of methods are briefly introduced in this chapter, followed by an outline of this dissertation.

Geometrical optics

In geometrical optics (GO) [2], the electromagnetic (EM) field is described in terms of rays. Each ray interacts individually with the materials it encounters on its path. The success of GO relies on the fact that scattering is a local phenomenon at high frequencies, i.e. scattering depends only on the value of the field and the geometry of the scattering object at the scattering point.

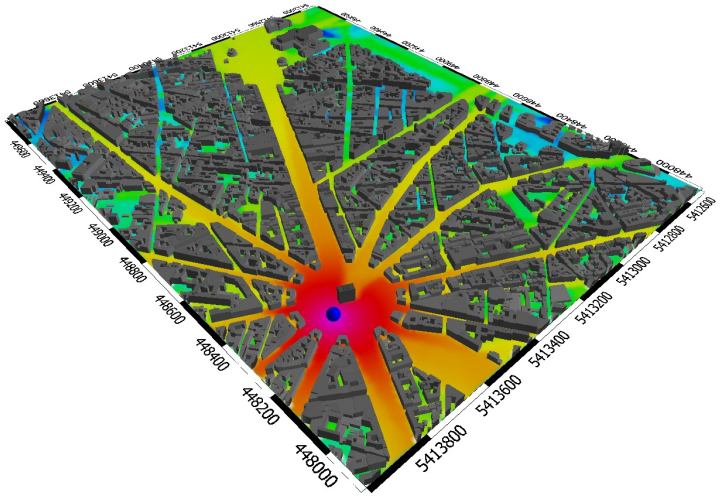

Figure 1.1: The propagation of the electromagnetic field in Paris for an antenna near the Arc de Triomphe, based on a geometrical optics simulation tool [3].

The ray description of high-frequency EM fields (e.g. light) provides a vivid physical picture for radiation and scattering. Several physical phenomena, such as direct illumination, reflection at metallic surfaces and refraction at dielectric interfaces are understood in terms of rays for more than a century. The application domain of GO drastically increased with the introduction of the Geometrical Theory of Diffraction (GTD) by Joseph Keller in 1953 [4], as it allowed describing diffraction at sharp edges in terms of rays. For example, the path traversed by a diffracted ray still has the extremal length of all possible paths passing through the diffraction point, an application of the well-known Fermat's principle that states that a ray always follows the stationary path between source and observer. Together with the Uniform Theory of Diffraction (UTD) [5], which resolves some singularity issues in the GTD solution, diffraction at a multitude of so-called canonical geometries, such as one or more wedges formed by two straight or curved faces and vertices formed at the intersection of three straight or curved faces, has been understood in terms of rays.

At the time of the development of GTD and later on, there was a considerable interest in tools that could describe scattering at complex targets such as aircrafts, missiles, satellites, naval ships, etc. With the advent of computers, the first UTD based simulation tools were developed at Ohio State University at the beginning of the 80s [6]. In the meantime, numerical tools that employ UTD for very complicated structures, used during computer-aided design (CAD), are also available [7]–[9]. Fig. 1.1 shows the result of such a simulation tool for a complex scattering problem in Paris, with an antenna placed close to the Arc De Triomphe.

Boundary element methods

At lower frequencies, the ray description of the EM fields is not valid. The EM fields are governed by a set of differential equations, namely the Maxwell equations. From these equations, the wave equation for homogeneous materials can be derived. To model the EM field exactly, the wave equation needs to be solved. There are several classes of methods to achieve this goal. One decomposes the region of interest into small volumes and imposes a weak formulation of the differential equations over each of these volumes. Such methods are called finite element methods [10]. Other techniques are used for piecewise homogeneous materials, discretize only the boundaries between the materials into segments and impose an appropriate boundary condition. These boundary element methods, often called the Method of Moments (MoM) in the EM community [11], are used in this work.

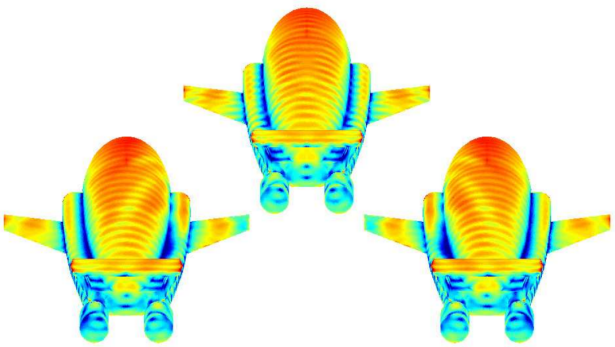

Figure 1.2: Current density on a formation of three Thunderbird planes, computed using a boundary element method [12].

Instead of directly solving the Maxwell equations, in MoM, an equivalent boundary integral equation (BIE) is solved. This allows one to discretize only the

boundaries between every pair of homogeneous materials, which drastically lowers the numbers of unknowns in problems with a low surface-to-volume ratio, as compared to finite element methods. The discretized version of the integral equation leads to a matrix equation that is solved by a computer. The disadvantage is that the pertinent interaction matrix is densely filled, in contrast to the sparse matrix systems that are typical for finite element methods. Consequently, for a system with N unknowns, the time and memory requirements scale as $\mathcal{O}\left(N^2\right)$ for increasing N. The Fast Multipole Method (FMM) [13] and its multilevel version (MLFMM) [14] are able to lower the scaling of the resources to $\mathcal{O}(N \log N)$. This has already led to the rigorous simulation of electrically large structures such as planes, as shown in Fig. 1.2. Recently, two problems involving billions of unknowns were solved on the Tier 1 supercomputer of Ghent University by means of MLFMM [15].

Goal and outline of this dissertation

Even with the very efficient scheme of MLFMM, extremely large scattering problems such as, e.g., the propagation of EM fields in an urban environment are impossible to model as the discretization of the entire region of interest becomes intractable. Such problems are nowadays modeled via ray-optical approaches that avoid the discretization of the simulation domain. This is however only possible if the different objects in the simulation domain can be approximated by a combination of canonical structures, for which a GO solution is available. This is the case for walls, doors, etc. When the domain also contains objects with fine details (such as, e.g., antennas), which should be treated as accurately as possible, a hybrid MoM-UTD is employed, as shown in Fig. 1.3 by the uppermost gray arrow. A MoM-UTD solver discretizes objects consisting of fine details, thus allowing one to accurately model the currents on these critical parts, while also taking the presence of large objects into account by using the canonical solutions from GO and UTD. As such, the discretization of only a small part of the simulation domain is required.

In this work, we develop a hybrid MLFMM-UTD solver to exploit the efficient scheme of MLFMM (red arrow in Fig. 1.3). This further reduces the computational requirements. Unlike the MoM-UTD method, in which the UTD canonical solution can easily be integrated into the computation of the interaction matrix, the hybridization of UTD with MLFMM requires an extension of UTD to general excitation sources. This in turn leads to the development of a MLFMM-UTD hybrid scheme by introducing a new MLFMM translation matrix. The translation matrix is, unlike conventional MLFMM, a full matrix. Only after a careful organization of the MLFMM interactions the scaling of the resources remains $\mathcal{O}(N \log N)$ for a certain class of problems. Further, to account for more complex scatterers using UTD, the diffraction coefficients of intricate (canonical) configurations need to be known. Via a novel MoM

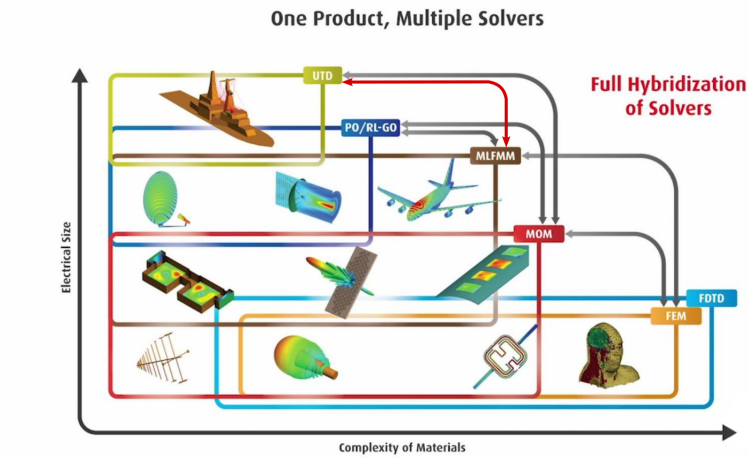

Figure 1.3: Different simulation techniques available in the commercial software FEKO, grouped according to problem size and complexity of the simulation domain [16]. The gray arrows show hybrid techniques, i.e. the integration of multiple techniques into a new tool. The red arrow shows the hybrid scheme investigated in this work. Image courtesy of Altair Engineering Inc.

scheme, leveraging Perfectly Matched Layer (PML) damping, UTD solutions for such geometries can now be derived numerically.
In Chapter 2, the notation used in this work and some basics about MLFMM and GO are given. The method developed to extend the use of UTD to more general sources is explained in detail in Chapter 3. Then, the novel MLFMM-UTD scheme is introduced in Chapter 4. The numerical computation of canonical UTD solutions for more intricate geometries is presented in Chapter 5. Chapter 6 ends this work with some concluding remarks and an overview of future work.

References

[1] J. G. Van Bladel, *Electromagnetic Fields, 2nd edition*. Wiley-IEEE press, 2007.

[2] A. Sommerfeld, *Optics*. Academic Press, 1954.

[3] A. Communications, *3D Urban Intelligent Ray Tracing*, Accessed on March 25th, 2016, 2006. [Online]. Available: `http://www.awe-communications.com/Propagation/Urban/IRT/`.

[4] J. B. Keller, "Geometrical Theory of Diffraction", *J. Opt. Soc. Am.*, vol. 52, no. 2, pp. 116–130, 1961.

[5] R. G. Kouyoumjian and P. H. Pathak, "A Uniform Geometrical Theory of Diffraction for an Edge in a Perfectly Conducting Surface", *Proc. IEEE*, vol. 62, no. 11, pp. 1448–1461, 1974.

[6] W. D. Burnside, R. C. Rudduck, and R. J. Marhefka, "Summary of GTD Computer Codes Developed at the Ohio State University", *IEEE Transactions on Electromagnetic Compatibility*, vol. EMC-22, pp. 238–243, 1980.

[7] F. Molinet, T. George, J. M. Brun, and L. P. Untersteller, "Description of a General Computer Program for RCS Computation of Complex Shapes Described by a CAD System, Founded on GTD/UTD", in *Antennas and Propagation Society International Symposium, 1992. AP-S. 1992 Digest. Held in Conjuction with: URSI Radio Science Meeting and Nuclear EMP Meeting., IEEE in Chicago, Illinois*, vol. 3, 1992, pp. 1462–1465.

[8] P. E. Hussar, V. Oliker, H. L. Riggins, E. M. Smith-Rowlan, W. R. Klocko, and L. Prussner, "An Implementation of the UTD on Facetized CAD Platform Models", *IEEE Antennas and Propagation Magazine*, vol. 42, pp. 100–106, 2000.

[9] O. S. University, *Computational Electromagnetics: Research and Publications*, Accessed on May 25th, 2016. [Online]. Available: `https://electroscience.osu.edu/research-publications/computational-electromagnetics`.

[10] J.-M. Jin, *The Finite Element Method in Electromagnetics (second edition)*. Wiley-IEEE Press, 2002, isbn: 978-0-4714-3818-2.

[11] R. F. Harrington, *Field Computation by Moment Methods (IEEE Press Series on Electromagnetic Wave Theory)*. Wiley-IEEE Press, 1993, isbn: 978-0-7803-1014-8.

[12] F. Olyslager, K. Cools, I. Bogaert, J. Fostier, J. Peeters, F. P. Andriulli, and E. Michielssen, "Recent Advances in Fast Multipole Methods to Simulate Ever Larger and More Complex Structures", *2008 Asia-Pacific Symposium on Electromagnetic Compatibility and 19th International Zurich Symposium on Electromagnetic Compatibility, Vols 1 and 2*, pp. 363–366, 2008.

[13] R. Coifman, V. Rokhlin, and S. Wandzura, "The Fast Multipole Method for the Wave Equation: A Pedestrian Prescription", *IEEE Antennas and Propagation Magazine*, vol. 35, pp. 7–12, 1993.

[14] C.-C. Lu and W. C. Chew, "A Multilevel Algorithm for Solving a Boundary Integral Equation of Wave Scattering", *Microwave and Optical Technology Letters*, vol. 7, pp. 466–470, 1994.

[15] B. Michiels, J. Fostier, I. Bogaert, and D. De Zutter, "Full-Wave Simulations of Electromagnetic Scattering Problems With Billions of Unknowns", *IEEE Trans. Antennas Propagat.*, vol. 63, no. 2, pp. 796–799, 2015.

[16] Altair, *FEKO Webinar: Choosing the Right Solver in FEKO*, Accessed on March 29th, 2016. [Online]. Available: `http://web2.altairhyperworks.com/feko-webinar-choosing-the-right-solver-in-feko`.

2

Electromagnetic Modeling Techniques

★ ★ ★

In this chapter, the fundamentals of electromagnetics and the notation used in this dissertation are briefly introduced. The two methods on which the novel hybrid scheme is based, i.e. Geometrical Optics (GO) and the Multilevel Fast Multipole Methods (MLFMM), are described. Moreover, the Fast Far-field Approximation (FAFFA) is introduced as a method that employs a ray-approximation to further accelerate MLFMM.

2.1 Frequency domain electromagnetics

2.1.1 Fundamentals

Electric current densities $\boldsymbol{J}(\boldsymbol{r},t)$ and electric charge densities $q(\boldsymbol{r},t)$ induce electromagnetic fields. The electric field $\boldsymbol{E}(\boldsymbol{r},t)$, magnetic field $\boldsymbol{H}(\boldsymbol{r},t)$, electric induction $\boldsymbol{D}(\boldsymbol{r},t)$ and magnetic induction $\boldsymbol{B}(\boldsymbol{r},t)$ are governed by Maxwell's equations:

$$\nabla \times \boldsymbol{E}(\boldsymbol{r},t) = -\frac{\partial \boldsymbol{B}(\boldsymbol{r},t)}{\partial t} \tag{2.1}$$

$$\nabla \times \boldsymbol{H}(\boldsymbol{r},t) = \frac{\partial \boldsymbol{D}(\boldsymbol{r},t)}{\partial t} + \boldsymbol{J}(\boldsymbol{r},t) \tag{2.2}$$

$$\nabla \cdot \boldsymbol{D}(\boldsymbol{r},t) = q(\boldsymbol{r},t) \tag{2.3}$$

$$\nabla \cdot \boldsymbol{B}(\boldsymbol{r},t) = 0. \tag{2.4}$$

Maxwell's equations are often studied in the frequency domain. Then, no transient phenomena are present and all quantities vary harmonically with time, i.e. $f(\boldsymbol{r},t) = \hat{f}(\boldsymbol{r})\exp(j\omega t)$[1], where ω is the angular frequency. The dependency of $\hat{f}(\boldsymbol{r})$ on ω is implicitly assumed. The time derivatives are replaced by a factor $j\omega$ in the frequency domain, such that Maxwell's equations become (the $\hat{}$ sign for the frequency-dependent fields is omitted):

$$\nabla \times \boldsymbol{E}(\boldsymbol{r}) = -j\omega \boldsymbol{B}(\boldsymbol{r}) \tag{2.5}$$

$$\nabla \times \boldsymbol{H}(\boldsymbol{r}) = j\omega \boldsymbol{D}(\boldsymbol{r}) + \boldsymbol{J}(\boldsymbol{r}) \tag{2.6}$$

$$\nabla \cdot \boldsymbol{D}(\boldsymbol{r}) = q(\boldsymbol{r}) \tag{2.7}$$

$$\nabla \cdot \boldsymbol{B}(\boldsymbol{r}) = 0. \tag{2.8}$$

Maxwell's equations (2.5)-(2.8) have too many degrees of freedom to be solvable. Additional relationships between the different field quantities, based on the physical properties of the materials involved, are required and they are called constitutive equations. Different constitutive equations are necessary for different background media. In this work, only linear, isotropic media are studied, with the following constitutive equations:

$$\boldsymbol{D}(\boldsymbol{r}) = \epsilon(\boldsymbol{r})\boldsymbol{E}(\boldsymbol{r}) \tag{2.9}$$

$$\boldsymbol{B}(\boldsymbol{r}) = \mu(\boldsymbol{r})\boldsymbol{H}(\boldsymbol{r}). \tag{2.10}$$

$\epsilon(\boldsymbol{r})$ and $\mu(\boldsymbol{r})$ are called the permittivity and permeability of the background medium, respectively. When $\epsilon(\boldsymbol{r}) \equiv \epsilon$ and $\mu(\boldsymbol{r}) \equiv \mu$, with ϵ and μ being constants, the medium is called *homogeneous*.
A lossy dielectric has a complex permittivity $\tilde{\epsilon}$ and is characterized by the permittivity ϵ and the loss tangent $\tan\delta$, such that

$$\tilde{\epsilon} = \epsilon(1 - j\tan\delta), \tag{2.11}$$

with $\epsilon > 0$ and $\tan\delta > 0$.
Often the relative permittivity $\epsilon_r(\boldsymbol{r})$ and relative permeability $\mu_r(\boldsymbol{r})$ are used, i.e.

[1] In literature, the $\exp(-i\omega t)$ convention is also often used, and leads, e.g., to different expressions for the Green's functions, (see Sec. 2.1.2).

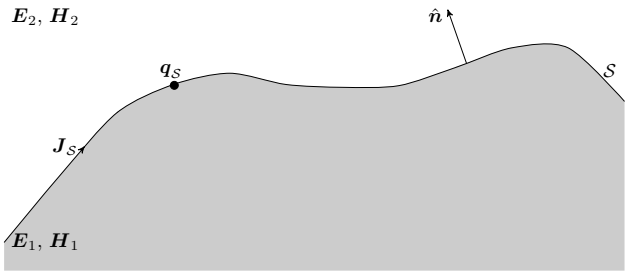

Figure 2.1: Two homogeneous media separated by interface $\mathcal{S}$. The unit vector $\hat{n}$ points towards medium 2.

$$\epsilon(\boldsymbol{r}) = \epsilon_0 \epsilon_r(\boldsymbol{r}) \tag{2.12}$$
$$\mu(\boldsymbol{r}) = \mu_0 \mu_r(\boldsymbol{r}), \tag{2.13}$$

where $\epsilon_0 \approx 8.85 \cdot 10^{-12}\,\mathrm{F/m}$ and $\mu_0 = 4\pi \cdot 10^{-7}\,\mathrm{H/m}$ are the permittivity and permeability of free space, respectively.

Supplemented with boundary conditions at the interface between materials with different electrical properties, Maxwell's equations have a unique solution. These boundary conditions are derived by making use of Maxwell's equations in integral form. Consider the interface $\mathcal{S}$ between two homogeneous media as shown in Fig. 2.1. Under certain circumstances a surface current density $\boldsymbol{J}_{\mathcal{S}}$ and a charge density $q_{\mathcal{S}}$ might exist on the surface between media 1 and 2. One important example of such surface current and charge densities are found on a PEC. Then, the boundary conditions are given by:

$$[\hat{\boldsymbol{n}} \times (\boldsymbol{E}_2 - \boldsymbol{E}_1)]_{\mathcal{S}} = \boldsymbol{0} \tag{2.14}$$
$$[\hat{\boldsymbol{n}} \times (\boldsymbol{H}_2 - \boldsymbol{H}_1)]_{\mathcal{S}} = \boldsymbol{J}_{\mathcal{S}} \tag{2.15}$$
$$[\hat{\boldsymbol{n}} \cdot (\boldsymbol{D}_2 - \boldsymbol{D}_1)]_{\mathcal{S}} = q_{\mathcal{S}} \tag{2.16}$$
$$[\hat{\boldsymbol{n}} \cdot (\boldsymbol{B}_2 - \boldsymbol{B}_1)]_{\mathcal{S}} = 0, \tag{2.17}$$

When e.g. medium 1 is a PEC, $\boldsymbol{E}_1$, $\boldsymbol{H}_1$, $\boldsymbol{D}_1$ and $\boldsymbol{B}_1$ all vanish.
If the problem is invariant in one direction, say the z-direction, Maxwell's equations in a homogeneous medium simplify considerably. We decompose $\boldsymbol{r}$ into $\boldsymbol{r} = \boldsymbol{\rho} + z\hat{\boldsymbol{z}}$ and $\boldsymbol{E}(\boldsymbol{\rho})$ into $\boldsymbol{E}(\boldsymbol{\rho}) = \boldsymbol{E}_t(\boldsymbol{\rho}) + E_z(\boldsymbol{\rho})\hat{z}$ and similarly for $\boldsymbol{H}(\boldsymbol{\rho})$ (in the following, we will omit the $\boldsymbol{\rho}$ dependence). Then, (2.5) and (2.6) become

$$\nabla_t \times \boldsymbol{E}_t = -j\omega\mu H_z \hat{\boldsymbol{z}} \tag{2.18}$$
$$\nabla_t \times (E_z \hat{\boldsymbol{z}}) = -j\omega\mu \boldsymbol{H}_t \tag{2.19}$$
$$\nabla_t \times \boldsymbol{H}_t = (j\omega\epsilon E_z + J_z)\hat{\boldsymbol{z}} \tag{2.20}$$
$$\nabla_t \times (H_z \hat{\boldsymbol{z}}) = j\omega\epsilon \boldsymbol{E}_t + \boldsymbol{J}_t, \tag{2.21}$$

where $\nabla_t = \hat{\boldsymbol{x}}\partial/\partial x + \hat{\boldsymbol{y}}\partial/\partial y$. Maxwell's equations are now split in two separate problems: (2.18) and (2.21) couple the transverse electric field and the z-component of the magnetic field. This is called the transverse electric (TE) problem. The other two equations describe the transverse magnetic (TM) problem. Taking the curl of (2.19) and inserting (2.20), the Helmholtz equation is obtained

$$\nabla_t^2 E_z + k^2 E_z = j\omega\mu J_z, \tag{2.22}$$

where $k^2 = \omega^2\epsilon\mu$ is the wavenumber. For the TE-case, a similar Helmholtz equation holds for the H_z component.

2.1.2 Green's functions

Solutions of the Helmholtz equation (2.22), called Green's functions, are solutions of

$$\nabla_t^2 G + k^2 G = \delta(\boldsymbol{\rho}'), \tag{2.23}$$

where $\delta(\boldsymbol{\rho}')$ is the Dirac-delta function. Once the Green's function is known, the general solution of (2.22) follows simply by superposition, i.e.

$$E_z(\boldsymbol{\rho}) = j\omega\mu \int_{\mathcal{S}} \mathrm{d}\boldsymbol{\rho}'\, G(\boldsymbol{\rho};\boldsymbol{\rho}') J_z(\boldsymbol{\rho}'), \tag{2.24}$$

where $\mathcal{S}$ is the surface on which sources reside.
The exact form of the Green's function depends on the boundary conditions that uniquely define the solution of (2.23). We give two examples of Green's functions relevant for this work.

Free space

In free-space, the only boundary condition is the radiation condition. In 2-D, it is given by [1]

$$\lim_{\rho\to\infty} \sqrt{\rho}\left(\frac{\partial G}{\partial \rho} + jkG\right) = 0, \tag{2.25}$$

where $\rho = \|\boldsymbol{\rho} - \boldsymbol{\rho}'\|$. The Green's function for free space is [2]

$$G(\boldsymbol{\rho}; \boldsymbol{\rho}') = \frac{j}{4} H_0^{(2)}(k \|\boldsymbol{\rho} - \boldsymbol{\rho}'\|). \tag{2.26}$$

Interesting asymptotic expressions are [3]

$$G \sim \frac{1}{2\pi} \ln(k\rho), \ \rho \to 0 \tag{2.27}$$

$$G \sim \frac{j}{4} \sqrt{\frac{2j}{\pi k}} \frac{\exp(-jk\rho)}{\sqrt{\rho}}, \ \rho \to \infty. \tag{2.28}$$

A formula that is related to these asymptotic expressions and that will be of particular interest in this work, is the asymptotic behavior of the Hankel function for large arguments

$$H_\nu^{(2)}(z) \sim j^\nu \sqrt{\frac{2j}{\pi z}} e^{-jz}, \ |z| \to \infty. \tag{2.29}$$

A wedge

The canonical example of a wedge is also of particular interest for this study. At high frequencies, scattering at a wedge can be interpreted as consisting of different ray-optical contributions, such as direct illumination, reflection and diffraction, which in this work will be linked to the framework of MLFMM. The Green's function is readily available and serves as a reference in this work. The boundary conditions that uniquely describe the problem are [1], [4]

(i) The Helmholtz equation (2.23) for $0 < \phi, \phi' < 2\pi - \psi$.

(ii) The radiation condition (2.25).

(iii) Boundary conditions on the faces:

$$\text{Dirichlet: } G(\boldsymbol{\rho}; \boldsymbol{\rho}') = 0, \ \phi = 0 \text{ and } \phi = 2\pi - \psi$$

$$\text{Neumann: } \frac{\partial G}{\partial n}(\boldsymbol{\rho}; \boldsymbol{\rho}') = 0, \ \phi = 0 \text{ and } \phi = 2\pi - \psi$$

(iv) Behavior of the solution at the wedge tip $\rho \to 0$ ($\delta > 0$):

$$G(\boldsymbol{\rho}; \boldsymbol{\rho}') = \mathcal{O}(\rho^\delta)$$

$$\left| \frac{\partial G(\boldsymbol{\rho}; \boldsymbol{\rho}')}{\partial \phi} \right| + \left| \frac{\partial^2 G(\boldsymbol{\rho}; \boldsymbol{\rho}')}{\partial \phi^2} \right| = \mathcal{O}(\rho^\delta)$$

Condition (iv) ensures that the tip neither radiates, nor absorbs energy. The Green's function for these boundary conditions is given by [5]

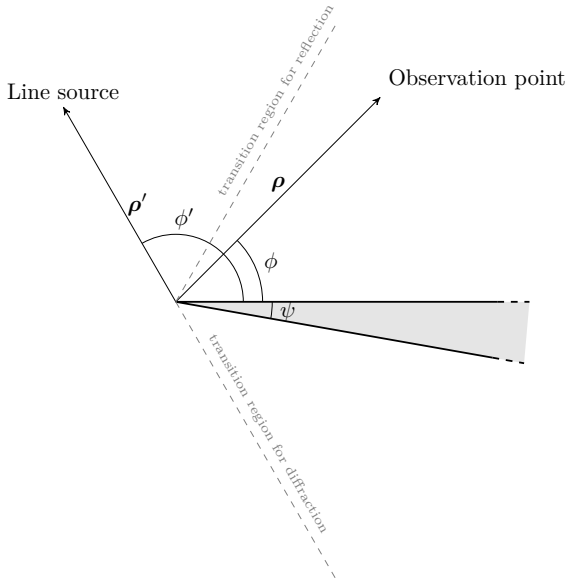

Figure 2.2: Canonical geometry of a wedge.

$$G(\boldsymbol{\rho};\boldsymbol{\rho}') = -\frac{j}{4n}\sum_{m=0}^{\infty}\epsilon_m J_\mu(k\rho_<)H_\mu^{(2)}(k\rho_>)[\cos(\mu(\phi-\phi')) \pm \cos(\mu(\phi+\phi'))], \tag{2.30}$$

where $\epsilon_m = 1$ if $m = 0$, $\epsilon_m = 2$ otherwise and $\mu = m/\nu$ with $\nu\pi = (2\pi - \psi)$. Also, $\rho_< = \min(\rho, \rho')$ and $\rho_> = \max(\rho, \rho')$. In (2.30), the plus sign should be retained for the Neumann conditions (TE case), and the minus sign for the Dirichlet conditions (TM case).
The convergence of this series is determined by the product of the special functions. For large μ, the asymptotic expansion of this product is

$$J_\mu(k\rho_<)H_\mu^{(2)}(k\rho_>) \sim \frac{1}{\sqrt{2\pi\mu}}\left(\frac{ek\rho_<}{2\mu}\right)^{\mu}\cdot j\sqrt{\frac{2}{\pi\mu}}\left(\frac{ek\rho_>}{2\mu}\right)^{-\mu} = \frac{j}{\pi\mu}\left(\frac{\rho_<}{\rho_>}\right)^{\mu},$$

and it becomes clear that the series converges fast for small $\frac{\rho_<}{\rho_>}$.
This series also forms the basis for the derivation of the UTD diffraction coefficient for the canonical wedge structure. A derivation of the UTD high-frequency solution is given in Appendix A.

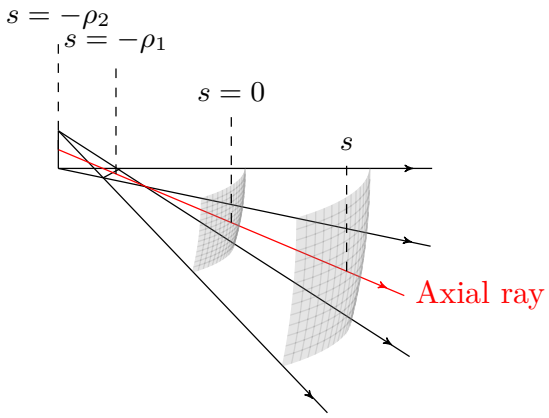

Figure 2.3: Axial ray and wavefronts in its neighborhood, at two different positions along the ray path. The paraxial rays shown in black are perpendicular to the wavefront. Locally, wavefronts can be approximated by a second degree equation, leading to the definition of Gaussian curvature.

2.2 Geometrical optics

At very high frequencies/short wavelengths, electromagnetic waves behave as they exist of numerous rays, each one interacting individually with the materials it crosses on its path. For example, visible light is an electromagnetic field with a short wavelength at the typical dimensions of objects and structures such as humans, buildings, etc. of everyday life. For engineering purposes, treating the scattering at complex targets through a ray approximation not only considerably simplifies the analysis of the problem, but also yields physical insight. Ray-optical methods are often used to describe scattering at extremely large targets, e.g. cargo ships [6], airplanes/missiles [7] and urban environments [8]–[10].
In this section we present an overview of geometrical ray methods that are used in this dissertation. Another class of high-frequency methods, the currents-based physical optics (PO) and physical theory of diffraction (PTD), are not presented here. The interested reader is encouraged to consult further references, e.g. [11].

2.2.1 Ray nature of EM waves

In GO, the ray nature of electromagnetic waves arises as a high-frequency solution of the Helmholtz equation. The field is expanded into a Luneberg-Klein series, i.e. a series in terms of inverse powers of the frequency [12]. In the 2-D

case, the z-component of the field u (electric field in the TM case and magnetic field in the TE case) is written as

$$u_z(\boldsymbol{\rho}) = \exp(-jk\psi(\boldsymbol{\rho})) \sum_{m=0}^{\infty} \frac{u_m(\boldsymbol{\rho})}{(j\omega)^m}. \tag{2.31}$$

For very high frequencies, the $m = 0$ term becomes the dominant contribution in this series. Retaining only this term and introducing it into (2.22) for a sourceless region results in

$$\exp(-jk\psi(\boldsymbol{\rho}))\Big[\big(\nabla_t^2 + k^2 - k^2(\nabla_t\psi(\boldsymbol{\rho}))^2\big) - jk\big(\nabla_t^2\psi(\boldsymbol{\rho}) + 2k\nabla_t\psi(\boldsymbol{\rho})\cdot\nabla_t\big)\Big]u_0(\boldsymbol{\rho}) = 0. \tag{2.32}$$

Both the real part and the imaginary part between the square brackets need to be zero. The real part leads to the eikonal equation. A variational interpretation of it yields the well-known Fermat's principle, which dictates that rays follow the optical path with minimal or maximal length. The imaginary part leads to a transport equation. It can be solved along the ray direction, which is described by an intrinsic parameter s. The situation is illustrated in Fig. 2.3. The solution for propagation between a starting point at $s = 0$ and observation at s is [13]

$$u_z(s) \sim u_0(s)\exp(-jk\psi(s)) = u_0(0)\exp(-jk(\psi(0)+s))\sqrt{\frac{G(s)}{G(0)}}, \tag{2.33}$$

where $G(s)$ is the Gaussian curvature at s

$$G(s) = \frac{1}{(\rho_1 + s)(\rho_2 + s)}, \tag{2.34}$$

and ρ_1 and ρ_2 are the principal curvatures of the wavefront at $s = 0$ as shown in Fig. 2.3. Introducing (2.34) into (2.33) leads to

$$u_z(s) \sim u_0(0)\exp(-jk(\psi(0)+s))\sqrt{\frac{\rho_1\rho_2}{(\rho_1 + s)(\rho_2 + s)}}. \tag{2.35}$$

For the 2-D case, one of the principal curvatures is infinite.
Expression (2.35) shows how the amplitude and the phase of the field evolve along a ray path. Locally, the field behaves as a plane wave, with nearly constant amplitude and a phase factor $-jks$. Globally, the amplitude of the ray scales as $1/s$ for large s. In 2-D, when one of the principal curvatures is infinite, the

amplitude of the ray scales as $1/\sqrt{s}$ for large s. This is consistent with the high-frequency approximation (2.28) that was derived for the exact solution of (2.22).

2.2.2 Reflection

Expression (2.35) can also be used to describe reflected rays. Choosing the point of reflection at $s = 0$ yields the following expression for the reflected field:

$$u_z^{refl}(s) \sim u^{refl}(0) \exp(-jk(\psi^{refl}(0) + s)) \sqrt{\frac{\rho_1^{refl} \rho_2^{refl}}{(\rho_1^{refl} + s)(\rho_2^{refl} + s)}}. \quad (2.36)$$

The quantities on the right-hand side are related to the incoming field. The amplitude of the reflected field at the reflection point $s = 0$ is related to that of the incoming field through a reflection coefficient R. If the ray impinges from a medium with impedance $Z_1 = \sqrt{\mu_1/\epsilon_1}$ and reflects at an interface of a medium with an impedance Z_2, then the reflection coefficient is given by [2]

$$R_{TM} = \frac{Z_2 \cos\phi_i - Z_1 \cos\phi_t}{Z_2 \cos\phi_i + Z_1 \cos\phi_t} \quad (2.37)$$

$$R_{TE} = \frac{Z_1 \cos\phi_i - Z_2 \cos\phi_t}{Z_1 \cos\phi_i + Z_2 \cos\phi_t}, \quad (2.38)$$

where ϕ_i is the angle that the incoming ray makes with the normal to the interface at the reflection point and ϕ_t is given by

$$k_2 \sin\phi_t = k_1 \sin\phi_i. \quad (2.39)$$

For a PEC interface, $R_{TM} = -1$ and $R_{TE} = 1$.
The principal curvatures ρ_1^{refl} and ρ_2^{refl} of the reflected wavefront are found by diagonalizing the curvature matrix of the reflected wavefront [14]. In the case of a flat reflection surface, the principal curvatures of the reflected wavefront are the same as the principal curvatures of the incoming wavefront. Furthermore, $\psi^{refl}(0) = 0$. The reflected electric field at a flat surface is finally given by

$$u_z^{refl}(s) \sim u^{inc}(0)\, R \exp(-jks) \sqrt{\frac{\rho_1^{inc} \rho_2^{inc}}{(\rho_1^{inc} + s)(\rho_2^{inc} + s)}}, \quad (2.40)$$

where ρ_i^{inc}, $(i = 1, 2)$ are the radii of curvature of the incoming field at the reflection point.

2.2.3 Diffraction

Consider again the geometry of Fig. 2.2. Each observation point that cannot be connected by a straight line to the source point without crossing the wedge is in the shadow. Consequently, the field is zero according to GO. However, in reality, owing to diffraction, this is not the case. Also, the full-wave expression (2.30) predicts a non-zero value of the field. Moreover, the solution for observation points far from the tip behaves as a cylindrical wave, which can e.g. be seen from (2.30). Therefore, in [15], Keller introduced a *canonical solution* to describe diffraction in terms of rays. The canonical solution is found by scaling the value of the incoming field at the diffraction point by a diffraction coefficient D and a divergence factor, that describes the amplitude and phase variation of the diffracted wave. As this is a cylindrical wave in the 2-D case, the divergence factor becomes $\exp(-jks)/\sqrt{s}$, where s is the distance between diffraction and observation points. The field then becomes

$$u_z^{diff}(s) \sim u^{inc}(0)\, D\, \frac{\exp(-jks)}{\sqrt{s}}. \tag{2.41}$$

The diffraction coefficient D, called the GTD diffraction coefficient, was derived by Keller from a high-frequency approximation of the exact solution when the incoming field is a plane wave [1] and is given by

$$D = -\frac{\exp(-j\pi/4)}{2\nu\sqrt{2\pi k}}\left[\cot\left(\frac{\pi+(\phi-\phi')}{2\nu}\right)+\cot\left(\frac{\pi-(\phi-\phi')}{2\nu}\right)\right.$$
$$\left.\pm\left(\cot\left(\frac{\pi+(\phi+\phi')}{2\nu}\right)+\cot\left(\frac{\pi-(\phi+\phi')}{2\nu}\right)\right)\right], \tag{2.42}$$

where the angles ϕ and ϕ' are defined in Fig. 2.2 and $\nu\pi = 2\pi - \psi$. The plus sign is valid for the TE case and the minus sign for the TM case. Although derived for plane-wave illumination, D can be used for other illumination sources as well, as long as the incoming field at the diffraction tip can be locally approximated by a plane-wave.
GTD fails in the so-called *transition regions*, which are the boundaries at which either the reflection contribution or the direct illumination disappears from a ray-optical point of view. The GTD coefficient becomes singular in this case. UTD provides a solution that remains valid in the transition regions. The UTD corrections to (2.42) depend on the type of illumination. The UTD diffraction coefficient for line source illumination is derived in Appendix A.

2.3 Boundary element methods

2.3.1 Notation

We briefly introduce the notation that will be used in the following chapters. The pertinent geometry consists of a source group/box and an observation group/box, not necessarily of the same size. A point of reference, in later chapters identified with a diffracting tip, serves as the origin of a global coordinate system with axes $(\hat{\boldsymbol{x}}, \hat{\boldsymbol{y}}, \hat{\boldsymbol{z}})$. The configuration is shown in Fig. 2.4. Position vectors fixed to the origin of the global coordinate system are denoted $\boldsymbol{\rho}$. A subscript c is used to indicate the center of a group/box. The accent $'$ is used to denote a source group/box. Without an accent, the quantity is related to an observation group/box. Position vectors of external sources, not related to the BIE scatterers, are indicated with a subscript s and vectors of additional observation points with subscript o. Angles with respect to the $\hat{\boldsymbol{x}}$-axis are denoted with the Greek alphabet characters θ, ϕ, ψ.
Local coordinate axes $(\hat{\boldsymbol{\xi}}, \hat{\boldsymbol{\eta}}, \hat{\boldsymbol{\zeta}})$ are introduced to indicate quantities that relate to the center of a box B or b (B denotes a parent box, whereas b denotes a child box). This is illustrated in Fig. 2.5. Position vectors fixed to local coordinate systems are denoted $\boldsymbol{r}$. The accents and subscripts retain the same meaning as for the global coordinate system. Angles with respect to the $\hat{\boldsymbol{\xi}}$-axis are denoted α, β, γ. The circumscribing circle of the box is denoted $\mathcal{C}$ and has a radius R. A position vector to a point on the surface of $\mathcal{C}$ is denoted $\boldsymbol{R}$.

2.3.2 The Electric Field Integral Equation

Consider a free-space environment in which N_S PEC cylinders reside. Their boundaries are denoted by $\mathcal{C}_i$ $(i = 1, \ldots, N_S)$. The total electric field is now decomposed into the incoming field $E_z^{inc}(\boldsymbol{\rho})$ due to external, known excitation sources and a scattered field due to the excited, unknown surface current densities $J_z(\boldsymbol{\rho}')$ on the surface of the scatterers. The scattered electric field is found by integration over the currents, as in (2.24). Imposing the boundary condition (2.14) leads to the Electric Field Integral Equation (EFIE), given by

$$E_z^{inc}(\boldsymbol{\rho}) = -j\omega\mu_0 \sum_{i=1}^{N_S} \oint_{\mathcal{C}_i} \mathrm{d}\boldsymbol{\rho}'\, G(\boldsymbol{\rho}; \boldsymbol{\rho}') J_z(\boldsymbol{\rho}'), \tag{2.43}$$

where μ_0 is the magnetic permeability of the (non-magnetic) background medium and $G(\boldsymbol{\rho}; \boldsymbol{\rho}')$ is the Green's function for a line source residing at $\boldsymbol{\rho}'$. $\boldsymbol{\rho}$ is a point on the surface of the scatterers. In a classical MoM scheme, as the background medium does not contain any scatterers, the Green's function used in (2.43) is the free space Green's function $G^{free}(\boldsymbol{\rho}; \boldsymbol{\rho}')$ (2.26).

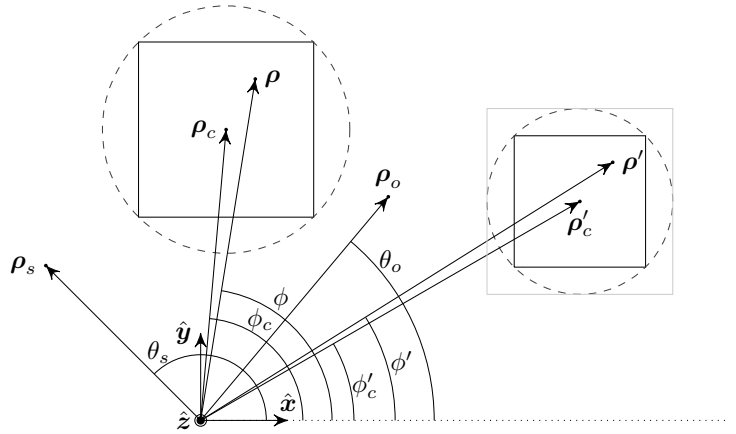

Figure 2.4: Global coordinates notation. The area at the right, inside the gray square boundary, is illustrated in detail in Fig. 2.5.

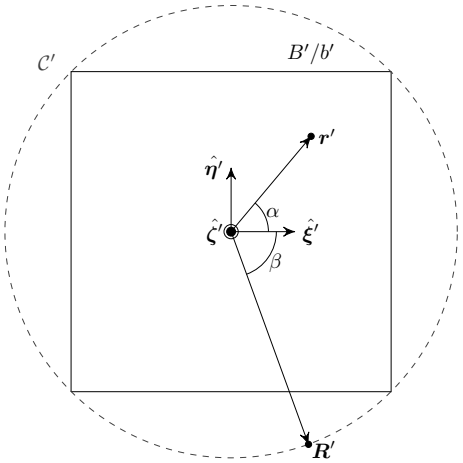

Figure 2.5: Local coordinates notation. The figure corresponds to the area inside the square boundary in Fig. 2.4.

The surface of the scatterers is discretized into N *segments* and a basis function $b_m(\boldsymbol{\rho})$ with limited support s_m is assigned to each segment ($m = 1, \ldots, N$). The surface current is now approximated by

$$J_z(\boldsymbol{\rho}') \approx \sum_{m=1}^{N} I_m b_m(\boldsymbol{\rho}'), \tag{2.44}$$

where I_m is an unknown expansion coefficient related to the basis function $b_m(\boldsymbol{\rho}')$. Common basis functions are pulse functions, triangular functions and sinusoidal

functions [16]. Next, testing functions[2] $t_l(\boldsymbol{\rho})$ with support s_l are defined. Multiplication of (2.43) with each testing function and integration over its support results in the following matrix system

$$E_l = \sum_{m=0}^{N} Z_{l,m} I_m, \tag{2.45}$$

where

$$E_l = \int_{s_l} \mathrm{d}\boldsymbol{\rho}\, E_z^{inc}(\boldsymbol{\rho}) t_l(\boldsymbol{\rho}), \tag{2.46}$$

$$Z_{l,m} = -j\omega\mu_0 \int_{s_l} \mathrm{d}\boldsymbol{\rho} \int_{s_m} \mathrm{d}\boldsymbol{\rho}'\, G(\boldsymbol{\rho};\boldsymbol{\rho}') t_l(\boldsymbol{\rho}) b_m(\boldsymbol{\rho}'). \tag{2.47}$$

In matrix notation, the linear system (2.45) becomes $\boldsymbol{E} = \boldsymbol{Z} \cdot \boldsymbol{I}$, where $\boldsymbol{E}$ is called the excitation vector, $\boldsymbol{Z}$ the MoM interaction matrix and $\boldsymbol{I}$ the current vector.
Mostly, the integrations are performed numerically by means of Gaussian quadratures. Good implementations exist to compute the necessary integration points and weights, see e.g. [17]. We use 4^{th}-order and 5^{th}-order Gaussian quadrature, which provide an exact result if the integrand is a 7^{th}-order or 9^{th}-order polynomial, respectively [16]. Singularity extraction is used for self-segment (when $m = l$) or neighbor-segment interactions (when segments share a common point), see e.g. [18].
The linear system of (2.45) is solved for the unknown current vector by an iterative solver, such as e.g. the bi-conjugate gradient method [16]. The iterative solver converges in a computational time that scales as $\mathcal{O}\big(PN^2\big)$, where P is the number of iterations and N^2 is the operational count of one matrix-vector product (MVP). Provided that the interaction matrix is well-conditioned, i.e. $P \ll N$, the solution time will thus be $\mathcal{O}\big(N^2\big)$.

2.3.3 The Multilevel Fast Multipole Method

To relax the computational memory and cost of solving the MoM system, MLFMM is used. In an L-level MLFMM scheme, all the segments are enclosed in a hypothetical square box that is recursively partitioned $L-1$ times to create a uniform quad-tree. The number of levels L is chosen such that the side length of the smallest box, at the lowest level $l = 1$, so obtained, is about half a wavelength. A box is said to be empty when no segments reside in it and empty boxes are immediately discarded during the construction of the tree. At each level $l = 1, 2, \ldots, L$, the boxes are circumscribed by a hypothetical circle

[2] Test and basis functions often coincide.

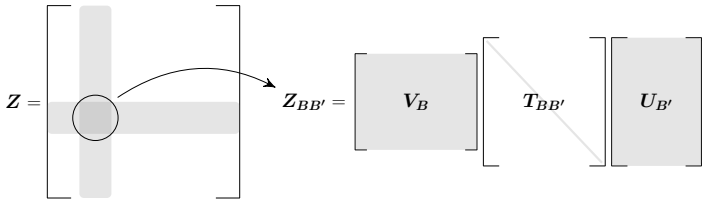

Figure 2.6: The decomposition of the MoM interaction matrix in FMM.

of radius R_l. Finally, at all levels and starting with the highest one, so-called *far interaction pairs* are identified. A pair of "child" boxes on level l constitute a far interaction pair if (i) the distance between their closest points is greater than a fixed constant, typically chosen as $5R_l$, and (ii) their "parent" boxes on level $l+1$ do not constitute a far interaction pair. At the lowest level $l = 1$, all non-far interaction pairs are labeled as near interaction pairs. Interactions between two segments that reside in two boxes labeled as a near interaction pair are treated in the classical BIE-MoM way of Sec. 2.3.2.
When $L = 1$, the resulting two-level hierarchical scheme is used during the matrix-vector product (MVP). For a pair of boxes B and B', the corresponding block in the interaction matrix is decomposed as shown in Fig. 2.6. The decomposition of the interaction matrix allows performing the MVP of MoM in three efficient steps:

- Aggregation: For every box B', the product $\boldsymbol{U}_{B'} \cdot \boldsymbol{I}_{B'}$, where $\boldsymbol{I}_{B'}$ contains the unknowns I_m for segments in box B', is computed. Physically, this corresponds to the aggregation of the current densities in B' into *outgoing plane waves* $\mathrm{OPW}_{q'}$.

- Translation: For every far interaction pair of boxes B and B', the OPWs of box B' are translated to box B through the product $T_{BB',qq'} \cdot \mathrm{OPW}_{q'}$. The result is called the *incoming plane waves* IPW_q at box B. IPWs arriving at the same observation box B from several source boxes B' can simply be superimposed.

- Desaggregation: The IPWs are converted back to field values at the individual segments through the product with matrix $\boldsymbol{V}_B$.

This scheme is very efficient for two reasons. First, the OPWs are re-used to describe the interaction of a source box with all far observation boxes. Similarly, desaggregation of the IPWs is only performed once for the superposition of all far interactions. Second, because the translation matrix is diagonal, every

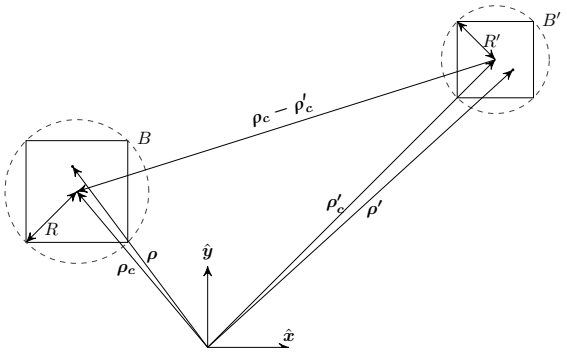

Figure 2.7: Illustration of the contribution due to direct coupling: typical MLFMM constellation of a source box B' and an observation box B.

OPW is translated into only one IPW[3]. The complexity of this one-level FMM is $\mathcal{O}\big(N^{3/2}\big)$.

The decomposition shown in Fig. 2.6 is possible because of Graf's addition theorem. Consider Fig. 2.7, where a source at $\boldsymbol{\rho}'$ resides inside box B' with center $\boldsymbol{\rho}'_c$ and an observation point $\boldsymbol{\rho}$ resides inside box B with center $\boldsymbol{\rho}_c$. The addition theorem allows to write the Green's function in (2.26) as [3]

$$G(\boldsymbol{\rho};\boldsymbol{\rho}') = \frac{j}{4}\sum_{m=-\infty}^{\infty} H_m^{(2)}(k\rho_>)J_m(k\rho_<)\exp\left(jm(\theta-\theta')\right), \tag{2.48}$$

where

$$\begin{aligned}\boldsymbol{\rho}_> &= \boldsymbol{\rho}_c - \boldsymbol{\rho}'_c\\ \boldsymbol{\rho}_< &= -(\boldsymbol{\rho}-\boldsymbol{\rho}_c) + (\boldsymbol{\rho}'-\boldsymbol{\rho}'_c)\end{aligned}$$

and θ and θ' are the angles that $\boldsymbol{\rho}_>$ and $\boldsymbol{\rho}_<$ make with the $\hat{\boldsymbol{x}}$-axis, respectively. (2.48) is valid provided that $\rho_> > \rho_<$. We further introduce the Fourier integral form [3]

$$J_q(k\rho_<)\exp\left(-jm\theta'\right) = \frac{1}{2\pi}\int_{2\pi} \mathrm{d}\beta\, \exp\left(j\boldsymbol{k}(\beta)\cdot\boldsymbol{\rho}_<\right)\exp\Big(-jm(\beta+\frac{\pi}{2})\Big), \tag{2.49}$$

with $\boldsymbol{k}(\beta) = k[\cos\beta, \sin\beta]^T$ into (2.48), such that

[3]In Chapter 4, it will be shown that under some special conditions, the scheme retains its efficiency even for a full translation matrix.

$$G(\boldsymbol{\rho};\boldsymbol{\rho}') = \frac{j}{4}\frac{1}{2\pi}\sum_{m=-\infty}^{\infty} H_m^{(2)}(k\rho_>)\exp\left(jm(\theta-\frac{\pi}{2})\right) \cdot \int_{2\pi} \mathrm{d}\beta\, \exp\left(j\boldsymbol{k}(\beta)\cdot\boldsymbol{\rho}_<\right)\exp\left(-jm\beta\right). \quad (2.50)$$

The integral in (2.50) represents the Fourier transform of the far-field of a line source at $\boldsymbol{\rho}_<$. It is known that this function is quasi-bandlimited, i.e. its spectrum decreases super-exponentially for frequencies higher than a certain bandwidth [19]. Provided that one samples such a function with a sufficiently high sampling rate, it can be reconstructed up to an arbitrary accuracy. If $2Q+1$ samples are sufficient, the integral is discretized with

$$\int_{2\pi}\mathrm{d}\beta \;\rightarrow \frac{2\pi}{2Q+1}\sum_{q=-Q}^{Q}$$
$$\beta \rightarrow \beta_q = \frac{2\pi q}{2Q+1},\; q=-Q,\ldots,Q,$$

such that

$$G(\boldsymbol{\rho};\boldsymbol{\rho}') = \frac{j}{4}\sum_{q=-Q}^{Q}\exp\left(-j\boldsymbol{k}(\beta_q)\cdot(\boldsymbol{\rho}-\boldsymbol{\rho}_c)\right) \cdot\left[\frac{1}{2Q+1}\sum_{m=-Q}^{Q} H_m^{(2)}(k\rho_>)\exp\left(jm(\theta-\beta_q-\frac{\pi}{2})\right)\right] \cdot\exp\left(j\boldsymbol{k}(\beta_q)\cdot(\boldsymbol{\rho}'-\boldsymbol{\rho}_c')\right). \quad (2.51)$$

Introduction of (2.51) into (2.47) leads to the following expression for the elements of the $\boldsymbol{U}_{B'}$, $\boldsymbol{T}_{BB'}$ and $\boldsymbol{V}_B$ matrices:

$$V_{B,lq} = \int_{s_l}\mathrm{d}\boldsymbol{\rho}\, t_l(\boldsymbol{\rho})\exp\left(-j\boldsymbol{k}(\beta_q)\cdot(\boldsymbol{\rho}-\boldsymbol{\rho}_c)\right) \quad (2.52)$$

$$T_{BB',qq'} = \frac{\omega\mu_0}{4}\delta_{qq'}\left[\frac{1}{2Q+1}\sum_{m=-Q}^{Q} H_m^{(2)}(k\rho_>)\exp\left(jm(\theta-\beta_q-\frac{\pi}{2})\right)\right] \quad (2.53)$$

$$U_{B',q'm} = \int_{s_m}\mathrm{d}\boldsymbol{\rho}'\, b_m(\boldsymbol{\rho}')\exp\left(j\boldsymbol{k}(\beta_{q'})\cdot(\boldsymbol{\rho}'-\boldsymbol{\rho}_c')\right), \quad (2.54)$$

where $\delta_{qq'}$ is the Kronecker delta function. For sufficient accuracy, the number of samples should scale with the box radius R_l as [20]

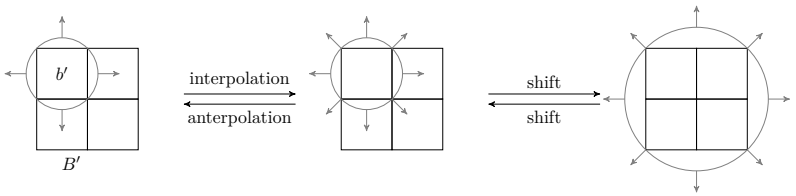

Figure 2.8: Illustration of the transition to higher or lower levels of the MLFMM tree for the OPWs and IPWs [19].

$$Q \sim (2kR_l) + C(2kR_l)^{1/3}, \tag{2.55}$$

where C is a positive constant.

When $L > 1$, translations will be performed at the highest possible level, as explained before. The OPWs of a higher-level parent box B' are then not computed by using the MVP explained before, but are directly computed from the OPWs of their children boxes b'. Two additional steps are required, as schematically shown in Fig. 2.8:

1. The bandwidth Q_l is larger at the parent level, thus the number of samples is first increased during *interpolation*. The OPWs at the new sample points are found either by using a limited number of OPWs around every new sample point (local interpolation) [20] or by global interpolation [19]. In this work we opt for global interpolation. This is efficiently performed by the use of Fast Fourier Transforms (FFTs). First, the spectral content of the OPWs of the child box is computed through FFT. As the OPWs are quasi-bandlimited, the spectral content is exponentially small at the tails and can therefore be padded with zeros. Then, the zero-padded signal is transformed back to a larger set of OPWs by an inverse FFT. A schematic representation of the interpolation is also shown in Fig. 2.9.

2. The phase center needs to be translated from the center of the child box to the center of the parent box. From (2.54), it is seen that every OPW needs to be multiplied by a factor $\exp\left(-j\boldsymbol{k}(\beta_{q'}) \cdot (\boldsymbol{\rho}_c^{B'} - \boldsymbol{\rho}_c^{b'})\right)$. We choose to store these factors during the setup phase, at the expense of an increased memory cost. The contributions of the OPWs of different child boxes are simply superimposed.

Similarly, after the translation step, the IPWs of the higher-level boxes are recursively *anterpolated* to the $l = 1$ level in the inverse procedure of interpolation.

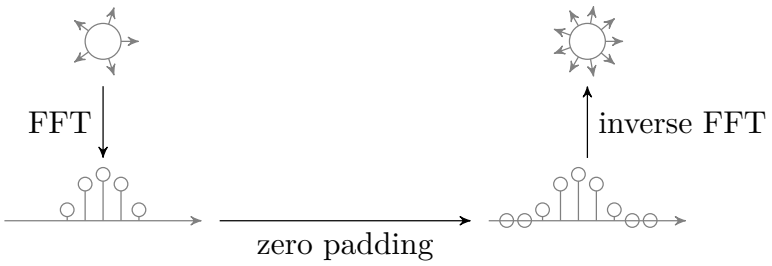

Figure 2.9: Schematic illustration of global interpolation of the OPWs [19].

2.3.4 The Fast Far-Field Approximation

The Fast Far-Field Approximation (FAFFA) provides a means to further accelerate the translation step of MLFMM. Thereto, for interacting boxes that are very far apart, the number of translated OPWs is reduced to one [21].
Indeed, when source and observation point are very far apart, the Green's function becomes (see (2.28))

$$G(\boldsymbol{\rho};\boldsymbol{\rho}') \sim \frac{j}{4}\sqrt{\frac{2j}{\pi k\,\|\boldsymbol{\rho}-\boldsymbol{\rho}'\|}}\exp\left(-jk\,\|\boldsymbol{\rho}-\boldsymbol{\rho}'\|\right)$$

Further, we introduce $\boldsymbol{\rho}_<$ and $\boldsymbol{\rho}_>$ as in Sec. 2.3.3. It is now assumed that the distance between the boxes B and B' is much larger than the dimensions of the boxes, such that $\rho_> \gg \rho_<$. $\|\boldsymbol{\rho}-\boldsymbol{\rho}'\|$ can be approximated by

$$\|\boldsymbol{\rho}-\boldsymbol{\rho}'\| = \rho_> - \hat{\boldsymbol{k}}(\theta)\cdot\boldsymbol{\rho}_< + \mathcal{O}\big(\rho_>^{-1}\big), \tag{2.56}$$

where $\hat{\boldsymbol{k}}(\theta) = [\cos\theta, \sin\theta]^T$. Finally, we obtain

$$G(\boldsymbol{\rho};\boldsymbol{\rho}') \sim \frac{j}{4}\sqrt{\frac{2j}{\pi k\rho_>}}\exp\left(-jk\rho_>\right)\exp\left(j\boldsymbol{k}(\theta)\cdot\boldsymbol{\rho}_<\right). \tag{2.57}$$

This expression is similar to (2.51), except for the far-field expression for the translator and it only contains one relevant angle θ. Thus, in FAFFA, translation of only one OPW is required. It has been shown that this leads to reduction of the overall computational complexity by a factor of two [21].
Note that, in MLFMM, OPWs are available only at a discrete set of angles β_q and in general the angle θ will not coincide with any of these angles. Usually, the OPW is approximated by a Lagrange interpolation based on the OPWs at neighboring angles [21], [22].

References

[1] A. Sommerfeld, *Optics*. Academic Press, 1954.

[2] J. G. Van Bladel, *Electromagnetic Fields, 2nd edition*. Wiley-IEEE press, 2007.

[3] *NIST Digital Library of Mathematical Functions*, http://dlmf.nist.gov/, Release 1.0.5 of 2012-10-01. [Online]. Available: `http://dlmf.nist.gov/`.

[4] M. A. Lyalinov and N. Y. Zhu, *Scattering of Waves by Wedges and Cones with Impedance Boundary Conditions*. Scitech Publishing, 2012.

[5] F. Oberhettinger, "Diffraction of Waves by a Wedge", *Communications on Pure and Applied Mathematics*, vol. 7, no. 3, pp. 551–563, 1954.

[6] X. H. Mao and Y. H. Lee, "UHF Propagation Along a Cargo Hold on Board a Merchant Ship", *IEEE Trans. Wireless Comm.*, vol. 12, no. 1, pp. 22–30, 2013.

[7] F. Weinmann, "Ray Tracing with PO/PTD for RCS Modeling of Large Complex Objects", *IEEE Trans. Antennas Propagat.*, vol. 54, no. 6, pp. 1797–1806, 2006.

[8] G. E. Athanasiadou, A. R. Nix, and J. P. McGeehan, "A Microcellular Ray-Tracing Propagation Model and Evaluation of its Narrow-Band and Wide-Band Predictions", *IEEE Journal on Selected Areas in Communications*, vol. 18, no. 3, pp. 322–335, 2000.

[9] T. Fuegen, J. Maurer, T. Kayser, and W. Wiesbeck, "Capability of 3-D Ray Tracing for Defining Parameter Sets for the Specification of Future Mobile Communications Systems", *IEEE Trans. Antennas Propagat.*, vol. 54, no. 11, pp. 3125–3137, 2006.

[10] A. O. Kaya, W. Trappe, L. J. Greenstein, and D. Chizhik, "Predicting MIMO Performance in Urban Microcells Using Ray Tracing to Characterize the Channel", *IEEE Trans. Wireless Comm.*, vol. 11, no. 7, pp. 2402–2411, 2012.

[11] P. Y. Ufimtsev, *Fundamentals of the Physical Theory of Diffraction*. Wiley-IEEE Press, 2014.

[12] R. G. Kouyoumjian and P. H. Pathak, "A Uniform Geometrical Theory of Diffraction for an Edge in a Perfectly Conducting Surface", *Proc. IEEE*, vol. 62, no. 11, pp. 1448–1461, 1974.

[13] D. L. Shealy, "Geometrical Optics: Some Applications of the Law of Intensity", in *Society of Photo-Optical Instrumentation Engineers (SPIE) Conference Series*, Accessed on March 11th, 2016, vol. 6289, 2006. [Online]. Available: `http://people.cas.uab.edu/~dls/publications/spie6289/spie6289-16_electronic-paper.pdf`.

[14] G. A. Deschamps, "Ray Techniques in Electromagnetics", *Proc. IEEE*, vol. 60, pp. 1022–1035, 1972.

[15] J. B. Keller, "Geometrical Theory of Diffraction", *J. Opt. Soc. Am.*, vol. 52, no. 2, pp. 116–130, 1961.

[16] W. C. Gibson, *The Method of Moments in Electromagnetics*. CRC press, 2008.

[17] G. von Winckel, *Legendre-Gauss Quadrature Weights and Nodes*, Accessed on March 15th, 2016. [Online]. Available: `http://www.mathworks.com/matlabcentral/fileexchange/4540-legendre-gauss-quadrature-weights-and-nodes/content/lgwt.m`.

[18] J. Fostier and F. Olyslager, "A GRID Computer Implementation of the Multilevel Fast Multipole Algorithm for Full-Wave Analysis of Optical Devices", *IEICE Transactions on Communications*, vol. E90B, no. 9, pp. 2430–2438, 2007, issn: 0916-8516.

[19] D. Vande Ginste, "Perfectly Matched Layer Based Fast Multipole Methods for Planar Microwave Structures", PhD thesis, UGent, 2005.

[20] W. C. Chew, J.-M. Jin, E. Michielssen, and J. Song, *Fast and Efficient Algorithms in Computational Electromagnetics*. Artech House Publishers, 2001.

[21] T. J. Cui, W. C. Chew, G. Chen, and J. Song, "Efficient MLFMA, RPFMA, and FAFFA Algorithms for EM Scattering by Very Large Structures", *IEEE Trans. Antennas Propagat.*, vol. 52, no. 3, pp. 759–770, 2004.

[22] A. Tzoulis and T. F. Eibert, "A Hybrid FEBI-MLFMM-UTD Method for Numerical Solutions of Electromagnetic Problems Including Arbitrarily Shaped and Electrically Large Objects", *IEEE Trans. Antennas Propagat.*, vol. 53, no. 10, pp. 3358–3366, 2005.

3

Computation of the diffraction from complex illumination sources in extended regions of space

G. Karagounis, D. De Zutter and D. Vande Ginste

This chapter is based on an article published in
Optics Express [1] and on a contribution to the
Computational Electromagnetics International Workshop (CEM) (2015) [2].

★ ★ ★

In this chapter, a two-dimensional high-frequency formalism is presented which describes the diffraction of arbitrary wavefronts incident on edges of an otherwise smooth surface. The diffracted field in all points of a predefined region of interest is expressed in terms of the generalized Huygens representation of the incident field and a limited set of coupling coefficients that take into account the arbitrary nature of the incident wavefront and its diffraction. The method is based on UTD and can therefore be utilized for every canonical problem for which the UTD diffraction coefficient is known. Moreover, the proposed technique is easy to implement as only standard FFT routines are required. The technique's validity is confirmed both theoretically and numerically. It is shown that for fields emitted by

a discrete line source and diffracted by a perfectly conducting wedge, the method is in excellent agreement with the analytic solution over the entire simulation domain, including regions near shadow and reflection boundaries. As an application example, the diffraction in the presence of a perfectly conducting wedge illuminated by a complex light source is analyzed, demonstrating the appositeness of the method.

3.1 Introduction

On the one hand, GTD [3] and UTD [4] are still used extensively due to the simplicity of their implementation. Despite the popularity of UTD, in essence, it can only be used to study the diffraction of plane waves or fields emitted by discrete sources. GTD is applicable to any kind of illumination, but it is less accurate than UTD close to the diffraction edge and it does not provide the correct solution over the entire space, as its solution is singular at transition regions. On the other hand, formalisms that can deal with complex source configurations [5]–[6] often miss transparency and/or are very intricate and as such are less likely to be used in practice. Because of this, scattering by large objects is either studied using full-wave electromagnetic solvers, which require large amounts of memory and computing time, or the original problem is simplified so that the high-frequency methods can still be used, leading to loss of accuracy.
The high-frequency formalism that is presented in this chapter describes the diffraction of arbitrary incident fields. As the formalism is based on UTD, it can be used for every geometry for which the UTD diffraction coefficient is available. In addition, the field over an extended region of space is obtained using the generalized Huygens representation of the incident field and a limited set of coupling coefficients. The technique has been presented in a transparent way and can readily be used in applications, this in contrast to the Spectral Theory of Diffraction (STD) [6].
In Sec. 3.2, we present the new formalism. The validity of the formalism is established both theoretically and experimentally in Sec. 3.3. In Sec. 3.4, we give some final remarks.

3.2 Formalism

In this section, the new formalism is derived. It will be shown that by leveraging standard FFT routines, the diffracted field for an arbitrary, spatially distributed source configuration is readily computed.
The geometry of the problem is illustrated in Fig. 3.1. Diffraction by a straight,

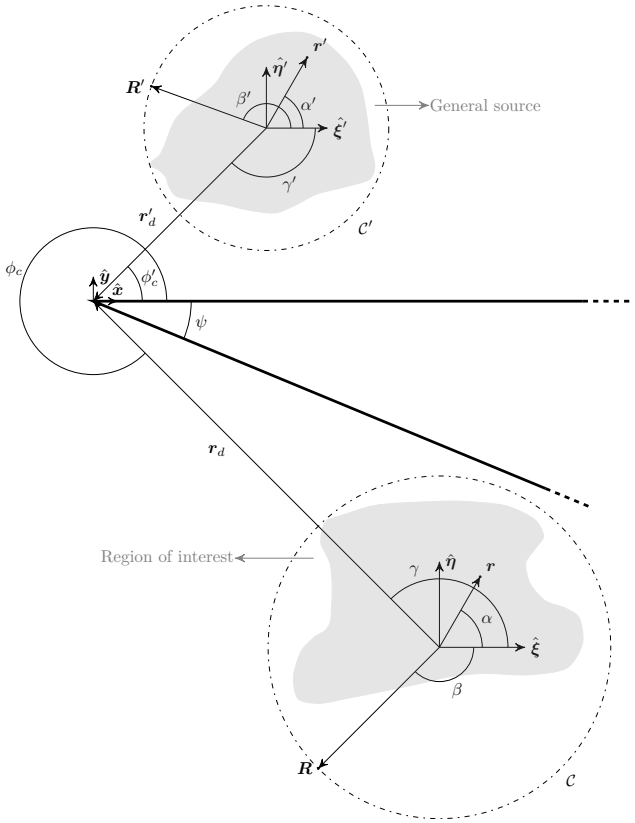

Figure 3.1: Canonical problem geometry. An arbitrary, spatially distributed light source (light gray) illuminates the wedge, leading to a (diffracted) field within a user-defined, spatially distributed region of interest (light gray).

perfectly conducting wedge is considered, although the formalism is applicable to any canonical problem for which the diffraction coefficient is known. The tip of the wedge resides at the origin of the coordinate system ($\hat{\boldsymbol{x}}$, $\hat{\boldsymbol{y}}$). The distributed source is indicated in light gray in the figure. A local Cartesian coordinate system ($\hat{\boldsymbol{\xi}}'$, $\hat{\boldsymbol{\eta}}'$) is attached to this source configuration, from which the local polar coordinates (r, α') are derived. With respect to the ($\hat{\boldsymbol{\xi}}'$, $\hat{\boldsymbol{\eta}}'$) system, the wedge resides at $\boldsymbol{r}'_d$, making an angle γ' measured from the $\hat{\boldsymbol{\xi}}'$-axis. Conversely, the origin of this local coordinate system resides at an angle ϕ'_c measured from the $\hat{\boldsymbol{x}}'$-axis. The distributed source is circumscribed by a circle $\mathcal{C}'$ with radius R' centered about the origin of the local coordinate system (dash-dot line in the figure). This circle is described by position vector $\boldsymbol{R}'$, making an angle β' measured from the $\hat{\boldsymbol{\xi}}'$-axis. Similarly, the region of interest is also indicated on the figure, a local coordinate system is attached to it and

its circumscribing circle $\mathcal{C}$ is drawn. The question that now arises is how to efficiently compute the field within the complete region of interest.
On the one hand, we consider the souce field outside contour $\mathcal{C}'$, i.e. for $r' > R'$. The source field can be first expressed in terms of angular harmonics in the $(\hat{\boldsymbol{\xi}}', \hat{\boldsymbol{\eta}}')$ coordinate system:

$$E_z^{inc}(\boldsymbol{r}') = -\frac{\omega\mu_0}{4} \sum_{q'=-\infty}^{\infty} a_{q'} H_{q'}^{(2)}(kr') e^{jq'\alpha'}, \; r' > R', \tag{3.1}$$

where $H_{q'}^{(2)}$ stands for the Hankel function of the second kind and of order q', $r' = \|\boldsymbol{r}'\|$. The coefficients $a_{q'}$ are related to the incident field on the boundary $\mathcal{C}'$ as follows:

$$a_{q'} = -\frac{2}{\pi\omega\mu_0 \, H_{q'}^{(2)}(kR')} \int_{-\pi}^{\pi} \mathrm{d}\beta' \, E_z^{inc}(\boldsymbol{R}') e^{-jq'\beta'}. \tag{3.2}$$

Hence, upon knowledge of $E_z^{inc}(\boldsymbol{R}')$, they can be efficiently computed by means of a FFT.
Second, the source field can be expressed by introducing equivalent Huygens sources $\mathcal{J}_z(\boldsymbol{R}')$ on $\mathcal{C}'$ that produce the same field as in (3.1) for $r' > R'$. Thereto, consider the field radiated by these equivalent sources:

$$E_z^{inc}(\boldsymbol{r}') = -\frac{\omega\mu_0}{4} \int_{-\pi}^{\pi} R' \mathrm{d}\beta' \, \mathcal{J}_z(\boldsymbol{R}') H_0^{(2)}(k \left\|\boldsymbol{r}' - \boldsymbol{R}'\right\|). \tag{3.3}$$

Given the periodicity along $\mathcal{C}'$, $\mathcal{J}_z(\boldsymbol{R}')$ is decomposed into its Fourier series

$$\mathcal{J}_z(\boldsymbol{R}') = \sum_{q'=-\infty}^{\infty} I_{q'} e^{jq'\beta'}, \tag{3.4}$$

with as yet unknown coefficients $I_{q'}$. Graf's addition theorem [7] dictates that

$$H_0^{(2)}\left(k \left\|\boldsymbol{r}' - \boldsymbol{R}'\right\|\right) = \sum_{m=-\infty}^{\infty} H_m^{(2)}(kr') J_m(kR') e^{jm(\alpha'-\beta')}, \; r' > R', \tag{3.5}$$

Introducing (3.4) and (3.5) into (3.3) allows to relate the two descriptions of the source field. Identification with (3.1) yields

$$I_{q'} = \frac{a_{q'}}{2\pi R' J_{q'}(kR')}. \tag{3.6}$$

(3.3) can also be rewritten as:

$$E_z^{inc}(\boldsymbol{r}') = -\frac{\omega\mu_0}{4}\sum_{q'=-\infty}^{\infty}\frac{a_{q'}}{2\pi J_{q'}(kR')}\int_{-\pi}^{\pi}\mathrm{d}\beta'\,H_0^{(2)}\left(k\left\|\boldsymbol{r}'-\boldsymbol{R}'\right\|\right)e^{jq'\beta'}. \quad (3.7)$$

On the other hand, we focus on the diffracted field within the region of interest. First, the diffracted field can be expressed as a superposition of UTD contributions from Sec. 2.2.3 due to the line sources in (3.7). The diffracted field in $\boldsymbol{r}$, in the $(\hat{\boldsymbol{\xi}},\hat{\boldsymbol{\eta}})$ coordinate system, is then given by

$$E_z^{diff}(\boldsymbol{r}) = -\frac{\omega\mu_0}{4}\frac{e^{-jk\|-\boldsymbol{r}_d+\boldsymbol{r}\|}}{\sqrt{\|-\boldsymbol{r}_d+\boldsymbol{r}\|}}\sum_{q'=-\infty}^{\infty}\frac{a_{q'}}{2\pi J_{q'}(kR')}$$
$$\times\int_{-\pi}^{\pi}\mathrm{d}\beta'\,D_{UTD}\left(L;-\boldsymbol{r}_d'+\boldsymbol{R}',-\boldsymbol{r}_d+\boldsymbol{r}\right)e^{jq'\beta'}H_0^{(2)}\left(k\left\|\boldsymbol{r}_d'-\boldsymbol{R}'\right\|\right). \quad (3.8)$$

Second, the diffracted field is expanded into angular harmonics within the region of interest. The decomposition is similar to (3.1), i.e.

$$E_z^{diff}(\boldsymbol{r}) = -\frac{\omega\mu_0}{4}\sum_{q=-\infty}^{\infty}b_q J_q(kr)e^{jq\alpha}, \quad (3.9)$$

with $r=\|\boldsymbol{r}\|<R$ and with the coefficients b_q given by

$$b_q = \frac{1}{2\pi J_q(kR)}\sum_{q'=-\infty}^{\infty}\frac{a_{q'}}{2\pi J_{q'}(kR')}\int_{-\pi}^{\pi}\mathrm{d}\beta\,\frac{e^{-jk\|-\boldsymbol{r}_d+\boldsymbol{R}\|}}{\sqrt{\|-\boldsymbol{r}_d+\boldsymbol{R}\|}}e^{-jq\beta}$$
$$\times\int_{-\pi}^{\pi}\mathrm{d}\beta'\,D_{UTD}\left(L;-\boldsymbol{r}_d'+\boldsymbol{R}',-\boldsymbol{r}_d+\boldsymbol{R}\right)e^{jq'\beta'}H_0^{(2)}\left(k\left\|\boldsymbol{r}_d'-\boldsymbol{R}'\right\|\right). \quad (3.10)$$

As the proposed formalism is valid at high frequencies, the high-frequency approximation of the 2-D Green's function, i.e. the Hankel function, is used to symmetrize (3.10) in the integrals over β' and β. Substitution of (2.29) into (3.10) leads to

$$b_q \approx \frac{1}{2\pi J_q(kR)}\sum_{q'=-\infty}^{\infty}\frac{a_{q'}}{2\pi J_{q'}(kR')}\sqrt{\frac{\pi k}{2j}}\int_{-\pi}^{\pi}\mathrm{d}\beta\,H_0^{(2)}\left(k\left\|-\boldsymbol{r}_d+\boldsymbol{R}\right\|\right)e^{-jq\beta}$$
$$\times\int_{-\pi}^{\pi}\mathrm{d}\beta'\,D_{UTD}\left(L;-\boldsymbol{r}_d'+\boldsymbol{R}',-\boldsymbol{r}_d+\boldsymbol{R}\right)e^{jq'\beta'}H_0^{(2)}\left(k\left\|\boldsymbol{r}_d'-\boldsymbol{R}'\right\|\right). \quad (3.11)$$

Although (3.9) and (3.11) suffice to determine the diffracted field in the entire region of interest, the computation would be rather cumbersome as the integrand of the double integral is highly oscillatory with multiple, possibly coinciding,

stationary points. Fortunately, this integration can be circumvented by again invoking Graf's addition theorem of (3.5), but now for $H_0^{(2)}(k\left\|\boldsymbol{r}'_d - \boldsymbol{R}'\right\|)$ and $H_0^{(2)}(\|-\boldsymbol{r}_d + \boldsymbol{R}\|)$. After some straightforward mathematical manipulations, the following final expression for the diffracted field is obtained:

$$E_z^{diff}(\boldsymbol{r}) \approx -\frac{\omega\mu_0}{4}\sum_{q=-\infty}^{\infty}\left[\sum_{q'=-\infty}^{\infty} t_{qq'}a_{q'}\right] J_q(kr)e^{jq\alpha}, \tag{3.12}$$

with known coefficients $a_{q'}$ from (3.2) and coupling coefficients

$$t_{qq'} = \frac{1}{J_{q'}(kR')J_q(kR)}\sum_{n=-\infty}^{\infty} H_n^{(2)}(kr_d)J_n(kR)e^{-jn\gamma} \times \sum_{m=-\infty}^{\infty}\frac{1-j}{2}\sqrt{\pi k}\, d_{-n+q,m-q'}H_m^{(2)}(kr'_d)J_m(kR')e^{jm\gamma'}. \tag{3.13}$$

The coupling coefficients $t_{qq'}$ connect the angular harmonics expansion of the incident field to the expansion of the field within the region of interest. The coefficients $d_{-n+q,m-q'}$ in (3.13) are given by

$$d_{s,l} = \frac{1}{4\pi^2}\int_{-\pi}^{\pi}\mathrm{d}\beta\, e^{-js\beta}\int_{-\pi}^{\pi}\mathrm{d}\beta'\, e^{-jl\beta'}D_{UTD}\left(L; -\boldsymbol{r}'_d + \boldsymbol{R}', -\boldsymbol{r}_d + \boldsymbol{R}\right), \tag{3.14}$$

and hence, they are efficiently computed via 2-D FFTs of the pertinent diffraction coefficient. Note indeed that the integrand in the 2-D FFT of (3.14) is no longer oscillatory.

The introduction of the high-frequency approximation of the 2-D Green's function in (3.10) can be questioned. However, in Chapter 4, it will be shown that this approximation can be undone. Moreover, it is shown that the coupling coefficients $t_{qq'}$ are proportional to the 2-D FFT of the diffracted field. This adds physical meaning to the coupling coefficients and also yields a more efficient means to compute them. Otherwise, an alternative approach, employing a mathematically rigorous Green's addition theorem in the high-frequency limit [7], leads to the same coupling coefficients as the ones given in Sec. 4.2.4.

In Sec. 3.3, it will be shown that retaining a limited number of terms in the infinite series of (3.12) and (3.13) leads to a good accuracy. At this point, we opt not to present a full convergence analysis, but restrict ourselves to providing the necessary insight to the reader. Given the large values of $kr' > kR'$ and small values $kr < kR$ in (3.1) and (3.9) respectively, these series converge rapidly. The series in (3.13) can also be truncated, retaining a limited number of terms, provided that only a limited set of coefficients $d_{s,l}$ contributes to this series. This is the case for a smooth, well-behaved integrand in the 2-D FFT computation in (3.14) and hence, at this point, it should be noted that the diffraction

coefficient in the UTD theory is discontinuous at the transition regions. As a result, an accurate description of the diffracted field in regions of interest that cross the transition regions of the source configuration may not be guaranteed because of the Gibbs phenomenon. In order to avoid inaccuracies at transition regions for this kind of problems, rather than focusing on the diffracted field, we propose to describe the *total* field in a "UTD-like manner". Thereto, the total field at $\boldsymbol{r}$ in the $(\hat{\boldsymbol{\xi}},\hat{\boldsymbol{\eta}})$ system, due to a line source with unit current density in the $+\hat{\boldsymbol{z}}$ direction at $\boldsymbol{r}'$ in the $(\hat{\boldsymbol{\xi}}',\hat{\boldsymbol{\eta}}')$ system, is written in the following way

$$\begin{aligned}
E_z^{tot}(\boldsymbol{r};\boldsymbol{r}') &= E^{diff}(\boldsymbol{r};\boldsymbol{r}') + E^{refl}(\boldsymbol{r};\boldsymbol{r}') + E^{direct}(\boldsymbol{r};\boldsymbol{r}') \\
&\approx -\frac{\omega\mu_0}{4}H_0^{(2)}\left(k\left\|\boldsymbol{r}'_d-\boldsymbol{r}'\right\|\right)D_{UTD}\left(L;-\boldsymbol{r}'_d+\boldsymbol{r}',-\boldsymbol{r}_d+\boldsymbol{r}\right) \\
&\quad \times\frac{1-j}{2}\sqrt{\pi k}H_0^{(2)}\left(k\left\|-\boldsymbol{r}_d+\boldsymbol{r}\right\|\right) \\
&\quad +\frac{\omega\mu_0}{4}H_0^{(2)}\left(k\left\|\boldsymbol{r}''_d-\boldsymbol{r}''-\boldsymbol{r}_d+\boldsymbol{r}\right\|\right)u^{refl} \\
&\quad -\frac{\omega\mu_0}{4}H_0^{(2)}\left(k\left\|\boldsymbol{r}'_d-\boldsymbol{r}'-\boldsymbol{r}_d+\boldsymbol{r}\right\|\right)u^{direct} \\
&\equiv -\frac{\omega\mu_0}{4}H_0^{(2)}\left(k\left\|\boldsymbol{r}'_d-\boldsymbol{r}'\right\|\right)D'\left(L;-\boldsymbol{r}'_d+\boldsymbol{r}',-\boldsymbol{r}_d+\boldsymbol{r}\right) \\
&\quad \times\frac{1-j}{2}\sqrt{\pi k}H_0^{(2)}\left(k\left\|-\boldsymbol{r}_d+\boldsymbol{r}\right\|\right). \qquad (3.15)
\end{aligned}$$

The reflection and the direct contributions may both be different from zero depending on the position of the observer relative to the position of the source. Step functions u^{refl} and u^{direct} are added to the above expression to account for this. Vectors with superscript $''$ have a similar meaning as vectors with superscript $'$, but are related to image sources corresponding to reflection contributions. In the last step, a new coefficient $D'\left(L;-\boldsymbol{r}'_d+\boldsymbol{r}',-\boldsymbol{r}_d+\boldsymbol{r}\right)$ is introduced, which equals

$$\begin{aligned}
D'\left(L;-\boldsymbol{r}'_d+\boldsymbol{r}',-\boldsymbol{r}_d+\boldsymbol{r}\right) &= D_{UTD}\left(L;-\boldsymbol{r}'_d+\boldsymbol{r}',-\boldsymbol{r}_d+\boldsymbol{r}\right) \\
&\quad +\frac{1+j}{\sqrt{\pi k}}\frac{1}{H_0^{(2)}\left(k\left\|\boldsymbol{r}'_d-\boldsymbol{r}'\right\|\right)H_0^{(2)}\left(k\left\|-\boldsymbol{r}_d+\boldsymbol{r}\right.\right)\|}\times \\
&\quad \Big[-H_0^{(2)}\left(k\left\|\boldsymbol{r}''_d-\boldsymbol{r}''-\boldsymbol{r}_d+\boldsymbol{r}\right\|\right)u^{refl} \\
&\quad +H_0^{(2)}\left(k\left\|\boldsymbol{r}'_d-\boldsymbol{r}'-\boldsymbol{r}_d+\boldsymbol{r}\right\|\right)u^{direct}\Big]. \qquad (3.16)
\end{aligned}$$

The coefficient $D'\left(L;-\boldsymbol{r}'_d+\boldsymbol{r}',-\boldsymbol{r}_d+\boldsymbol{r}\right)$ is continuous over the transition regions. Using D' instead of D_{UTD} in the formalism, and hence in (3.14), always ensures good accuracy over the transition regions. Additionally, by this substitution, one immediately obtains the sought for total field in the entire region of

interest rather than the diffracted field.

3.3 Results

3.3.1 Theoretical validation at large distance

When $r_d \gg R$ and $r'_d \gg R'$, i.e. when the dimensions of the source and the region of interest become negligible, the proposed formalism should reduce to the UTD formalism. Indeed, with these assumptions we can write the Taylor series of the diffraction coefficient, only retaining the following dominant contribution: $D_{UTD}\left(L; -\boldsymbol{r}'_d + \boldsymbol{R}', -\boldsymbol{r}_d + \boldsymbol{R}\right) \sim D_{UTD}\left(L; -\boldsymbol{r}'_d, -\boldsymbol{r}_d\right), \forall \boldsymbol{R}', \boldsymbol{R}$, i.e. the "distributed" UTD diffraction coefficient reduces to a constant diffraction coefficient, related to the centers of the regions. Inserting the dominant term in (3.14) results in

$$d_{s,l} \sim D_{UTD}\left(L; -\boldsymbol{r}'_d, -\boldsymbol{r}_d\right) \delta_{s,0}\delta_{l,0}, \tag{3.17}$$

where δ is the Kronecker delta symbol. Consequently, the diffracted field in (3.12) becomes

$$E_z^{diff}(\boldsymbol{r}) \sim -\frac{\omega\mu_0}{4} \sum_{q'=-\infty}^{\infty} a_{q'} H_{q'}^{(2)}(kr'_d) e^{jq'\gamma'} D_{UTD}\left(L; -\boldsymbol{r}'_d, -\boldsymbol{r}_d\right) \times \frac{1-j}{2}\sqrt{\pi k} \sum_{q=-\infty}^{\infty} J_q(kr) H_q^{(2)}(kr_d) e^{jq(\alpha-\gamma)}. \tag{3.18}$$

For a single line source, located at $\boldsymbol{r}'$ in the $(\hat{\boldsymbol{\xi}}', \hat{\boldsymbol{\eta}}')$ coordinate system, with unit current density in the $\hat{\boldsymbol{z}}$-direction and with $r' = \|\boldsymbol{r}'\| < R'$, the coefficients $a_{q'}$ are given by

$$a_{q'} = J_{q'}(kr') e^{-jq'\alpha'}. \tag{3.19}$$

After substitution of this result into (3.18), Graf's addition theorem appears in the first summation. The second summation also corresponds to Graf's addition theorem. The factor in front of this summation hints at the previous use of (2.29), which can now be undone. The final result is

$$E_z^{diff}(\boldsymbol{r}; \boldsymbol{r}') \sim -\frac{\omega\mu_0}{4} H_0^{(2)}(k\|\boldsymbol{r}'_d - \boldsymbol{r}'\|) D_{UTD}\left(L; -\boldsymbol{r}'_d, -\boldsymbol{r}_d\right) \frac{e^{-jk\|-\boldsymbol{r}_d+\boldsymbol{r}\|}}{\sqrt{\|-\boldsymbol{r}_d+\boldsymbol{r}\|}}. \tag{3.20}$$

The last expression describes the diffracted field induced by a line source at $\boldsymbol{r}'$ in the $(\hat{\boldsymbol{\xi}}',\hat{\boldsymbol{\eta}}')$ system and observed at $\boldsymbol{r}$ in the $(\hat{\boldsymbol{\xi}},\hat{\boldsymbol{\eta}})$ system. However, here, the diffraction coefficient is calculated from the centers of the corresponding regions, which is allowed when $r_d \gg R$ and $r'_d \gg R'$. This result should be compared to (2.41), proving the validity of the proposed approach.

3.3.2 Verification example

To assess the accuracy of the formalism, consider the geometry shown in Fig. 3.2. In this constellation, $\psi = 30^\text{o}$, $r'_d = 5\lambda$, $\phi'_c = 45^\text{o}$ and $R' = \lambda$ are fixed. The region of interest is moved along a trajectory as shown in the figure (dotted line). The center of the region of interest remains at a constant distance from the edge, $r_d = 10\lambda$. The angle ϕ_c varies from 15° to 315° in steps of 5°. Also, $R = 2\lambda$. A single line source is placed inside the source region and the field is calculated in a discrete observation point P. The source is placed at $r' = 0.8\lambda$ and $\alpha' = 0^\text{o}$ and is excited with unit current density in the $+\hat{\boldsymbol{z}}$ direction. The observation point P is placed at $r = 1.5\lambda$ and $\alpha = \phi_c - 180^\text{o}$. In this way, the field is calculated in a circular arc around the edge. We choose this constellation with a discrete line source and discrete observation point to allow a comparison with the exact analytical solution (2.30). The summations over q' and n in (3.12) and (3.13) are symmetrically truncated to 33 terms, whereas 51 terms are used for the summations over q and m. The series of (2.30) is truncated to 203 terms.

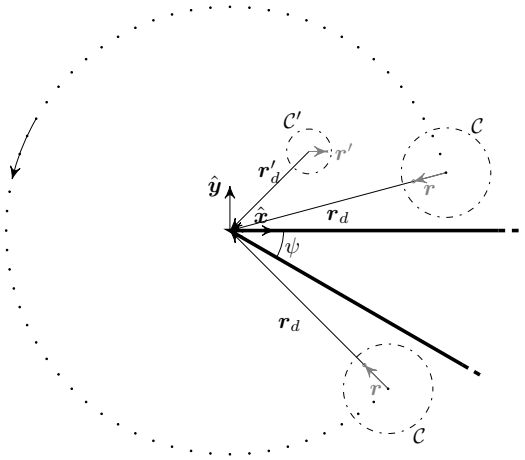

Figure 3.2: Configuration for the numerical validation. The region of interest is held at a constant distance from the edge, while changing its angular position. Its trajectory is indicated by means of the dotted line.

The exact result from (2.30), when the region of interest moves along the trajectory from $\phi_c = 15^\text{o}$ to 315° as described above, is presented in the top

panel of Fig. 3.3, together with the results from the new technique. The first result, indicated by crosses (x), is obtained using the traditional diffraction coefficient D_{UTD} in (3.14); the second, indicated by circles (o), leverages the improved diffraction coefficient D' of (3.16). The error between these two new results and the exact solution is shown in the bottom panel of Fig. 3.3. An excellent accuracy is observed in regions where the integrand of the 2-D FFT transform of (3.14) remains continuous over the integration domain. The integrand is discontinuous for observation angles between 112° and 158° (because of the discontinuity of the contribution due to reflection) and also between 202° and 248° (because of the discontinuity of the direct contribution). In these regions, the advantage of using the coefficient $D'\left(L; -\boldsymbol{r}'_d + \boldsymbol{r}', -\boldsymbol{r}_d + \boldsymbol{r}\right)$ is evident. The maximum relative error when adopting $D'\left(L; -\boldsymbol{r}'_d + \boldsymbol{r}', -\boldsymbol{r}_d + \boldsymbol{r}\right)$ remains bounded to about 1%. This good overall accuracy confirms the validity of the technique.

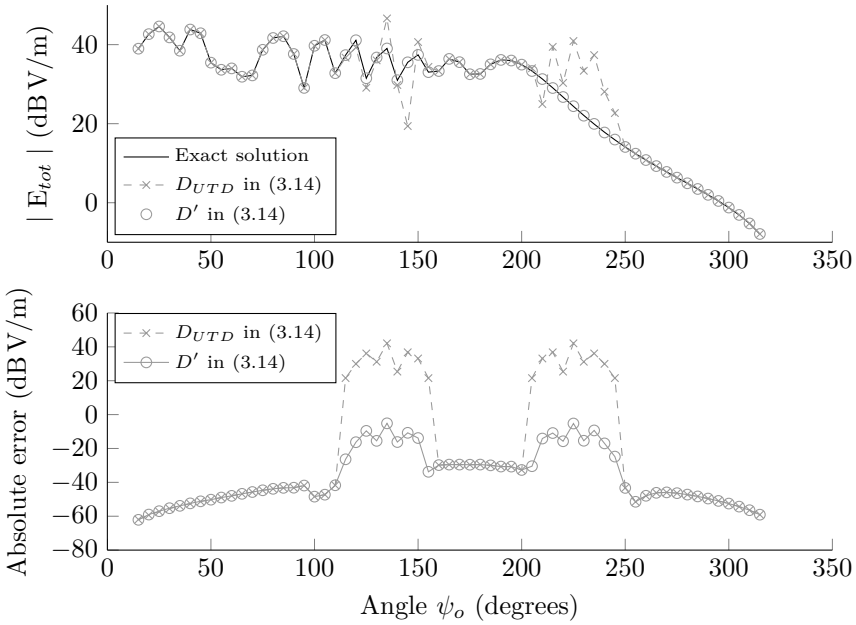

Figure 3.3: Top panel: total field at the varying observation point obtained via the exact solution of (2.30) (black line) and via the proposed technique of (3.12), where the result indicated by crosses (x) is computed relying on the traditional diffraction coefficient, and whereas the result indicated by circles (o) is based on the equivalent UTD coefficient of (3.16). Bottom panel: Absolute error. Note that the maximum relative error (not shown in the figure) remains bounded to about 1% when the equivalent UTD coefficient is used.

The much better results obtained by employing D' in (3.14) can be understood

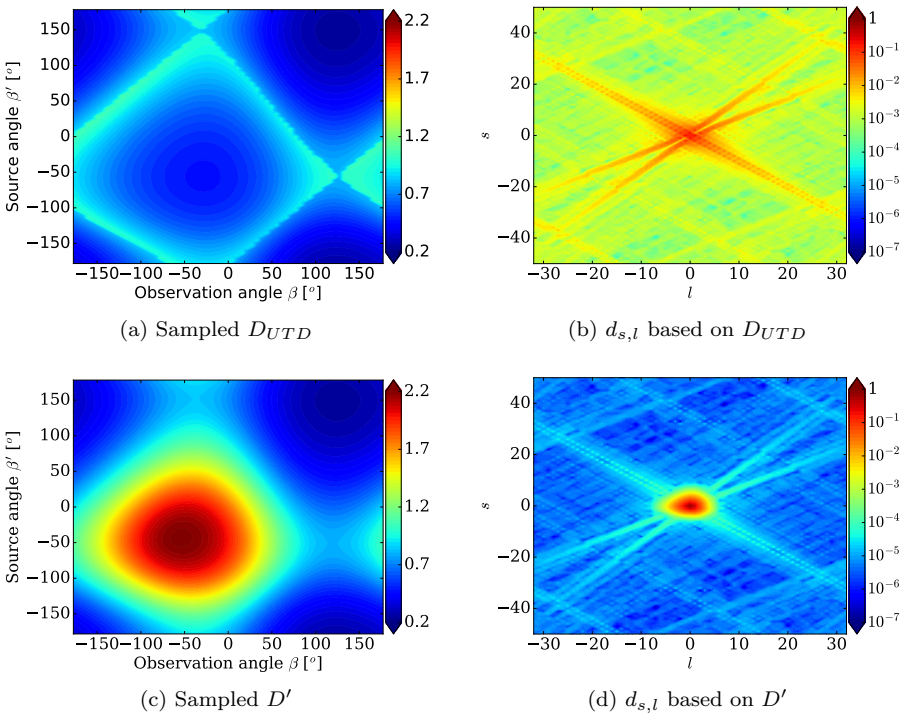

(a) Sampled D_{UTD}

(b) $d_{s,l}$ based on D_{UTD}

(c) Sampled D'

(d) $d_{s,l}$ based on D'

Figure 3.4: Amplitude of the sampled diffraction coefficients D_{UTD} and D' and of the corresponding coefficients $d_{s,l}$ for the geometry in Fig. 3.2, with $\phi_c = 225^{\circ}$.

by investigating the coefficients $d_{s,l}$ in the transition regions. This is shown in Fig. 3.4 for the situation where $\phi_c = 225^{\circ}$. The discontinuity of the diffraction coefficient D_{UTD} in this case is clearly observable in Fig. 3.4(a). Therefore, the amplitude of the coefficients $d_{s,l}$, when computed by employing D_{UTD}, falls off very slowly for increasing $|s|$ and $|l|$. This is shown in Fig. 3.4(b). In contrast, the coefficient D' remains continuous across the transition region, as is shown in Fig. 3.4(c) and as such the coefficients $d_{s,l}$ are strongly centered around $s = 0$, $l = 0$.

3.3.3 Application example

To illustrate the full power of the technique, we will now focus on *distributed* sources and regions of interest by investigating the diffraction of a Gaussian beam by a perfectly conducting wedge. During the last few decades, several studies have been devoted to this problem. We refer the reader to [8] for an

interesting overview. Most of these approaches are based on the fact that a Gaussian beam is equivalent to a line source in complex space [9] and the diffraction is described based on results for ordinary line sources, e.g. (2.30) can be used to derive the solution when the wedge is illuminated by a Gaussian beam, provided that the cylindrical coordinates of the source are replaced by the complex distance ρ_b and the complex angle ϕ_b given below [8], [10].
The geometry of the problem is illustrated in Fig. 3.5. A Gaussian beam, originating at $\boldsymbol{\rho}_0 = \rho_0 \cos\phi_0 \hat{\boldsymbol{x}} + \rho_0 \sin\phi_0 \hat{\boldsymbol{y}}$, with $1/e$-half- width waist $w(\boldsymbol{\rho}_0)$, whose axis in the direction of propagation makes an angle θ with the $\hat{\boldsymbol{x}}$-axis, leads to the following field at position $\boldsymbol{\rho} = (\rho, \phi)$ [9], [10]

$$E_z^{inc}(\boldsymbol{\rho}) = -\frac{\omega\mu_0}{4} H_0^{(2)}\left(k\sqrt{\rho^2 + \rho_b^2 - 2\rho_b\rho\cos(\phi_b - \phi)}\right), \tag{3.21}$$

where

$$r_b = \sqrt{\rho_0^2 - 2jb\rho_0\cos(\theta - \phi_0) - b^2},\ \mathcal{R}(\rho_b) > 0, \tag{3.22}$$

$$\cos\phi_b = \frac{\rho_0\cos\phi_0 - jb\cos\theta}{\rho_b}, \tag{3.23}$$

and with $\rho_0 = 22\lambda$, $\phi_0 = 45^o$, $\theta = 225^o$, $w(\boldsymbol{\rho}_0) = \lambda/2$ and $b = kw(\boldsymbol{\rho}_0)^2/2$. The wedge has an opening angle $\psi = 30^o$. A source region defined by the circular contour $\mathcal{C}'$ with center at $\rho'_c = 20\lambda$, $\phi'_c = 45^o$ and radius $R' = 3\lambda$ is positioned around the beam at $\boldsymbol{\rho}_0$. The coefficients $a_{q'}$ are computed by the substitution of (3.21) into (3.2). The total field is calculated via (3.12) in three completely arbitrarily-shaped regions circumscribed by the following circles:

- $\mathcal{C}_1$: $\phi'_{c,1} = 20^o$ and $\boldsymbol{\rho}_0 \cdot \hat{x} = -\boldsymbol{r}_{d,1} \cdot \hat{x}$, i.e. the group center lies beneath the point of origin of the Gaussian beam. Also, $R_1 = 2\lambda$.
- $\mathcal{C}_2$: $\phi'_{c,2} = 180^o$, $r_{d,2} = 10\lambda$, $R_2 = 3\lambda$.
- $\mathcal{C}_3$: $\phi'_{c,3} = 270^o$, $r_{d,3} = 15\lambda$, $R_3 = 4\lambda$.

The results are shown in Fig. 3.5. In the region of interest enclosed by $\mathcal{C}_1$, a standing wave pattern is observed, which is a consequence of the interference of the incoming beam with its reflection at the upper face of the wedge. The field inside $\mathcal{C}_2$ is mainly dominated by the incoming beam. Some slight variation in the amplitude of the field is visible because of the interference with the diffracted field. The region inside $\mathcal{C}_3$ lies in the shadow of the wedge. Only the diffracted field penetrates this region of space and hence, a low field amplitude is observed.

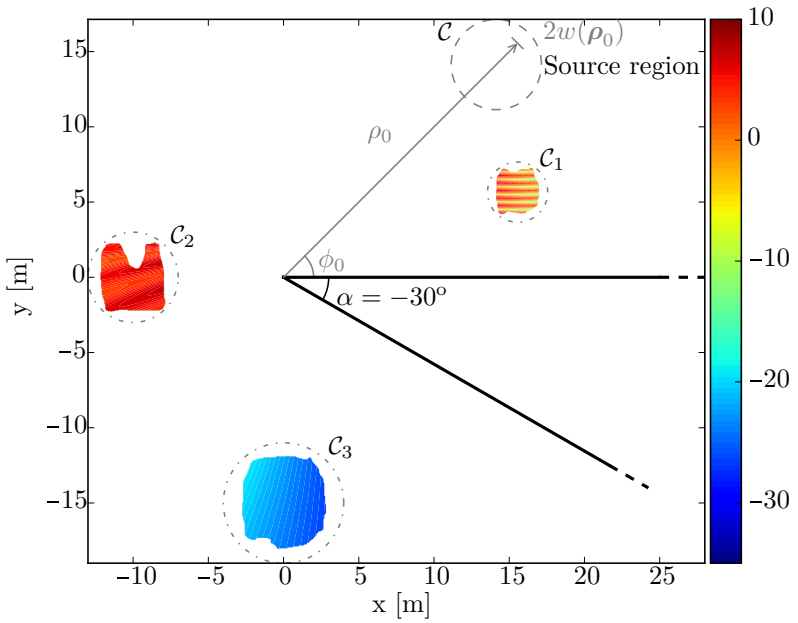

Figure 3.5: The total field in dB V/m for an incoming Gaussian beam in the presence of a perfectly conducting wedge.

3.3.4 Multiple diffraction centers

In the following example, the field behind a PEC slit is investigated. The slit is modeled as two separate semi-infinite straight PEC plates, such that classical UTD can be employed to describe single diffractions. Double diffractions can also be included in this case. The interaction between the two tips of the slit is taken into account by considering double diffractions as a product of separate UTD contributions [11]. The diffraction coefficient for double diffraction (D_{DD}) is thus given by

$$D_{DD} = D_1 \frac{\exp(-jkD)}{\sqrt{D}} D_2, \tag{3.24}$$

where D_1 and D_2 are the UTD diffraction coefficients for single diffraction at the first and second tip of the slit, respectively and D is the width of the slit. The coordinates belonging to the source region are now measured relative to the first diffraction tip, while the coordinates belonging to the region of interest are measured relative to the second diffraction tip.
The accuracy of the method is assessed for the example shown in Fig. 3.6. A

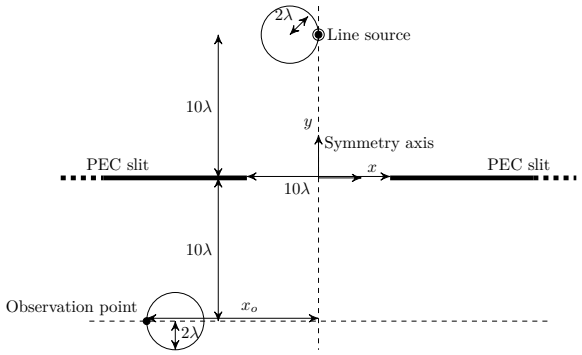

Figure 3.6: PEC slit excited by a line source.

PEC slit of width 10λ, λ being the wavelength, is symmetrically illuminated by an electric line source and a phase center is chosen at a distance 2λ from the source. Different observation points are chosen on a line parallel to the slit at a distance of 10λ, at x-coordinates $x_o \in [-23\lambda, 22\lambda]$. A phase center is assigned to each observation point at a distance 2λ to its right.
The RE with UTD, including double diffractions, as reference is plotted in Fig. 3.7. The RE remains below 10^{-4} in this case, even in the transition regions. We also treat the scattering of a 2^{nd} order Hermite-Gaussian beam at a PEC slit. Our method is able to deal with such complex illumination sources, as a set of sampled values of the source field on the boundary $\mathcal{C}'$ is already sufficient to determine the coefficients $a_{q'}$ in (3.1). The same slit as in Fig. 3.6 is used. The Hermite-Gaussian beam propagates along the symmetry axis of the slit. The beam has a waist λ at ten wavelengths above the slit. In order to determine the coefficients $a_{q'}$, the source field is sampled on a circle $\mathcal{C}'$ with radius 2λ. The total field behind the slit is computed in 10201 observation points within a square with $x \in [-5\lambda, 5\lambda]$ and $y \in [-15\lambda, -5\lambda]$. The computation took 47 s on a dual-core machine at 2.66 GHz with 8 GB of RAM.
The amplitude of the Hermite-Gaussian beam near the source region is shown in Fig. 3.8(a) and the total field amplitude behind the slit is plotted in Fig. 3.8(b).

3.4 Conclusion

We presented a high-frequency formalism which describes the diffraction of arbitrary incident wavefronts at edges. No matter how complex the light sources may be, it can now be easily dealt with. To start up the simulation, we merely need to know the field emitted by this source over a closed contour. It is proven how the diffracted field in a predefined region of interest can then be expressed in terms of this incident field and a limited set of coupling coefficients that take into account the arbitrary nature of the incident wavefront and its

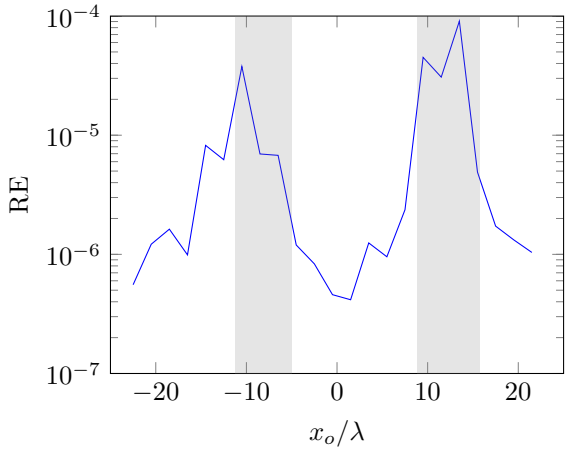

Figure 3.7: Accuracy compared to classical UTD for the example of Fig. 3.6. Transition regions are indicated by a gray background.

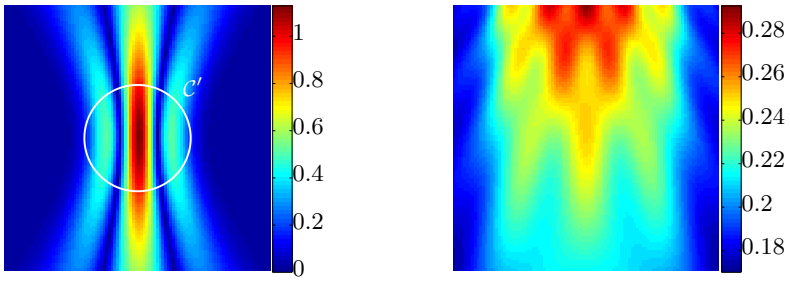

(a) Incoming field.

(b) Total field behind slit.

Figure 3.8: Field amplitude in V/m for diffraction of a Hermite-Gaussian beam at a PEC slit.

diffraction. In the limit of source regions and regions of interest of infinitesimally small dimensions, our solution is shown to reduce to conventional UTD, which confirms the validity of the proposed approach. In the case of a discrete line source, the method proved to be in excellent agreement with the analytic Green's function, especially after the introduction of the novel diffraction coefficient D'. The advocated formalism considerably increases the range of problems that can be studied using UTD. This is illustrated by investigating the diffraction of a Gaussian beam in Sec. 3.3.3 and a higher-order Hermite-Gaussian beam in Sec. 3.3.4, showing that no knowledge about the specific source choice needs to be used explicitly. Moreover, it is important to mention that the proposed

technique is easy to implement, as only standard FFT routines are leveraged.

References

[1] G. Karagounis, D. De Zutter, and D. Vande Ginste, "Computation of the Diffraction from Complex Illumination Sources in Extended Regions of Space", *Optics Express*, vol. 21, no. 25, pp. 30 379–30 391, 2013.

[2] G. Karagounis, D. De Zutter, and D. Vande Ginste, "A Generalized Uniform Theory of Diffraction Method for Complex Illumination Sources Accounting for Multiply-Diffracted Rays", in *Computational Electromagnetics International Workshop (CEM) in Izmir, Turkey*, 2015, pp. 1–2.

[3] J. B. Keller, "Geometrical Theory of Diffraction", *J. Opt. Soc. Am.*, vol. 52, no. 2, pp. 116–130, 1961.

[4] R. G. Kouyoumjian and P. H. Pathak, "A Uniform Geometrical Theory of Diffraction for an Edge in a Perfectly Conducting Surface", *Proc. IEEE*, vol. 62, no. 11, pp. 1448–1461, 1974.

[5] P. Pathak, W. Burnside, and R. J. Marhefka, "A Uniform GTD Analysis of the Diffraction of Electromagnetic Waves by a Smooth Convex Surface", *IEEE Trans. Antennas Propagat.*, vol. 28, no. 5, pp. 631–642, 1980.

[6] Y. Rahmat-Samii and R. Mittra, "Spectral Analysis of High-Frequency Diffraction of an Arbitrary Incident Field by a Half Plane – Comparison with Four Asymptotic Techniques", *Radio Science*, vol. 13, no. 1, pp. 31–48, 1978.

[7] *NIST Digital Library of Mathematical Functions*, http://dlmf.nist.gov/, Release 1.0.5 of 2012-10-01. [Online]. Available: `http://dlmf.nist.gov/`.

[8] Y. Z. Umul, "Scattering of a Gaussian Beam by an Impedance Half-Plane", *J. Opt. Soc. Am. A*, vol. 24, no. 10, pp. 3159–3167, 2007.

[9] A. C. Green, H. L. Bertoni, and L. B. Felsen, "Properties of the Shadow Cast by a Half-Screen when Illuminated by a Gaussian Beam", *J. Opt. Soc. Am.*, vol. 69, no. 11, pp. 1503–1508, 1979.

[10] G. Suedan and E. Jull, "Beam Diffraction by Half Planes and Wedges: Uniform and Asymptotic Solutions", *J*,

[11] M. Schneider and R. J. Luebbers, "A General, Uniform Double Wedge Diffraction Coefficient", *IEEE Trans. Antennas Propagat.*, vol. 39, no. 1, pp. 8–14, 1991.

4

A Hybrid MLFMM-UTD Method for the Solution of Very Large 2-D Electromagnetic Problems

G. Karagounis, D. De Zutter and D. Vande Ginste

This chapter is based on an article published in
IEEE Transactions on Antennas and Propagation [1] and a contribution to the
International Conference on Electromagnetics in Advanced Applications (ICEAA) (2015) [2].

★ ★ ★

MLFMM is combined with the UTD to model 2-D scattering problems including very large scatterers. The discretization of the very large scatterers is avoided by using ray-based methods. Reflections are accounted for by image source theory, while for diffraction a new MLFMM translation matrix is introduced. The translation matrix elements are derived based on a technique that generalizes the use of UTD for arbitrary source configurations and that efficiently describes the field over extended regions of space. $\mathcal{O}(n)$ scaling of the computational time and memory requirements is achieved for relevant structures, such as large antenna arrays in the presence of a wedge. The theory is validated by means of several illustrative numerical examples and is shown to remain accurate for NLoS scattering problems.

4.1 Introduction

EM solvers provide a means to deal with scattering problems in complex environments. For scattering problems involving piecewise homogeneous domains, BIEs are advantageous as only the unknown tangential fields on the boundary surfaces between domains have to be discretized. Discretizing the BIEs according to a MoM scheme results in a system with N unknowns and N equations that can be solved efficiently using an iterative solver. The memory requirements and the computational complexity of the matrix-vector multiplication scale as $\mathcal{O}(N^2)$. MLFMM reduces this scaling to $\mathcal{O}(N)$ or $\mathcal{O}(N \log N)$ [3], depending on the specific geometry of the problem. When the problem size becomes very large, memory requirements will however still grow excessively. High-frequency methods are useful in this case, as they provide asymptotic solutions to account for the presence of very large scatterers. Hybrid methods that combine MoM and high-frequency approaches are able to accurately deal with very large EM problems in the presence of complex geometries.
Field-based hybrid methods that combine GTD or UTD with MoM can avoid the discretization of large scatterers completely [4]–[10]. The current-based Physical Theory of Diffraction (PTD) is combined with MoM in [11]–[15]. The number of unknowns is reduced greatly on large smooth scatterers by only introducing MoM basis functions at discontinuities (points of diffraction). The matrix-vector multiplication time and the memory requirements of these methods is $\mathcal{O}(n^2)$, where n is now the number of unknowns obtained by only discretizing the boundaries of the scatterers treated by the BIE-MoM part of the hybrid scheme.
A hybrid MLFMM-UTD method has been presented in [16]. The method estimates the amplitude and phase of the UTD rays based on the MLFMM radiation pattern. This approximation proves sufficient to compute the amplitude of the total field in regions illuminated by the source. Here, we present a MLFMM-UTD hybrid method that provides accurate solutions in *all* regions where UTD is applicable. The novel method is based on the technique that generalizes the use of UTD as described in Chapter 3. Reflections at straight PEC scatterers are taken exactly into account using image source theory. For compact scatterers, such as large antenna arrays, the memory requirements and the computational time scale as $\mathcal{O}(n)$. Therefore, our method provides a valid and efficient alternative if the phase of the field also needs to be described accurately and for non line-of-sight (NLoS) problems.
In Sec. 4.2, we present the new MLFMM-UTD method. Also, a theoretical derivation of the proposed technique's computational complexity is given. Furthermore, an asymptotic expansion of the newly introduced MLFMM-UTD translator is derived and it is demonstrated that in this limit it is similar to the method described in [16]. Three numerical examples in Sec. 4.3 prove the accuracy of the method and demonstrate the good scaling properties of the algorithm. A fourth example illustrates the versatility of the method. In

Sec. 4.4, we give some concluding remarks.
In this chapter, we deal with 2-D TM problems. The $\hat{\boldsymbol{z}}$-axis is chosen as the axis of invariance.

4.2 Formalism

We consider an environment with N_S PEC scatterers. The pertinent EFIE is then given by (2.43). In a classical MoM scheme, as the background medium does not contain any scatterers, the Green's function used in (2.43) is the free space Green's function of (2.26).

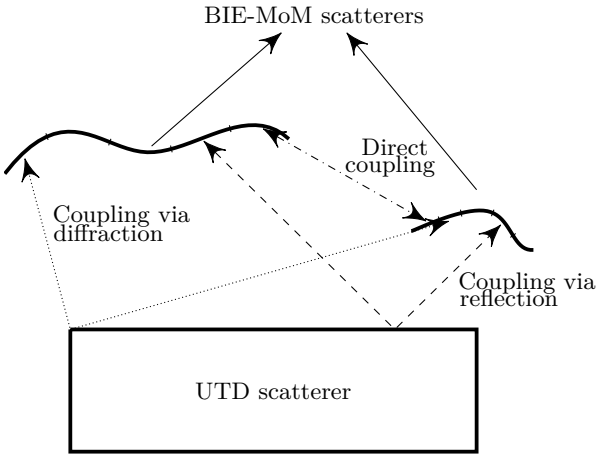

Figure 4.1: Generic example of the MoM-UTD method. The BIE-MoM scatterers are discretized, while the presence of the UTD scatterer is taken into account implicitly.

In a hybrid MoM-UTD scheme, some of the scatterers for which a canonical UTD solution is available are not discretized. This is shown in Fig. 4.1. Their presence is taken into account by adjusting the Green's function for ray-optical contributions, such as reflections and diffractions. The Green's function to be used in (2.43) then becomes:

$$G^{UTD}(\boldsymbol{\rho};\boldsymbol{\rho}') = G^{free}(\boldsymbol{\rho};\boldsymbol{\rho}') + G^{refl}(\boldsymbol{\rho};\boldsymbol{\rho}') + G^{diff}(\boldsymbol{\rho};\boldsymbol{\rho}') + \ldots \tag{4.1}$$

Higher-order interactions, such as reflection-reflection, diffraction-reflection etc., can be further added if necessary.
After discretization of the boundaries of all remaining scatterers, a linear system with n equations and n unknowns of the following form is derived from (2.43):

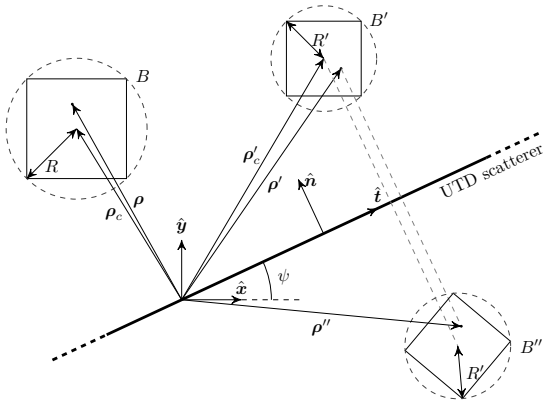

Figure 4.2: Illustration of the reflection at a long, straight surface of a UTD scatterer. The surface makes an angle ψ with the x-axis. The image of a source $\boldsymbol{\rho}'$ in source box B' is then $\boldsymbol{\rho}''$ in image box B''. Reflections are now described by the interaction between boxes B and B''.

$$\boldsymbol{V} = \boldsymbol{Z}^{tot} \cdot \boldsymbol{I} = \boldsymbol{Z}^{free} \cdot \boldsymbol{I} + \boldsymbol{Z}^{refl} \cdot \boldsymbol{I} + \boldsymbol{Z}^{diff} \cdot \boldsymbol{I} + \ldots \tag{4.2}$$

This system is solved for the unknown current vector $\boldsymbol{I}$. Iterative solvers seek at each iteration a better approximation for this vector, based on the matrix-vector product of $\boldsymbol{Z}^{tot}$ with the previous approximation. An efficient matrix-vector multiplication scheme for each term in the right-hand-side (RHS) of (4.2) is presented in what follows.

4.2.1 Direct coupling

The contributions due to direct coupling, i.e. the first term in the RHS of (4.2), can be handled by conventional MLFMM, as described in Sec. 2.3.3.

4.2.2 Coupling by reflection

The second term in the RHS of (4.2) is taken into account using image source theory. An illustration of a reflection at a UTD object is given in Fig. 4.2. Adopting an MLFMM implementation again, the radiation pattern of the image box B'' is to be translated to box B. The translation matrix is the same as in (2.53), where the distance r and angle α are now measured from the center of box B''. An interesting property is that the radiation pattern of the image box B'' can be expressed in terms of the radiation pattern of B'. Indeed, from (2.54) and using some basic vector algebra, for the reflection at a straight PEC scatterer elevated at angle ψ:

$$
\begin{aligned}
&\exp\left[j\boldsymbol{k}(\beta_{q'})\cdot(\boldsymbol{\rho}''-\boldsymbol{\rho}_c'')\right]\\
=&\exp\left[j\boldsymbol{k}(\beta_{q'})\cdot\{((\boldsymbol{\rho}'-\boldsymbol{\rho}_c')\cdot\hat{\boldsymbol{t}})\hat{\boldsymbol{t}}-((\boldsymbol{\rho}'-\boldsymbol{\rho}_c')\cdot\hat{\boldsymbol{n}})\hat{\boldsymbol{n}}\}\right]\\
=&\exp\left[jk\{((\boldsymbol{\rho}'-\boldsymbol{\rho}_c')\cdot(\hat{\boldsymbol{x}}\cos\psi+\hat{\boldsymbol{y}}\sin\psi))\cos(\psi-\beta_{q'})\right.\\
&\left.+((\boldsymbol{\rho}'-\boldsymbol{\rho}_c')\cdot(-\hat{\boldsymbol{x}}\sin\psi+\hat{\boldsymbol{y}}\cos\psi))\sin(\psi-\beta_{q'})\}\right]\\
=&\exp\left[jk\{((\boldsymbol{\rho}'-\boldsymbol{\rho}_c')\cdot\hat{\boldsymbol{x}})\cos(2\psi+\beta_{-q'})+((\boldsymbol{\rho}'-\boldsymbol{\rho}_c')\cdot\hat{\boldsymbol{y}})\sin(2\psi+\beta_{-q'})\}\right]\\
=&\mathcal{R}_{2\psi}\left\{\exp\left[j\boldsymbol{k}(\beta_{-q'})\cdot(\boldsymbol{\rho}'-\boldsymbol{\rho}_c')\right]\right\}
\end{aligned}
\tag{4.3}
$$

where $\mathcal{R}_{2\psi}$ denotes the transformation $\beta\rightarrow\beta+2\psi$. Such transformations are accurately and efficiently computed by using the FFT scheme shown in Fig. 4.3 [17]. The computational complexity remains unaffected by this additional step.

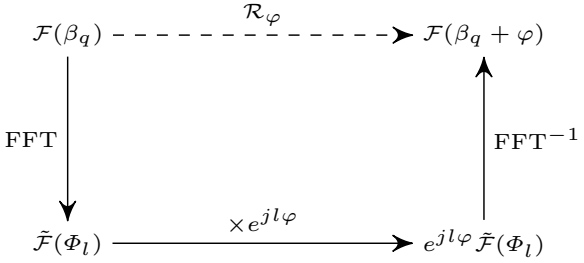

Figure 4.3: Efficient rotation of a sampled function $\mathcal{F}$ over an angle φ by use of FFTs.

Reflections are only taken into account by the above method if boxes B and B'' are sufficiently far apart and if every point within B can be reached by reflected rays. Else, the interaction will be handled at a lower level. If at the lowest level reflections are still not accounted for, they are taken into account by MoM.

4.2.3 Coupling by diffraction

The third term in the RHS of (4.2) deserves some more attention. We opt to use UTD to describe the coupling due to the diffraction at tips. Note that the plane waves, emerging in MLFMM, correspond to a decomposition of a far-field pattern in the angular spectrum and not to physically propagating plane waves arriving at the diffracting tip. Since canonical UTD solutions only exist for a limited number of illumination sources, such as a line source or an ordinary plane wave, it is not possible to use UTD directly in an MLFMM setting[1].

[1] A clear distinction between ordinary plane waves and the plane waves in MLFMM is that the wavevector of a plane wave in MLFMM is not equal to the translation direction. As

Therefore, in the envisaged hybrid scheme, we propose to generalize the UTD method such that (*i*) we can deal with arbitrary sources, in particular MLFMM source boxes; (*ii*) the diffracted field can be translated to IPWs at observation boxes. The UTD method described in Chapter 3 serves as a starting point. Now we adopt and extend this scheme to make it suitable for integration within an MLFMM solver. Consider the configuration in Fig. 4.4. A source box B', circumscribed by a circle $\mathcal{C}'$ with radius R', resides at position $\boldsymbol{\rho}'_c$ with respect to the diffracting tip of a semi-infinite PEC wedge with interior angle ψ. A similar notation is used for the observation box B. The incident field due to the arbitrary source configuration inside box B' is expanded into multipoles as follows:

$$E^{inc}(\boldsymbol{\rho}_o) = -\frac{\omega\mu_0}{4} \sum_{q'=-Q'}^{Q'} a_{q'} H_{q'}^{(2)} \left(k \left\|\boldsymbol{\rho}_o - \boldsymbol{\rho}'_c\right\|\right) e^{jq'\alpha'_o}, \tag{4.4}$$

for every observation point at position $\boldsymbol{\rho}_o$ outside $\mathcal{C}'$ ($\|\boldsymbol{\rho}_o - \boldsymbol{\rho}'_c\| > R'$). α'_o is the angle that $\boldsymbol{\rho}_o - \boldsymbol{\rho}'_c$ makes w.r.t. the $\hat{\boldsymbol{x}}$-axis. All coefficients $a_{q'}$ are independent of $\boldsymbol{\rho}_o$. The number of multipoles $2Q'+1$ again depends on the size R' of box B'. The diffracted field at a point $\boldsymbol{\rho}$ inside the observation box B is also expanded into multipoles, i.e.

$$E^{diff}(\boldsymbol{\rho}) = -\frac{\omega\mu_0}{4} \sum_{q=-Q}^{Q} b_q J_q \left(k \left\|\boldsymbol{\rho} - \boldsymbol{\rho}_c\right\|\right) e^{jq\alpha}. \tag{4.5}$$

The angle α is the angle that $\boldsymbol{\rho} - \boldsymbol{\rho}_c$ makes with the x-axis. The number of multipoles $2Q+1$ depends on R and, for generality, we describe the case where $R \neq R'$ and thus $Q \neq Q'$ (e.g. when B and B' belong to different MLFMM levels). Via the method described in Chapter 3, the two multipole expansions are related through

$$b_q = \sum_{q'=Q'}^{Q'} t_{qq'} a_{q'}. \tag{4.6}$$

The coupling coefficients $t_{qq'}$ are given by

the direction of propagation is a parameter of the UTD diffraction coefficient, UTD is not directly applicable on plane waves inherent to MLFMM.

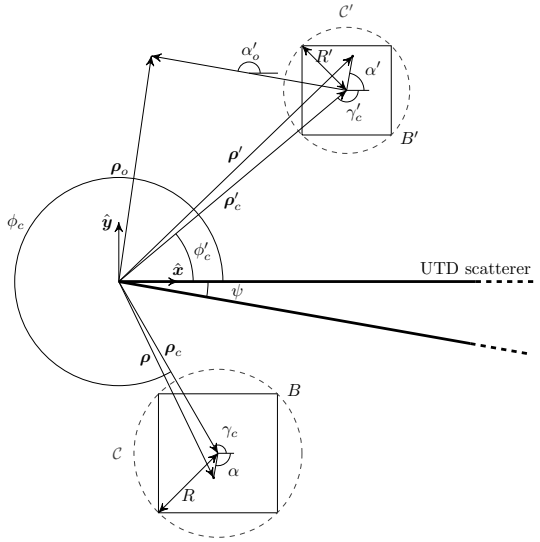

Figure 4.4: Illustration of the MLFMM-UTD geometry, where the UTD object is a PEC wedge with opening angle ψ situated between the MLFMM boxes.

$$t_{qq'} = \frac{1}{J_q(kR)} \frac{1}{J_{q'}(kR')} \sum_{n=-Q}^{Q} H_n^{(2)}(k\rho_c) J_n(kR) e^{-jn\gamma_c} \times \sum_{m=-Q'}^{Q'} \frac{1-j}{2} \sqrt{\pi k}\, d_{-n+q,m-q'} \times H_m^{(2)}(k\rho'_c) J_m(kR') e^{jm\gamma'_c}, \quad (4.7)$$

where $q' = -Q', \ldots, Q'$ and $q = -Q, \ldots, Q$. The angle γ'_c is the angle that $-\boldsymbol{\rho}'_c$ makes with the $\hat{\boldsymbol{x}}$-axis. The coefficients $d_{-n+q,m-q'}$ are given by

$$d_{s,l} = \frac{1}{4\pi^2} \int_{\mathcal{C}} \mathrm{d}\beta\, e^{-js\beta} \int_{\mathcal{C}'} \mathrm{d}\beta'\, e^{-jl\beta'} D_{UTD}\left(L; \boldsymbol{R}', \boldsymbol{R}\right). \quad (4.8)$$

The vector $\boldsymbol{R}$ denotes a position on $\mathcal{C}$, measured from the center $\boldsymbol{\rho}_c$ and at angle β. The parameter L in (4.8) is the well-known length parameter for line source illumination [18]

$$L = \frac{\left\|\boldsymbol{\rho}'_c + \boldsymbol{R}'\right\| \cdot \left\|\boldsymbol{\rho}_c + \boldsymbol{R}\right\|}{\left\|\boldsymbol{\rho}'_c + \boldsymbol{R}'\right\| + \left\|\boldsymbol{\rho}_c + \boldsymbol{R}\right\|}. \quad (4.9)$$

Now the coefficients $a_{q'}$ of the expansion (4.4) are written in terms of OPWs

and Bessel's integral is invoked to deal with $J_q\left(k\left\|\boldsymbol{\rho}-\boldsymbol{\rho}_c\right\|\right)$ in (4.5).
We first determine the connection between coefficients $a_{q'}$ in (4.4) and the OPWs in the far-field. The asymptotic approximation for the cylindrical harmonics $H_{q'}^{(2)}\left(k\left\|\boldsymbol{\rho}-\boldsymbol{\rho}_c'\right\|\right)$ in (4.4), for large argument values, is given by (2.29). Inserting this into (4.4) results in

$$E^{inc}(\boldsymbol{\rho}_o) \approx -\frac{1+j}{\sqrt{\pi k}}\frac{\omega\mu_0}{4}\frac{e^{-jk\left\|\boldsymbol{\rho}_o-\boldsymbol{\rho}_c'\right\|}}{\sqrt{\left\|\boldsymbol{\rho}_o-\boldsymbol{\rho}_c'\right\|}}\sum_{q'=-Q'}^{Q'} a_{q'}e^{jq'\left(\alpha_o'+\pi/2\right)}. \tag{4.10}$$

We now relate this to a well-known alternative derivation of the FMM expansion of the Green's function into plane waves [19]. In the presence of a single line source with current density J_s residing at $\boldsymbol{\rho}'$ ($\left\|\boldsymbol{\rho}'-\boldsymbol{\rho}_c'\right\| < \left\|\boldsymbol{\rho}_o-\boldsymbol{\rho}_c'\right\|$), $E^{inc}(\boldsymbol{\rho}_o)$ is also given by

$$E^{inc}(\boldsymbol{\rho}_o) = -J_s\frac{\omega\mu_0}{4}H_0^{(2)}\left(k\left\|\boldsymbol{\rho}_o-\boldsymbol{\rho}'\right\|\right). \tag{4.11}$$

In the far-field, using (2.29), the asymptotic approximation becomes

$$E^{inc}(\boldsymbol{\rho}_o) \approx -J_s\frac{1+j}{\sqrt{\pi k}}\frac{\omega\mu_0}{4}\frac{e^{-jk\left\|\boldsymbol{\rho}_o-\boldsymbol{\rho}'\right\|}}{\sqrt{\left\|\boldsymbol{\rho}_o-\boldsymbol{\rho}'\right\|}}. \tag{4.12}$$

We further introduce the Taylor expansion

$$\begin{aligned}\left\|\boldsymbol{\rho}_o-\boldsymbol{\rho}'\right\| &= \left\|\boldsymbol{\rho}_o-\boldsymbol{\rho}_c'-\left(\boldsymbol{\rho}'-\boldsymbol{\rho}_c'\right)\right\| \\ &\approx \left\|\boldsymbol{\rho}_o-\boldsymbol{\rho}_c'\right\| - \hat{\boldsymbol{k}}(\alpha_o')\cdot\left(\boldsymbol{\rho}'-\boldsymbol{\rho}_c'\right) + \mathcal{O}\left(\left\|\boldsymbol{\rho}_o-\boldsymbol{\rho}_c'\right\|^{-1}\right)\end{aligned} \tag{4.13}$$

in (4.12), with $\hat{\boldsymbol{k}}(\alpha_o') = \cos\alpha_o'\hat{\boldsymbol{x}} + \sin\alpha_o'\hat{\boldsymbol{y}}$. For the amplitude, we use only the zeroth-order approximation, while for the phase we keep the first-order term as well, yielding

$$E^{inc}(\boldsymbol{\rho}_o) \approx -\frac{1+j}{\sqrt{\pi k}}\frac{\omega\mu_0}{4}\frac{e^{-jk\left\|\boldsymbol{\rho}_o-\boldsymbol{\rho}_c'\right\|}}{\sqrt{\left\|\boldsymbol{\rho}_o-\boldsymbol{\rho}_c'\right\|}}\mathcal{F}(\alpha_o'), \tag{4.14}$$

in which $\mathcal{F}(\alpha_o') = J'e^{j\boldsymbol{k}(\alpha_o')\cdot\left(\boldsymbol{\rho}'-\boldsymbol{\rho}_c'\right)}$ and $\boldsymbol{k}(\alpha_o') = k\hat{\boldsymbol{k}}(\alpha_o')$. In the case of multiple sources, (4.14) remains valid, provided that $\mathcal{F}(\alpha_o')$ is replaced by a superposition of factors similar to the one derived here. The function $\mathcal{F}(\alpha_o')$ describes the radiation pattern of box B'. Comparison with (2.54) shows that the OPWs are sampled values of this radiation pattern. As $\mathcal{F}(\alpha_o')$ is quasi-bandlimited, it can be reconstructed from the OPWs [20]. Thereto, the appropriate kernel is the Dirichlet kernel, given by

$$D(\alpha'_o) = \sum_{q'=-Q'}^{Q'} \frac{e^{jq'\alpha'_o}}{2Q'+1}. \tag{4.15}$$

The reconstruction is performed in the following way:

$$\begin{aligned}\mathcal{F}(\alpha'_o) &\approx \sum_{p'=-Q'}^{Q'} \mathrm{OPW}_{p'} D(\alpha'_o - \beta_{p'}) \\ &= \frac{1}{2Q'+1} \sum_{q'=-Q'}^{Q'} e^{jq'\alpha'_o} \sum_{p'=-Q'}^{Q'} \mathrm{OPW}_{p'} e^{-jq'\beta_{p'}}\end{aligned} \tag{4.16}$$

Introduction of (4.16) into (4.14) and identification with (4.10) finally leads to

$$a_{q'} = \frac{1}{2Q'+1} \sum_{p'=-Q'}^{Q'} \mathrm{OPW}_{p'} e^{-jq'(\beta_{p'}+\pi/2)}. \tag{4.17}$$

Second, the Bessel functions $J_q\left(k\left\|\boldsymbol{\rho}-\boldsymbol{\rho}_c\right\|\right)$ in (4.5) can be described by a Fourier integral [21]:

$$J_q\left(k\left\|\boldsymbol{\rho}-\boldsymbol{\rho}_c\right\|\right) = \frac{1}{2\pi}\int_{2\pi} \mathrm{d}\beta^*\, e^{-j\boldsymbol{k}(\beta^*)\cdot(\boldsymbol{\rho}-\boldsymbol{\rho}_c)} e^{jq(\beta^*-\alpha+\pi/2)}. \tag{4.18}$$

The integral can also be discretized to yield a summation [22]

$$J_q\left(k\left\|\boldsymbol{\rho}-\boldsymbol{\rho}_c\right\|\right) e^{jq\alpha} = \frac{1}{2Q+1} \sum_{p=-Q}^{Q} e^{-j\boldsymbol{k}(\beta_p)\cdot(\boldsymbol{\rho}-\boldsymbol{\rho}_c)} e^{jq(\beta_p+\pi/2)}. \tag{4.19}$$

By introduction of the results (4.17) and (4.19) into (4.5), the diffracted field is finally written in a form that is compatible with MLFMM, i.e.

$$E^{diff}(\boldsymbol{\rho}) = -\frac{\omega\mu_0}{4} \sum_{p=-Q}^{Q} \mathrm{IPW}_p e^{-j\boldsymbol{k}(\beta_p)\cdot(\boldsymbol{\rho}-\boldsymbol{\rho}_c)}, \tag{4.20}$$

where the IPWs are now described by

$$\mathrm{IPW}_p = \sum_{p'=-Q'}^{Q'} \tilde{T}_{pp'} \mathrm{OPW}_{p'},\ p = -Q, \ldots, Q, \tag{4.21}$$

and the elements $\tilde{T}_{pp'}$ of the new translator $\tilde{\mathbf{T}}$ are given by

$$\tilde{T}_{pp'} = \frac{1}{(2Q+1)(2Q'+1)} \sum_{q=-Q}^{Q} \sum_{q'=-Q'}^{Q'} e^{jq(\beta_p+\pi/2)} t_{qq'} e^{-jq'(\beta_{p'}+\pi/2)}, \quad (4.22)$$

where $p' = -Q', \ldots, Q'$ and $p = -Q, \ldots, Q$. Note that, in contrast to the conventional MLFMM translator $\mathbf{T}$ in (2.53) used to describe the direct coupling, this new translator $\tilde{\mathbf{T}}$ is not diagonal, nor sparse. Nevertheless, in the next sections it will be shown that it can be computed efficiently during the setup of the algorithm and that the desired low computational complexity can be maintained.
The above scheme is used for boxes B and B' that are sufficiently far from tips of UTD scatterers and if for every observer in B, there is no point in B' for which a transition region is met. Else, the interactions will be handled at a lower level. If at the lowest level some diffraction interactions still need to be taken into account, MoM-UTD is used instead.

4.2.4 Efficient computation of the new translator $\tilde{\mathbf{T}}$

The computation of the coupling coefficients $t_{qq'}$ requires a double summation for every q and q'. Nonetheless, as the matrix with elements $d_{-n+q,m-q'}$ in (4.7) is Toeplitz, the matrix of coupling coefficients $t_{qq'}$ can still be computed in an efficient way following a routine similar to the one presented in [23]. Consider the following identities:

$$1 \equiv \sum_{s=-2Q}^{2Q} \delta_{s,q-n}, \ \forall q, n \in [-Q, Q], \quad (4.23)$$

$$\delta_{s,q-n} \equiv \frac{1}{4Q+1} \sum_{t=-2Q}^{2Q} e^{-j\frac{2\pi t}{4Q+1}[s-(q-n)]}. \quad (4.24)$$

By using both identities, it is readily shown that (4.7) can be written as

$$t_{qq'} = \frac{1}{J_q(kR)J_{q'}(kR')} \frac{1}{(4Q+1)(4Q'+1)} \times \sum_{u=-2Q}^{2Q} \sum_{v=-2Q'}^{2Q'} \left[\sum_{n=-Q}^{Q} H_n^{(2)}(k\rho_c) J_n(kR) e^{-jn(\gamma_c - \beta_u)} \right] \times \frac{1-j}{2}\sqrt{\pi k} \left[\sum_{s=-2Q}^{2Q} \sum_{l=-2Q'}^{2Q'} d_{s,l}\, e^{js\beta_u} e^{jl\beta_v} \right] \times \left[\sum_{m=-Q'}^{Q'} H_m^{(2)}(k\rho_c') J_m(kR') e^{jm(\gamma_c' - \beta_v)} \right] e^{-jq\beta_u} e^{jq'\beta_v}, \quad (4.25)$$

where $\beta_u = 2\pi u/(4Q+1)$ and $\beta_v = 2\pi v/(4Q'+1)$. The expression between square brackets in the third line inverts the FFT that appears in definition (4.8) of the coefficients $d_{s,l}$. In the second and fourth line one recognizes Graf's addition theorem [21]. Expression (4.25) thus reduces to

$$t_{qq'} = \frac{1}{J_q(kR)J_{q'}(kR')} \frac{1}{(4Q+1)(4Q'+1)} \times \sum_{u=-2Q}^{2Q} \sum_{v=-2Q'}^{2Q'} e^{-jq\beta_u} e^{jq'\beta_v} \frac{1-j}{2}\sqrt{\pi k}\, H_0^{(2)}\left(k \left\|\boldsymbol{\rho}_c + \boldsymbol{R}(\beta_u)\right\|\right) \times D_{UTD}\left(L; \boldsymbol{R}'(\beta_v), \boldsymbol{R}(\beta_u)\right) \times H_0^{(2)}\left(k \left\|\boldsymbol{\rho}_c' + \boldsymbol{R}'(\beta_v)\right\|\right). \quad (4.26)$$

$\boldsymbol{R}'(\beta_v)$ is a vector with length R' that makes an angle ϕ_v with the positive $\hat{\boldsymbol{x}}$-axis; similarly for $\boldsymbol{R}(\beta_u)$. The Hankel function in the second line of (4.26) originates from an approximation that was introduced in Chapter 3 and is identical to (2.29) with $\nu = 0$. This approximation can now be undone. We further substitute v by $-v$. The final expression for the coefficients $t_{qq'}$ becomes

$$t_{qq'} = \frac{1}{J_q(kR)J_{q'}(kR')} \frac{1}{(4Q+1)(4Q'+1)} \times \sum_{u=-2Q}^{2Q} \sum_{v=-2Q'}^{2Q'} e^{-jq\beta_u} e^{-jq'\beta_v} \frac{e^{-jk\|\boldsymbol{\rho}_c + \boldsymbol{R}(\beta_u)\|}}{\sqrt{\|\boldsymbol{\rho}_c + \boldsymbol{R}(\beta_u)\|}} \times D_{UTD}\left(L; \boldsymbol{R}'(-\beta_v), \boldsymbol{R}(\beta_u)\right) H_0^{(2)}\left(k \left\|\boldsymbol{\rho}_c' + \boldsymbol{R}'(-\beta_v)\right\|\right). \quad (4.27)$$

Thus, these coefficients can now be efficiently computed by means of a 2-D FFT. Once they are known, $\tilde{\mathbf{T}}$ in (4.22) can also be efficiently computed by a 2-D FFT.

4.2.5 Computational complexity

The interactions due to direct coupling are taken into account by using a traditional 2D-MLFMM scheme. The complexity depends on the geometry of the scatterers. If the scatterers are densely packed volume scatterers[2], such that the boxes of the quad-tree are fully filled, the complexity of traditional MLFMM methods is $\mathcal{O}(n)$ [3]. In the case of surface scatterers, for which the boxes are sparsely filled, the complexity is $\mathcal{O}(n \log n)$.
The coupling due to reflections follows the scheme of the traditional MLFMM, except for the additional conversion of the radiation pattern of a source box to that of the corresponding image source box. This operation is similar to the upsampling and downsampling of the radiation pattern by FFTs in MLFMM. Hence, this additional step does not alter the $\mathcal{O}(n)$ complexity. This additional step does not alter the complexity of the algorithm in the case of densely packed structures, i.e. it is $\mathcal{O}(n)$. For surface scatterers, the computational complexity increases to $\mathcal{O}(n \log^2 n)$. It is known, also for traditional MLFMM schemes, that the computational cost increases if FFT routines are invoked during aggregation and desaggregation [3].
The essential difference between the presented MLFMM-UTD method and the traditional MLFMM scheme manifests itself during the translation step of the diffraction coupling. Our algorithm uses an adaptive scheme that allows higher-level boxes, that are further away from the diffracting object, to interact with lower-level boxes, that reside closer to it. A box is considered to be far from the tip when the distance between the center of the box and the diffraction tip is about five times the box size and when this is not the case for its parent box. An example is shown in Fig. 4.5. The circular arcs in the figure show the boundaries beyond which the diffraction coupling can be treated at a higher MLFMM level.
The computational cost of the new scheme is now calculated. First, we show that the number of boxes at level l, bounded by arcs in Fig. 4.5, is independent of l. The radii of the arcs enclosing the boxes at level l in Fig. 4.5 are chosen proportional to R_l, i.e. the radius of a box at level l[3]. Thus, the area of the ring segment enclosing all boxes at level l scales with R_l^2. The area of a box at level l is also proportional to R_l^2. Thus, the ratio of the area of the ring segment to the area of a box, and consequently the number of boxes within the ring segment, is bounded. Therefore, there is an upper limit for the number of boxes treated at each level and we denote this upper limit C_{int}.
Second, we estimate the cost of a translation from a source box at level l' to an observation box at level l. As $\tilde{T}_{q,q'}$ is then a matrix of size $(2Q_l + 1) \times (2Q'_l + 1)$, a translation between the two boxes costs $(2Q_l + 1)(2Q'_l + 1)$ operations, where $2Q_l + 1$ and $2Q'_l + 1$ are the sampling rates at levels l and l', respectively. Due

[2] With a slight abuse of terminology, we refer by this to fully filled two-dimensional structures.

[3] The arcs have radius βR_l, where beta is a fixed constant, typically $\beta = 5$. Also, $R_l = 2R_{l+1}$ in a MLFMM quad tree.

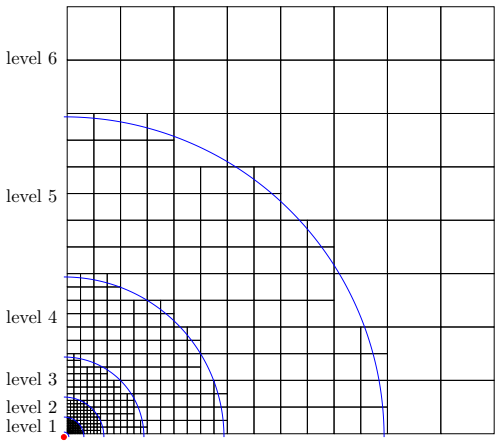

Figure 4.5: Boxes of a tree that interact with one another through diffraction by means of MLFMM. The diffraction tip is shown in red. The blue arcs show the admission boundaries for different levels in the MLFMM tree.

to (2.55), the sampling rates $2Q_l + 1$ and $2Q'_l + 1$ scale as $\mathcal{O}(R_l)$ and $\mathcal{O}(R'_l)$, respectively. Moreover, for densely packed volume scatterers, the number of unknowns within a box at level l, n_l, scales with the area of the box and thus with R_l^2. Therefore, $R_l \sim \sqrt{n_l}$ and $(2Q_l + 1)(2Q'_l + 1) \sim \sqrt{n_l n'_l}$.
Finally, the total complexity of the algorithm is estimated. As every of the at most C_{int} boxes at level l interacts with at most C_{int} other boxes at level l', the total number of computations between levels l and l' scales as $C_{int}^2 \sqrt{n_l n'_l}$. Interactions occur up to level $L - 1$. The total number of operations CC is found by summing over all pairs of levels l and l', i.e.

$$CC = C_{int}^2 \sum_{l,l'=1}^{L-1} \sqrt{n_l n_{l'}}. \tag{4.28}$$

The number of unknowns in a box at the lowest level is always fixed, say m. This number stems, traditionally, from a $\lambda/10$ discretization. As in a densely packed quad-tree, the number of unknowns grows by a factor of four at each level, $n_l = 4^l m$. Consequently, (4.28) reduces to

$$\begin{aligned} CC &= C_{int}^2 m \sum_{l,l'=1}^{L-1} 2^{l+l'} \\ &= C_{int}^2 m \left(2^L - 1\right)^2. \end{aligned} \tag{4.29}$$

Moreover, at the highest level L, all unknowns are members of one big box, thus $4^L m = n$. This leads to

$$CC = C_{int}^2 m \left(\sqrt{\frac{n}{m}} - 1 \right)^2 , \tag{4.30}$$

from which we conclude that $CC \propto \mathcal{O}(n)$.

4.2.6 Asymptotic approximation of $\tilde{\mathbf{T}}$

Except for compact volume scatterers, the MLFMM-UTD scheme discussed up to now will result in a $\mathcal{O}(n^2)$ complexity, owing to the full translator $\tilde{\mathbf{T}}$. So, the translation step is the bottleneck of the current MLFMM-UTD scheme. In this section, we show that, for boxes that are far from the diffracting tip, the translator can be decomposed in terms that are either related to the source box or the observation box. The decomposition then allows performing the translation for the coupling due to diffraction in three consecutive steps:

- Translation of the OPWs to the diffracting tip and desaggregation.
- Scaling of the incoming field with diffraction coefficients.
- Translation of the result to the observation groups.

This is very similar to traditional MLFMM and it results in an $\mathcal{O}(n \log n)$ complexity for sparse scatterers. This improvement in computational complexity comes at the loss of accuracy, because of the asymptotic approximation of the UTD diffraction coefficient. It will become apparent from the following derivation that the zeroth-order asymptotic approximation of $\tilde{\mathbf{T}}$ is closely related to the MLFMM-UTD scheme presented in [16].
We repeat the expression for the UTD diffraction coefficient (A.46), derived in Appendix A, for a line source at $\boldsymbol{\rho}' = (\rho', \phi')$ and an observation point at $\boldsymbol{\rho} = (\rho, \phi)$:

$$D_{UTD}(L; \boldsymbol{\rho}', \boldsymbol{\rho}) = -\frac{\exp(-j\pi/4)}{2n\sqrt{2\pi k}} \left[\cot\left(\frac{\pi + (\phi - \phi')}{2n} \right) F(kL\alpha^+(\phi - \phi')) + \right. \tag{4.31}$$

$$\cot\left(\frac{\pi - (\phi - \phi')}{2n} \right) F(kL\alpha^-(\phi - \phi')) \pm \left(\cot\left(\frac{\pi + (\phi + \phi')}{2n} \right) F(kL\alpha^+(\phi + \phi')) \right. \tag{4.32}$$

$$\left. \left. + \cot\left(\frac{\pi - (\phi + \phi')}{2n} \right) F(kL\alpha^-(\phi + \phi')) \right) \right]. \tag{4.33}$$

The definition of the functions L, F and $\alpha^{\pm}$ are given in Appendix A. We now seek an approximation of the diffraction coefficient for boxes that are far from the diffraction tip compared to their box size, i.e. an approximation in terms of small R/ρ_c and R'/ρ_c'. First, the angle ϕ' between the vector $\boldsymbol{\rho}' = \boldsymbol{\rho}_c' + \boldsymbol{R}'(\beta')$ and the $\hat{\boldsymbol{x}}$-axis is given by

$$\phi'(\beta') = \operatorname{atan}\left(\frac{\rho_c' \sin\phi_c' + R'\sin\beta'}{\rho_c'\cos\phi_c' + R'\cos\beta'}\right) = \phi_c' - \frac{R'}{\rho_c'}\sin(\phi_c' - \beta') + \mathcal{O}\left(\left(\frac{R'}{\rho_c'}\right)^2\right), \tag{4.34}$$

where the Taylor approximation in terms of small R'/ρ_c' is introduced. A similar expression may be found for $\phi(\beta)$. The expansion (4.34) is used to obtain a Taylor expansion of the cotangent functions in (4.33). The Taylor series of the cotangent function is:

$$\cot(x+\epsilon) = \cot x - \frac{1}{\sin^2 x}\epsilon + \mathcal{O}\big(\epsilon^2\big),\ \epsilon \ll 1$$

Second, a zeroth-order approximation of the function $F(x)$ in (4.33) is retained. The asymptotic approximation of the diffraction coefficient now becomes

$$\begin{aligned} D_{UTD}(L;\boldsymbol{R}'(\beta'),\boldsymbol{R}(\beta)) = D_{UTD}(L;\boldsymbol{\rho}_c',\boldsymbol{\rho}_c) + \frac{R'}{\rho_c'}C'(\boldsymbol{\rho}_c',\boldsymbol{\rho}_c)\sin(\phi_c'-\beta') \\ + \frac{R}{\rho_c}C(\boldsymbol{\rho}_c',\boldsymbol{\rho}_c)\sin(\phi_c-\beta) + \mathcal{O}\left(\left(\frac{R'}{\rho_c'}\right)^2\right) + \mathcal{O}\left(\left(\frac{R}{\rho_c}\right)^2\right), \end{aligned} \tag{4.35}$$

where

$$\begin{aligned} C'(\boldsymbol{\rho}_c',\boldsymbol{\rho}_c) = \frac{j}{8n^2}\sqrt{\frac{2j}{\pi k}}\Bigg[&- \frac{F(kL\alpha^+(\phi_c-\phi_c'))}{\sin^2\left(\frac{\pi+\phi_c-\phi_c'}{2n}\right)} + \frac{F(kL\alpha^-(\phi_c-\phi_c'))}{\sin^2\left(\frac{\pi-\phi_c+\phi_c'}{2n}\right)} \\ &\pm \left(\frac{F(kL\alpha^+(\phi_c+\phi_c'))}{\sin^2\left(\frac{\pi+\phi_c+\phi_c'}{2n}\right)} - \frac{F(kL\alpha^-(\phi_c+\phi_c'))}{\sin^2\left(\frac{\pi-\phi_c-\phi_c'}{2n}\right)}\right)\Bigg] \\ C(\boldsymbol{\rho}_c',\boldsymbol{\rho}_c) = \frac{j}{8n^2}\sqrt{\frac{2j}{\pi k}}\Bigg[&\frac{F(kL\alpha^+(\phi_c-\phi_c'))}{\sin^2\left(\frac{\pi+\phi_c-\phi_c'}{2n}\right)} - \frac{F(kL\alpha^-(\phi_c-\phi_c'))}{\sin^2\left(\frac{\pi-\phi_c+\phi_c'}{2n}\right)} \\ &\pm \left(\frac{F(kL\alpha^+(\phi_c+\phi_c'))}{\sin^2\left(\frac{\pi+\phi_c+\phi_c'}{2n}\right)} - \frac{F(kL\alpha^-(\phi_c+\phi_c'))}{\sin^2\left(\frac{\pi-\phi_c-\phi_c'}{2n}\right)}\right)\Bigg]. \end{aligned}$$

Introducing (4.35) into (4.8), an analytical result for $d_{s,l}$ is easily obtained. After some mathematical manipulations, one obtains the following approximation for

the matrix elements of $\tilde{\mathbf{T}}$

$$\begin{aligned}\tilde{T}_{pp'} \approx \sqrt{\frac{\pi k}{2j}}\Bigg[&D_{UTD}(L;\boldsymbol{\rho}_c',\boldsymbol{\rho}_c)\breve{T}_p^{(0)}(k,\rho_c,\phi_c)\breve{T}_{p'}^{(0)}(k,\rho_c',\gamma_c')\\ &+\frac{1}{2j}\frac{R'}{\rho_c'}C'(\boldsymbol{\rho}_c',\boldsymbol{\rho}_c)\breve{T}_p^{(0)}(k,\rho_c,\phi_c)\breve{T}_{p'}^{(1)}(k,\rho_c',\gamma_c',R')\\ &+\frac{1}{2j}\frac{R}{\rho_c}C(\boldsymbol{\rho}_c',\boldsymbol{\rho}_c)\breve{T}_p^{(1)}(k,\rho_c,\phi_c,R)\breve{T}_{p'}^{(0)}(k,\rho_c',\gamma_c')\Bigg],\end{aligned} \tag{4.36}$$

with $\breve{T}_p^{(0)}(k,r,\alpha) \equiv T_{pp}$ from (2.53) and

$$\begin{aligned}\breve{T}_p^{(1)}(k,r,\alpha,R) = \frac{1}{2Q+1}\sum_{q'=-Q}^{Q}\Bigg[&H_{q'+1}^{(2)}(kr)\frac{J_{q'+1}(kR)}{J_{q'}(kR)}\\ &-H_{q'-1}^{(2)}(kr)\frac{J_{q'-1}(kR)}{J_{q'}(kR)}\Bigg]\exp\left(jq'(\alpha-\beta_p-\pi/2)\right).\end{aligned} \tag{4.37}$$

Introduction of (4.36) into (4.21) yields

$$\mathrm{IPW}_p \approx \breve{T}_p^{(0)}\sqrt{\frac{\pi k}{2j}}D_{UTD}(L;\boldsymbol{\rho}_c',\boldsymbol{\rho}_c)\sum_{p'=-Q}^{Q}\breve{T}_{p'}^{(0)}\mathrm{OPW}_{p'}+\ldots, \tag{4.38}$$

in which we have omitted the arguments of the translators for brevity. From (4.38), it follows that the translation occurs in three steps as described at the beginning of this section. As the translation from the source boxes to the diffraction tip, as well as the translation from the diffraction tip to the observation boxes, are performed by diagonal translators, the complexity of this MLFMM-UTD scheme is the same as the complexity of MLFMM up to a constant factor.
The reader notices that by retaining only the first term of the translator (4.36) in (4.38), i.e.

$$\tilde{T}_{pp'} \approx \sqrt{\frac{\pi k}{2j}}D_{UTD}(L;\boldsymbol{\rho}_c',\boldsymbol{\rho}_c)\breve{T}_p^{(0)}(k,\rho_c,\phi_c)\breve{T}_{p'}^{(0)}(k,\rho_c',\gamma_c'), \tag{4.39}$$

first, the field due to the sources in the source box is evaluated at the diffraction tip, next, the incoming field is scaled with a UTD diffraction coefficient and then, the result is translated to the observation box. Moreover, only the MLFMM translator of (2.53) is involved. This is very similar to the MLFMM-UTD scheme presented in [16], where diffraction is described by the diffraction coefficient related to the ray path connecting the diffraction tip to the centers of the interacting boxes. Additionally in [16], a FAFFA approximation for the

radiation patterns of the boxes is introduced, as well as the high-frequency approximation of the translator between the diffracting tip and the observation boxes.

4.3 Results

We present three examples. First, the numerical accuracy of our method is assessed by comparing the results of our method to the MoM-UTD scheme proposed in [4] and to an alternative MLFMM-UTD formalism, that is somewhat similar to the one presented in [16], as detailed below. Next, the efficiency of our method is demonstrated. Finally, an application example is shown, comprising two large antenna arrays.

4.3.1 Accuracy test

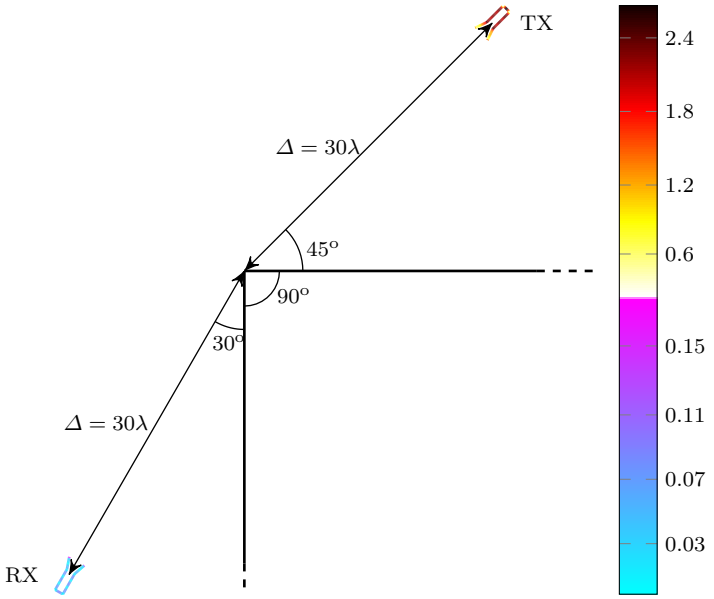

Figure 4.6: Amplitude of the unknown current expansion coefficients on the surface of the horns (in A/m). The currents are computed using our MLFMM-UTD method. λ is the wavelength in the background medium.

In the first example, the NLoS configuration depicted in Fig. 4.6 is investigated. We explicitly opt for a NLoS configuration because the diffraction contribution is then dominant. Two PEC horn antennas are in NLoS due to the presence of an

infinite 90° PEC wedge. The geometry of the 2-D horns is detailed in Fig. 4.7. Two 2λ long parallel plates, where λ is the wavelength in the background medium, serve as a waveguide that suppresses higher-order modes and supports the propagation of the fundamental mode. The opening of the horn is tapered. The transmitting antenna is fed by a 1 A/m line source at a quarter-wavelength from its back-end. The center-of-mass (CoM) of the transmitter (TX) resides at a distance of $\Delta = 30\lambda$ from the tip of the wedge at an angle of 45° w.r.t. the upper face of the wedge. The receiving antenna's (RX) CoM resides at the same distance Δ and at an angle of 30° w.r.t. the left face of the wedge. Both antennas are directed towards the tip of the wedge. Each antenna is discretized into 105 segments of length $\lambda/15$. Each antenna is assigned a different MLFMM tree, for which the box size at the lowest level in the MLFMM tree is $\lambda/2$. The total number of levels in each tree is $L = 4$. The diffraction interactions are treated at the highest level, in accordance with the adaptive scheme presented in Sec. 4.2.5. The amplitude of the currents along the surface of the antennas, computed by our method, is shown on Fig. 4.6.

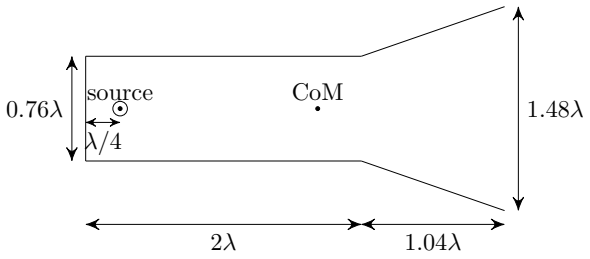

Figure 4.7: Geometric details of the horns used in Fig. 4.6.

As a reference solution, we implemented the classical MoM-UTD [4]. Additionally, for further comparison, we also implemented an alternative 2-D hybrid MLFMM-UTD scheme, that is somewhat similar to the one presented in [16]. In this alternative scheme, coupling through reflection and diffraction is treated by traditional UTD from the centers of the interacting boxes. The incoming field at the reflection/diffraction point $\boldsymbol{\rho}$ is determined by employing the following far-field approximation (see also Fig. 2.7):

$$G^{free}(\boldsymbol{\rho};\boldsymbol{\rho'}) \approx e^{j\boldsymbol{k_i}\cdot(\boldsymbol{\rho'}-\boldsymbol{\rho_s^c})} T_L^{FF}, \tag{4.40}$$

where $\boldsymbol{k_i}$ is a vector that points from the center of the source box $\boldsymbol{\rho_s^c}$ to the reflection/diffraction point $\boldsymbol{\rho}$ and $|\boldsymbol{k_i}| = k$. Moreover, T_L^{FF} is the 2-D far-field translation operator:

$$T_L^{FF} = \frac{1+j}{\sqrt{\pi k}} \frac{e^{-jkr}}{\sqrt{r}} \tag{4.41}$$

with $r = \left\|\boldsymbol{\rho} - \boldsymbol{\rho}_{\boldsymbol{s}}^{\boldsymbol{c}}\right\|$. The required direction of incidence $\boldsymbol{k_i}$ is interpolated from the available OPWs by Lagrange interpolation using three interpolation points. After reflection/diffraction, the appropriate ray contribution towards the center of the observation box is projected onto the three neighboring IPWs.
Moreover, a one-level FMM-UTD employing the asymptotic approximations (4.36) and (4.39) for $\tilde{\mathbf{T}}$ from Sec. 4.2.6 is also implemented.
The current density obtained on the 210 segments of the horns is computed with the three techniques. For each segment, the relative error (RE) is defined as

$$\mathrm{RE} = \left| \frac{J_{z,hybrid} - J_{z,MoM-UTD}}{J_{z,MoM-UTD}} \right|, \tag{4.42}$$

where $J_{z,hybrid}$ is the result from either our newly proposed hybrid technique or from the alternative scheme. $J_{z,MoM-UTD}$ is obtained by means of the reference MoM-UTD [4].

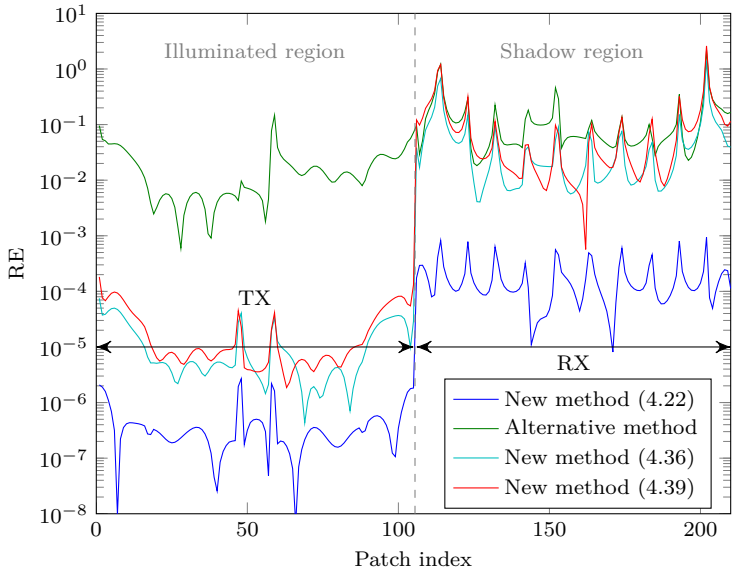

Figure 4.8: Relative error on the currents compared to the MoM-UTD solution.

In the illuminated region, in which the transmitter resides, direct and reflection contributions dominate diffraction contributions. As shown in Fig. 4.8, our methods prove to be very accurate in this illuminated region, as reflections are also exactly taken into account. The alternative method uses the canonical UTD solutions to account for reflections. This explains the large difference in accuracy between our methods and the alternative method for the illuminated part. In the shadow region, where the receiver horn resides, the accuracy is

purely determined by the diffraction contribution. It is seen that a RE of less than 0.1% is easily reached with our new technique with full translator. The alternative MLFMM-UTD formalism and the two methods employing the asymptotic approximations for the translator $\tilde{\mathbf{T}}$ are able to model the amplitude of the field, but fail to accurately predict the phase of the field. This leads to the poorer RE results.
The test is now repeated for a range of values of Δ and the results are shown in Fig. 4.9. The mean RE over the patches of each of the antennas is plotted. This mean RE defined as

$$\text{Mean RE} = \frac{1}{M}\sum_{i=1}^{M}\text{RE}_i, \tag{4.43}$$

where the summation runs over all M patches of the pertinent horn. The accuracy of all MLFMM-UTD schemes increases with increasing distance, as the far-field conditions on which UTD relies are better fulfilled. Note that for the receiver horn, the method employing the zeroth-order asymptotic approximation of $\tilde{\mathbf{T}}$ and the alternative method provide very similar results in terms of accuracy, as expected from the explanation given in Sec. 4.2.6.

4.3.2 Multiple diffraction centers

A second accuracy test concerns the scattering at a PEC square. Because of the compactness of the UTD object in this case, it is possible to validate our technique against exact full-wave simulations. The accuracy of the method is validated for the example of Fig. 4.10. A transmitting horn antenna is placed at 30λ from the upper left corner of a large square PEC scatterer, at an angle of 30^{o} w.r.t. the upper face. A receiving horn is placed in the shadow of the large scatterer, at 30λ from the corner and at an angle of 30^{o} w.r.t. the left face. A $\lambda/15$ discretization leads to $n = 210$ unknowns. A line source with current strength 1 A/m is placed along the symmetry axis of the TX, at $\lambda/4$ of its back-end. The single diffractions by all pertinent edges of the PEC square are taken into account. Doubly diffracted rays are also taken into account by the diffraction coefficient presented in [24]. Double diffractions occur for every pair of diffraction tips of which *(i)* the first tip is in the LoS of the source box, *(ii)* the second is in the LoS of the observation box and *(iii)* diffraction tips are different endpoints of the same face of the square. For the computation of the translator, coordinates belonging to the source box are expressed relative to the first diffraction tip, while coordinates belonging to the observation box are expressed relative to the second diffraction tip. All single and double diffractions are then superimposed in (4.27).
The currents are compared to these obtained by a traditional MLFMM solver, which also discretizes the large square cylinder, leading to 2000 extra unknowns.

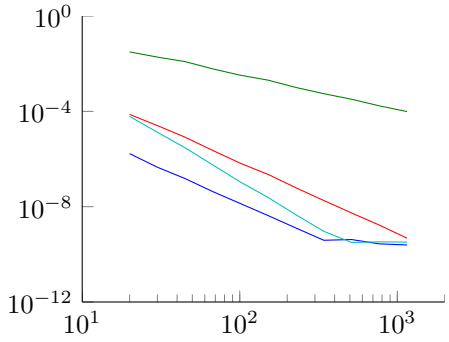

(a) Transmitter.

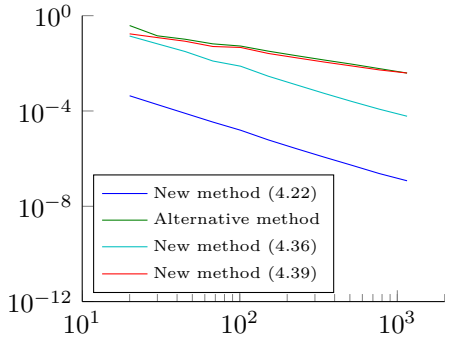

(b) Receiver.

Figure 4.9: Mean RE as a function of Δ.

The MLFMM solver required 10 minutes to solve the MoM system and 23.7 MB of memory. In contrast, the MLFMM-UTD method only needed 0.7 s and 1.9 MB of memory. The RE, with the full-wave MLFMM solution as a reference, is plotted in Fig. 4.11. A relative error of 1% is obtained for the currents on the RX, indicating that also the phase is modeled very well by our method.

A similar example, but with the receiving horn in the deep shadow of the transmitting horn as shown in Fig. 4.12, is also investigated. The current density on the surface of both horns is shown in Fig. 4.13. Again a good correspondence is found between our novel method and the full-wave reference solution.

4.3.3 Efficiency test

To test the computational complexity of our method, we consider two $m \times m$ arrays of PEC plates as shown in Fig. 4.14. The length of each plate is 0.5λ,

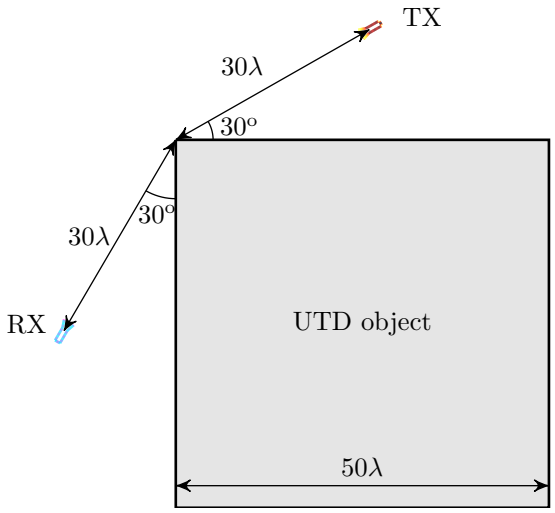

Figure 4.10: Geometry for the accuracy test. The induced current densities on the horns are shown in color.

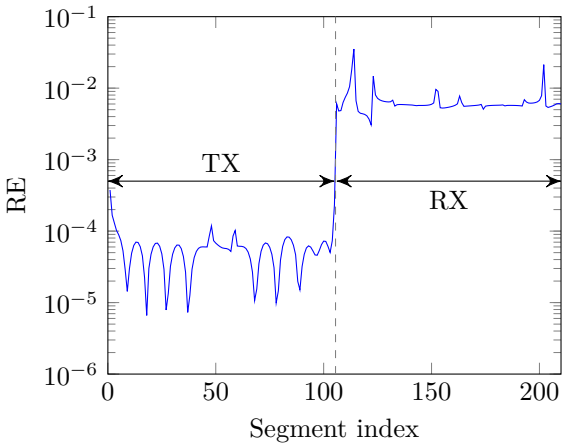

Figure 4.11: Relative error on the currents for square UTD object compared to an MLFMM solution.

with λ the wavelength in the background medium. The distance between the CoMs of neighboring plates is 0.6λ. The two arrays are separated by a half infinite, infinitely thin PEC plate. We increase m from 1 to 365. The size of the largest array is then $218.4\lambda \times 218.9\lambda$. The closest point of both arrays to the tip of the half-infinite scatterer is fixed at 10λ. Each array is assigned a different MLFMM tree, for which the box size at the lowest level is $\lambda/4$. The

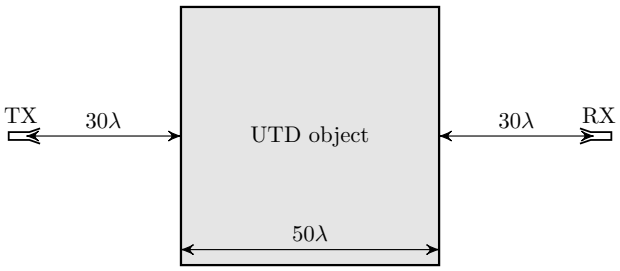

Figure 4.12: Geometry for an additional test in the deep shadow of a PEC square.

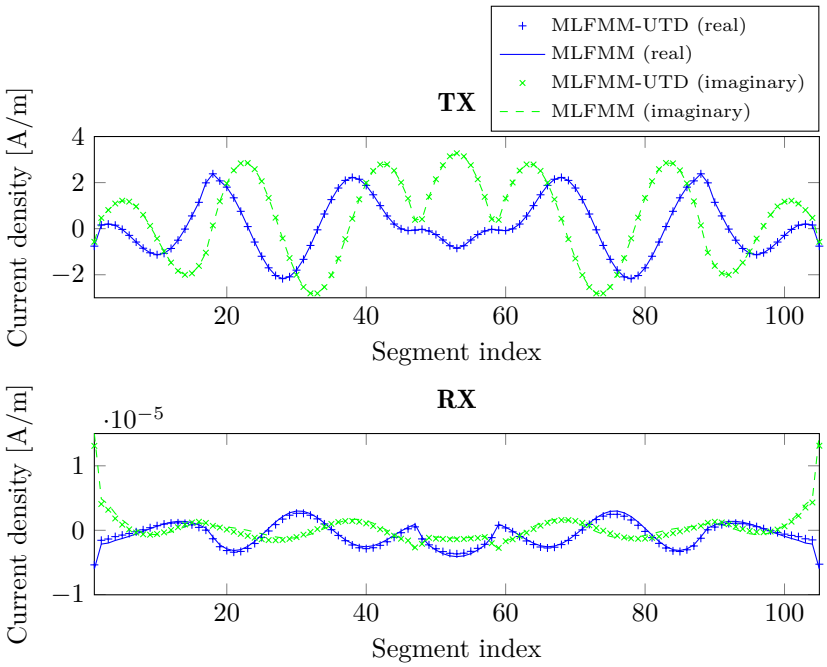

Figure 4.13: Real and imaginary part of the current density on the horns for the geometry shown in Fig. 4.12.

adaptive scheme presented in Sec. 4.2.5 is employed. To each plate, five basis functions are assigned. The *single* process jobs were performed on a processor of an Intel Xeon CPU E5-2680 twelve-core machine at 2.5 GHz with 512 GB of RAM.

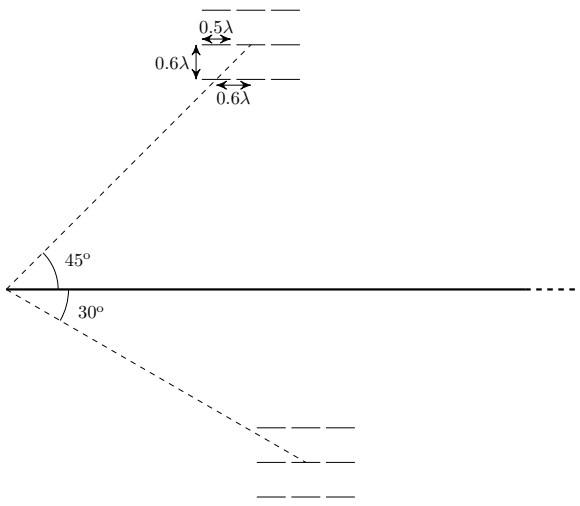

Figure 4.14: Geometry for the complexity tests. The plates form two $m \times m$ arrays, where here $m = 3$. The arrays are separated by a long straight PEC scatterer.

In Fig. 4.15, the scaling of the CPU time during the setup phase of the algorithm (i.e. allocating memory, filling up matrices, etc.), the CPU time for one matrix-vector multiplication and the allocated memory are plotted. For our newly proposed MLFMM-UTD method and the alternative MLFMM-UTD method, the CPU time and the memory requirements scale as $\mathcal{O}(n)$. The MoM-UTD scheme [4] has an $\mathcal{O}(n^2)$ complexity. Even for a very low number of unknowns, both MLFMM-UTD schemes are already faster than MoM-UTD during setup. This is due to the dominant contribution of the computation of the UTD coefficients in MoM-UTD. For the matrix-vector multiplication time and the memory requirements, the cross-over point for our novel method is found at about 2500 unknowns. These results are in line with conventional MLFMMs and demonstrate that our MLFMM-UTD method allows the modeling of very large structures.

4.3.4 Application example

In this section, we investigate a structure that illustrates the applicability of the proposed MLFMM-UTD scheme for problems including very large scatterers. The example consists of two radiating horn-antenna arrays that are constructed

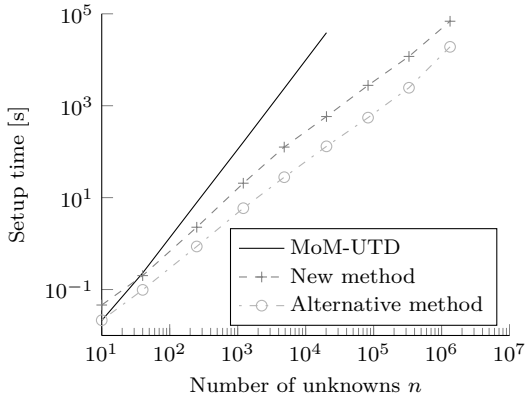

(a) CPU time during the setup phase.

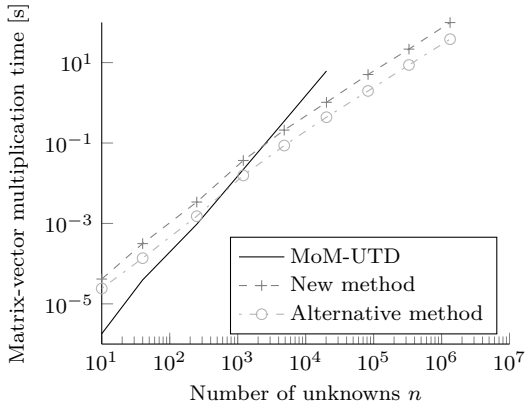

(b) CPU time for one matrix-vector multiplication.

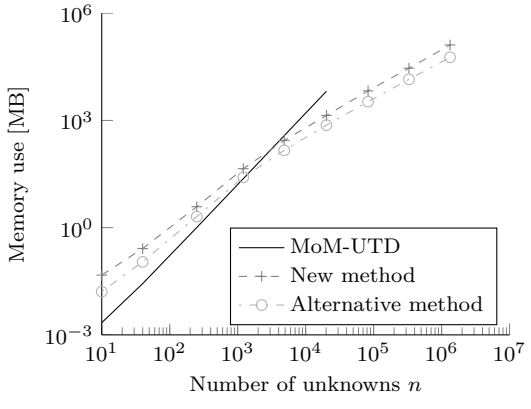

(c) Allocated memory.

Figure 4.15: Scaling of the resources for an increasing number of unknowns.

using a rectangular lattice of PEC circular cylinders. The geometry of one such a horn-antenna array is shown in Fig. 4.16. By introducing line defects through the lattice, a feed network of waveguides is constructed. The waveguides lead to the front of the lattice, where horns are constructed by gradually tapering the openings. Such structures have been presented in literature in the context of electromagnetic crystals [25].

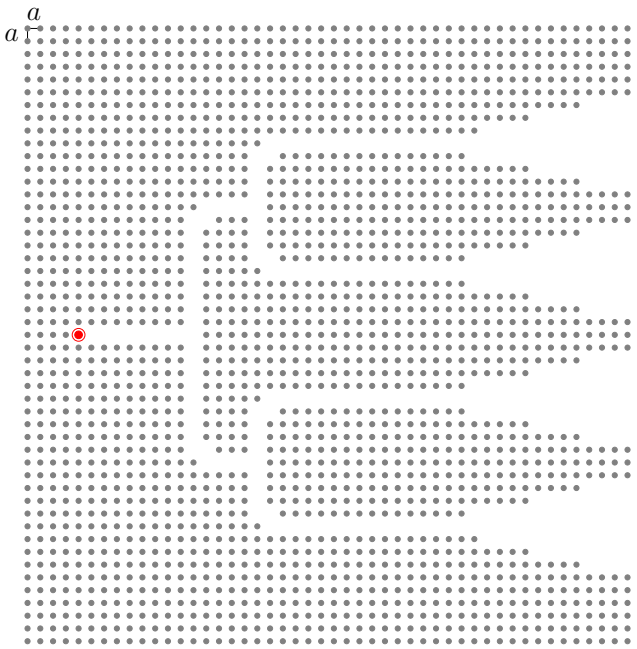

Figure 4.16: Horn-antenna array consisting of 1978 PEC cylinders (gray). The array is fed by a line source at the location of the red circle.

The taper length for the horns is $13a$, with an opening angle of $\text{atan}(3/13) \approx 13^{\text{o}}$, where $a = 0.4\lambda$ is the distance between the center of two neighboring cylinders and λ is the wavelength in the background medium. The radius of the cylinders is 0.08λ. We adopt the constellation of Fig. 4.14 again, but replace the plate arrays by the horn-antenna arrays shown in Fig. 4.16. Both horn-antenna arrays are oriented towards the tip of the plate. Each horn antenna comprises 1978 cylinders. Ten unknowns are introduced on the surface of each cylinder. In total, the problem consists of $n = 39560$ unknowns. Each antenna is assigned a different MLFMM tree, for which the size of the box at the lowest level is $\lambda/2$. The total number of levels in each tree is $L = 7$. The diffraction interactions are again treated at the highest level, in accordance with the adaptive scheme presented in Sec. 4.2.5. The top array is excited by a line source with current density 1 A/m (see also Fig. 4.16). Both horn antennas' COMs reside at a distance of 200λ from the tip of the wedge. The complete geometry is shown in

Fig. 4.17.

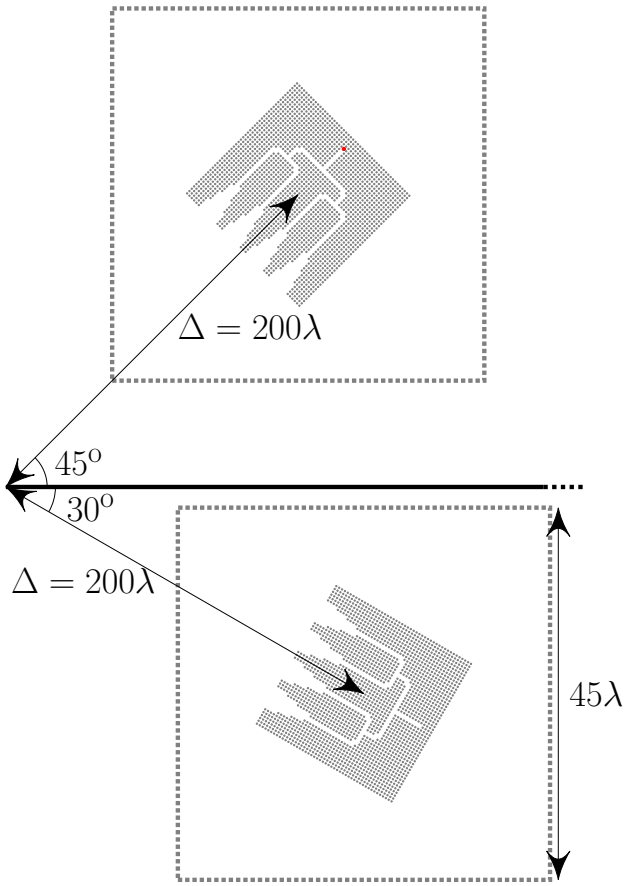

Figure 4.17: Geometry for the application example (scaled). The line-of-sight between the arrays is obstructed by a semi-infinite PEC plate, whose presence is taken into account by UTD. The gray squares around the two antenna arrays show the boundary within which the fields are plotted in Fig. 4.18.

The total computation time was 35 minutes and the required memory was about 500 MB. The amplitude of the field in the vicinity of the two arrays is shown in Fig. 4.18. In the shadow, the transmitted field still reaches the receiver via diffraction. The field penetrates the feed network through the separate horns and propagates further into the structure. The contributions of the four horns are clearly combined at the back end of the network. The reader notices that these fine details can easily be captured by the MLFMM-accelerated BIE-MoM part of our advocated hybrid scheme.

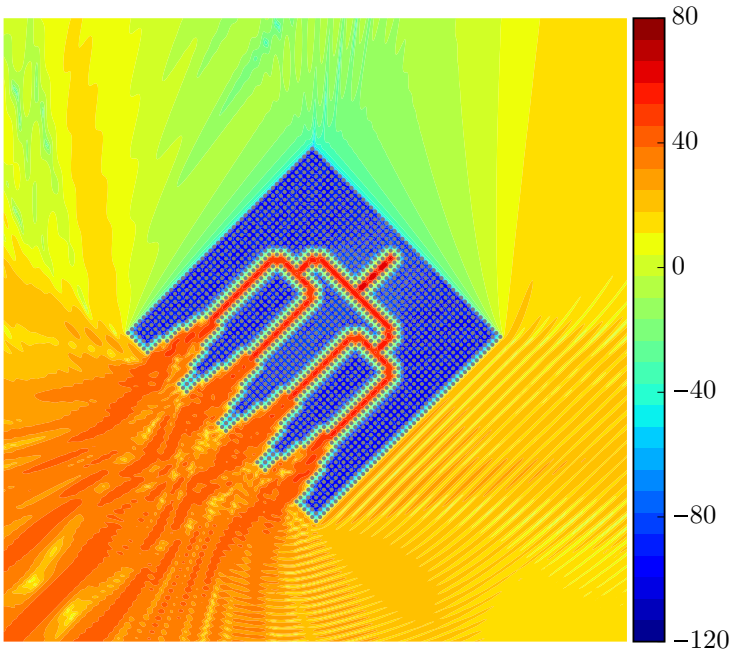

(a) Transmitting array

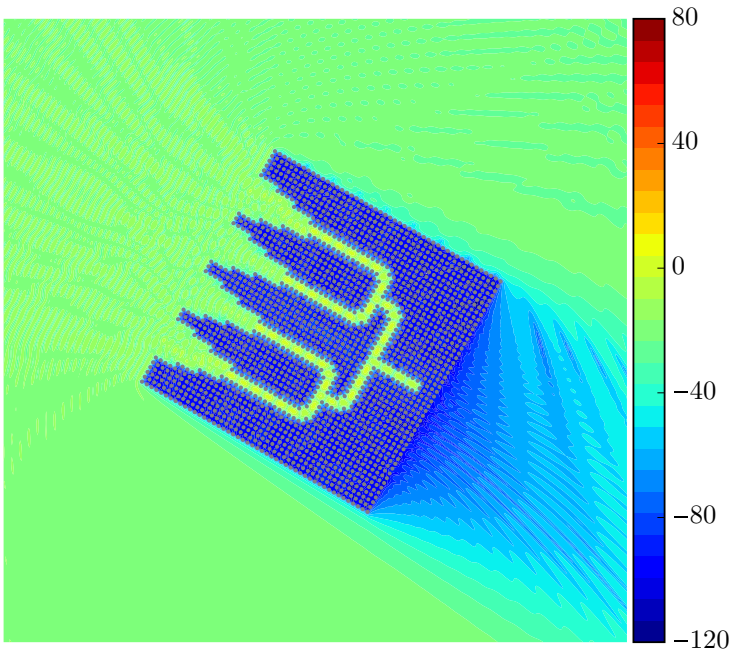

(b) Receiving array

Figure 4.18: Amplitude of the electric field (in dB V/m) in the vicinity of the horn antenna arrays.

4.4 Conclusion

A novel MLFMM-UTD hybrid method has been presented to analyze 2-D scattering in the presence of very large PEC scatterers. Reflections off the surface of the scatterers are taken into account using image theory, as such allowing to maintain the traditional MLFMM accuracy and efficiency via an FFT-based rotation of the pertinent radiation patterns. A new MLFMM compatible formalism has been introduced to account for diffractions at sharp edges, by generalizing the use of UTD for arbitrary source configurations. The accuracy has been tested and the results correspond well to these of traditional ray-optical hybrid schemes such as MoM-UTD and these of full-wave solvers, while the algorithm is much faster and requires a smaller amount of memory. Our novel scheme is accurate for NLoS problems whilst we also preserve the $\mathcal{O}(n)$ complexity. An application example consisting of electrically large antenna arrays has been simulated to demonstrate the capability of the method. The proposed method is especially suited to model large NLoS scattering problems. Future work comprises the extension to 3-D problems. Several issues need to be addressed, such as the rotation of the 3-D radiation pattern when dealing with reflections and the derivation of a new Huyghens' expansion to tackle diffraction. Moreover, a scalable version of the code over multiple processes can be implemented to allow the simulation of larger structures with hundreds of millions and even billions of unknowns [26].

References

[1] G. Karagounis, D. De Zutter, and D. Vande Ginste, "A Hybrid MLFMM-UTD Method for the Solution of Very Large 2-D Electromagnetic Problems", *IEEE Trans. Antennas Propagat.*, vol. 64, no. 1, pp. 224–234, 2016.

[2] G. Karagounis, D. De Zutter, and D. Vande Ginste, "An Efficient 2-D MLFMM-UTD Hybrid Method to Model Non-Line-of-Sight Propagation", in *International Conference on Electromagnetics in Advanced Applications (ICEAA) in Turin, Italy*, 2015, pp. 82–85.

[3] W. C. Chew, J.-M. Jin, E. Michielssen, and J. Song, *Fast and Efficient Algorithms in Computational Electromagnetics*. Artech House Publishers, 2001.

[4] G. A. Thiele and T. H. Newhouse, "A Hybrid Technique for Combining Moment Methods with the Geometrical Theory of Diffraction", *IEEE Trans. Antennas Propagat.*, vol. 23, no. 1, pp. 62–69, 1975.

[5] O. A. Civi, P. H. Pathak, H. T. Chou, and P. Nepa, "A Hybrid Uniform Geometrical Theory of Diffraction-Moment Method for Efficient Analysis of Electromagnetic Radiation/Scattering from Large Finite Planar Arrays", *Radio Science*, vol. 35, no. 2, pp. 607–620, 2000.

[6] H. F. Harms, "Using Wire Grid Structures in the Combination of Uniform Geometric Theory of Diffraction and Method of Moments for Near-Field Analysis", *Radio Science*, vol. 35, no. 2, pp. 639–652, 2000.

[7] C. J. Reddy, M. D. Deshpande, C. R. Cockrell, and F. B. Beck, "Radiation Characteristics of Cavity Backed Aperture Antennas in Finite Ground Plane Using the Hybrid FEM/MoM Technique and Geometrical Theory of Diffraction", *IEEE Trans. Antennas Propagat.*, vol. 44, no. 10, pp. 1327–1333, 1996.

[8] J. Silvestro, "Scattering from Slot Near Conducting Wedge Using Hybrid Method of Moments Geometrical-Theory of Diffraction – TE Case", *Electronics Letters*, vol. 28, no. 11, pp. 1055–1057, 1992.

[9] I. P. Theron, D. B. Davidson, and U. Jakobus, "Extensions to the Hybrid Method of Moments/Uniform GTD Formulation for Sources Located Close to a Smooth Convex Surface", *IEEE Trans. Antennas Propagat.*, vol. 48, no. 6, pp. 940–945, 2000.

[10] X. C. Wei and E. P. Li, "Efficient EMC Simulation of Enclosures with Apertures Residing in an Electrically Large Platform Using the MM-UTD Method", *IEEE Trans. Electromagn. Compat.*, vol. 47, no. 4, pp. 717–722, 2005.

[11] W. D. Burnside, C. L. Yu, and R. J. Marhefka, "Technique to Combine the Geometrical Theory of Diffraction and Moment Method", *IEEE Trans. Antennas Propagat.*, vol. 23, no. 4, pp. 551–558, 1975.

[12] H. J. Bilow, "Scattering by an Infinite Wedge with Tensor Impedance Boundary Conditions – a Moment Method/Physical Optics Solution for the Currents", *IEEE Trans. Antennas Propagat.*, vol. 39, no. 6, pp. 767–773, 1991.

[13] Z. Q. Gong, B. X. Xiao, G. Q. Zhu, and H. Y. Ke, "Improvements to the Hybrid MoM-PO Technique for Scattering of Plane Wave by an Infinite Wedge", *IEEE Trans. Antennas Propagat.*, vol. 54, no. 1, pp. 251–255, 2006.

[14] E. Jørgensen, S. Maci, and A. Toccafondi, "Fringe Integral Equation Method for a Truncated Grounded Dielectric Slab", *IEEE Trans. Antennas Propagat.*, vol. 49, no. 8, pp. 1210–1217, 2001.

[15] G. Apaydin, F. Hacivelioglu, L. Sevgi, and P. Ufimtsev, "Wedge Diffracted Waves Excited by a Line Source: Method of Moments (MoM) Modeling of Fringe Waves", *IEEE Trans. Antennas Propagat.*, vol. 62, no. 8, pp. 4368–4371, 2014.

[16] A. Tzoulis and T. F. Eibert, "A Hybrid FEBI-MLFMM-UTD Method for Numerical Solutions of Electromagnetic Problems Including Arbitrarily Shaped and Electrically Large Objects", *IEEE Trans. Antennas Propagat.*, vol. 53, no. 10, pp. 3358–3366, 2005.

[17] D. Vande Ginste, E. Michielssen, F. Olyslager, and D. De Zutter, "A High-Performance Upgrade of the Perfectly Matched Layer Multilevel Fast Multipole Algorithm for Large Planar Microwave Structures", *IEEE Trans. Antennas Propagat.*, vol. 57, no. 6, pp. 1728–1739, 2009.

[18] R. G. Kouyoumjian and P. H. Pathak, "A Uniform Geometrical Theory of Diffraction for an Edge in a Perfectly Conducting Surface", *Proc. IEEE*, vol. 62, no. 11, pp. 1448–1461, 1974.

[19] D. Vande Ginste, "Perfectly Matched Layer Based Fast Multipole Methods for Planar Microwave Structures", PhD thesis, UGent, 2005.

[20] D. Vande Ginste, L. Knockaert, and D. De Zutter, "Error Control in the Perfectly Matched Layer Based Multilevel Fast Multipole Algorithm", *Journal of Computational Physics*, vol. 228, no. 13, pp. 4811–4822, 2009.

[21] *NIST Digital Library of Mathematical Functions*, http://dlmf.nist.gov/, Release 1.0.5 of 2012-10-01. [Online]. Available: `http://dlmf.nist.gov/`.

[22] R. J. Burkholder and D. H. Kwon, "High-Frequency Asymptotic Acceleration of the Fast Multipole Method", *Radio Science*, vol. 31, no. 5, pp. 1199–1206, 1996.

[23] I. Bogaert, D. Pissoort, and F. Olyslager, "A Normalized Plane-Wave Method for 2D Helmholtz Problems", *Microwave and Optical Technology Letters*, vol. 48, no. 2, pp. 237–243, 2006.

[24] R. Tiberio, G. Manara, G. Pelosi, and R. G. Kouyuoumjian, "High-Frequency Electromagnetic Scattering of Plane Waves from Double Wedges", *IEEE Trans. Antennas Propagat.*, vol. 37, pp. 1172–1180, 1989.

[25] D. Pissoort, E. Michielssen, D. Vande Ginste, and F. Olyslager, "A Rank-Revealing Preconditioner for the Fast Integral-Equation-Based Characterization of Electromagnetic Crystal Devices", *Microwave and Optical Technology Letters*, vol. 48, pp. 783–789, 4 2006.

[26] B. Michiels, J. Fostier, I. Bogaert, and D. De Zutter, "Full-Wave Simulations of Electromagnetic Scattering Problems With Billions of Unknowns", *IEEE Trans. Antennas Propagat.*, vol. 63, no. 2, pp. 796–799, 2015.

5

Elimination of Extraneous Diffraction Centers in the Method of Moments by the Use of PML Absorbing Boundary Conditions

G. Karagounis, D. De Zutter and D. Vande Ginste

This chapter is based on articles submitted to
Journal of Lightwave Technology [1] and
IEEE Antennas and Wireless Propagation Letters [2].

★ ★ ★

In this chapter, the coordinate stretching formulation of a perfectly matched layer is integrated into a method of moments based boundary integral equation solver in order to damp the interaction between multiple edges of the same structure. This allows focusing on the scattering by an individual part of the structure, e.g. on an individual diffraction center, as is often done in ray optics. By truncation of the simulation domain to a mere ten wavelengths from the scattering center, the advocated method is found to be both efficient and accurate compared to traditional and analytical solution techniques. The method is also used to investigate the coupling of beams in a polarization beam splitter consisting of optical slab waveguides.

5.1 Introduction

GTD and UTD have found widespread use in the investigation of EM scattering at complex targets [3]. The basic reasoning of these methods is to first seek scattering solutions, called *canonical solutions*, at simple geometries, called *canonical structures*. An example of such a canonical structure, that has been extensively investigated in the past [4]–[8], is a wedge formed by two intersecting faces. The canonical solutions can then be combined to obtain an approximation of the scattering at a complex structure.
One approach to obtain solutions for these canonical problems is to simplify the problem under consideration, e.g. by infinitely extending the faces that constitute the wedge, such that it can be solved analytically. UTD originally provided a high-frequency asymptotic solution for the diffraction at the tip of a PEC wedge with infinitely extended faces [4]. Since then, solutions for many other canonical problems have been found, such as the diffraction at a pair of PEC wedges [9] and the diffraction at a vertex formed by curved PEC wedges [10]. Unfortunately, the number of canonical structures that can be treated analytically remains limited.
Therefore, numerical simulation tools have been developed that can deal with more intricate geometries and materials. The main challenge when using numerical tools is dealing with the unavoidable truncation of the canonical structure. When truncating the faces of a wedge, for example, new, extraneous diffraction centers are introduced that make it hard to isolate the EM behavior of the tip under study from the total scattering pattern. One of the earliest approaches focused on the solution of scattering at a finite structure by the MoM, after which the current at extraneous scattering centers was truncated by a windowing function and the desired fields were calculated with the windowed currents [5]. This method allows dealing with much more intricate canonical examples, with minimal computational requirements. However, the extraneous scattering centers of the finite structure still indirectly influence the results, as their presence is taken into account in the MoM interaction matrix. Another study investigated the use of the MoM currents to obtain the scattered fields without windowing, but by truncating at such a distance from the scattering edge under study that the effect of the extraneous scattering centers becomes negligible [6]. Although possible, the simulated structure needs to be hundreds of wavelengths long to minimize the influence of the extraneous centers. Moreover, in Sec. 5.3.4 we will argue that this method is not always applicable. In [11], the Finite Difference Time Domain (FDTD) method has been utilized to model the scattering at a straight wedge. In that contribution, a perfectly matched layer (PML) is used to effectively isolate the effect of a single scattering center. A disadvantage of this time domain approach is that a canonical solution is only obtained after a FFT of a time sequence of the field values. This procedure needs to be repeated for every point for which the solution is desired.
In this paper, we integrate the stretching formulation of a PML in a novel way,

as used in Finite Element Methods (FEM) [12], into an MoM based BIE solver. The PML layer is used to remove the influence of extraneous diffraction centers by damping the interaction between them and the scattering center of interest. In Sec. 5.2 we introduce the stretching formalism of PMLs, the system of BIEs that is solved and we explain how the stretching formalism is implemented in a MoM solver. In Sec. 5.3, first, the PML parameters are optimized. Second, the efficiency and accuracy of the proposed method is illustrated by two examples. Third, we demonstrate the appositeness of the method for diffraction problems by investigating the complex canonical problem of plane-wave illumination of a thick PEC plate. Fourth, we investigate the coupling of beams in a polarization beam splitter, to demonstrate that the added value of the proposed method extends beyond the numerical treatment of UTD diffraction problems. In Sec. 5.4, we provide some concluding remarks.

5.2 Formalism

5.2.1 BIE-MoM

Consider the configuration of Fig. 5.1, consisting of n PEC and/or (nested) dielectric cylinders with material parameters ϵ_i, μ_i $(i = 1, \ldots, n)$. The pertinent transverse magnetic (TM_z) BIEs for a single dielectric object then are [13]

$$\begin{aligned} e_z^i - \lim_{\boldsymbol{r}\to C^+} \oint_C \mathrm{d}c' \left[e_z \frac{\partial G_0}{\partial n'} - \frac{jk_0^2}{\omega\epsilon_0} G_0 h_t \right] \\ = \lim_{\boldsymbol{r}\to C^-} \oint_C \mathrm{d}c' \left[e_z \frac{\partial G}{\partial n'} - \frac{jk_i^2}{\omega\epsilon_i} G h_t \right], \end{aligned} \tag{5.1}$$

$$\begin{aligned} h_t^i - \lim_{\boldsymbol{r}\to C^+} \oint_C \mathrm{d}c' \left[-\frac{j\omega\epsilon_0}{k_0^2} e_z \frac{\partial G_0}{\partial n \partial n'} - \frac{\partial G_0}{\partial n} h_t \right] \\ = \lim_{\boldsymbol{r}\to C^-} \oint_C \mathrm{d}c' \left[-\frac{j\omega\epsilon_i}{k_i^2} e_z \frac{\partial G}{\partial n \partial n'} - \frac{\partial G}{\partial n} h_t \right], \end{aligned} \tag{5.2}$$

where e_z^i and h_t^i are the incoming tangential electric and magnetic fields on the boundary of the cylinder, respectively.

The BIEs are solved for e_z and h_t, the unknown total tangential electric and magnetic fields on the boundary, respectively. ϵ and μ are the material parameters of the object, $k_i^2 = \omega^2 \epsilon_i \mu_i$, and the Green's function for a source at $\boldsymbol{r}' = x'\hat{\boldsymbol{x}} + y'\hat{\boldsymbol{y}}$ and an observation point at $\boldsymbol{r} = x\hat{\boldsymbol{x}} + y\hat{\boldsymbol{y}}$ is given by

$$G(\boldsymbol{r}; \boldsymbol{r}') = \frac{j}{4} H_0^{(2)} \left(k_i \, d(\boldsymbol{r}, \boldsymbol{r}') \right), \tag{5.3}$$

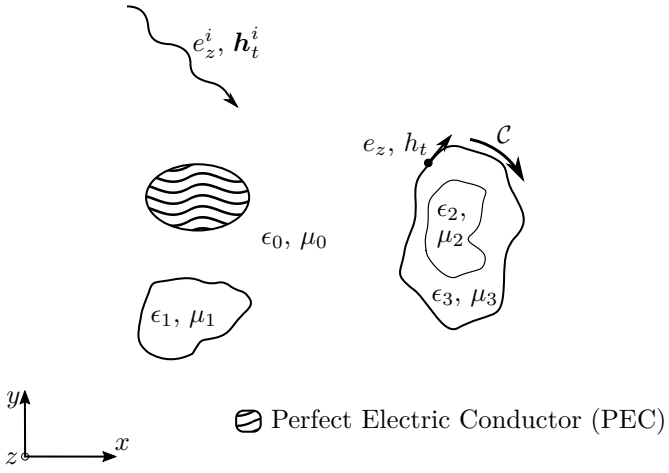

Figure 5.1: Objects illuminated by an electromagnetic wave.

and similarly for k_0 and G_0. $d(\boldsymbol{r}, \boldsymbol{r}')$ is the distance between the source and observation points, i.e. $\sqrt{(x-x')^2+(y-y')^2}$. The contour C denotes the boundary of the dielectric object, C^- and C^+ being its interior and exterior boundary, respectively.
At the surface of a PEC body, only (5.1) and the unknown h_t at C^+ remain. So, e_z and the entire right-hand side of the equation should be replaced by zero. Similar expressions exist for the transverse electric (TE_z) problem [13].
To solve the BIEs (5.1) and (5.2) with the well-known Galerkin MoM, pulse basis functions are used to expand h_t along the contour C and as test functions for (5.1). Hat functions are used to expand e_z and as test functions for (5.2) [14].

5.2.2 The coordinate stretching formalism

In order to damp the influence of subparts of the objects, the PML coordinate stretching formalism is employed, in a similar way as in FEM [12]. Ideally, a PML layer *(a)* exponentially damps impinging fields and *(b)* does not introduce reflections at the free space/PML interface.
For simplicity, we focus on stretching in the x-direction. A coordinate transformation $x \to \tilde{x}$ is introduced as follows (see also Fig. 5.2 for an illustration):

$$\tilde{x} = x_r + jx_i = \int_0^x dx'\, \tilde{\chi}(x'), \tag{5.4}$$

with $\tilde{\chi}(x)$ a complex function of x. x_r and x_i denote the real and imaginary part of $\tilde{x}$, respectively. This is equivalent to the introduction of a new medium. In

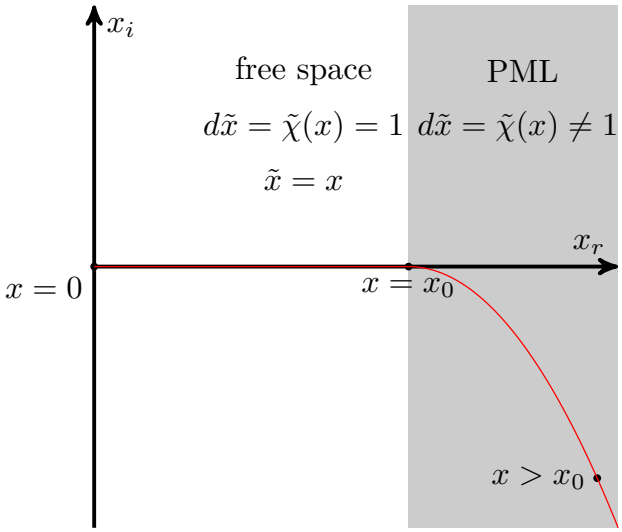

Figure 5.2: Illustration of the PML coordinate stretching formalism.

this new medium, the derivative in the x-direction is stretched in the following way:

$$\frac{\partial}{\partial x} \rightarrow \frac{\partial}{\partial \tilde{x}} = \frac{1}{\tilde{\chi}(x)} \frac{\partial}{\partial x}. \tag{5.5}$$

It can be shown [12], [15] that by introducing these changes into Maxwell's equations, the characteristic impedance of the new medium remains unchanged w.r.t. to the background medium, irrespective of $\tilde{\chi}(x)$. Moreover, the wave equation

$$\left(\frac{\partial^2}{\partial \tilde{x}^2} + k_x^2 \right) \tilde{\phi}(x) = 0, \tag{5.6}$$

is satisfied by

$$\tilde{\phi}(x) = A \exp\left(-jk_x\tilde{x}\right) + B \exp\left(jk_x\tilde{x}\right), \tag{5.7}$$

which further indicates that no reflections occur at the interface between free space and the new medium, irrespective of frequency or angle of incidence, if $\tilde{x}$ is a continuous function of x.
Assuming that the interface between the free-space background medium and the new medium is situated at $x = x_0$, as shown in Fig. 5.2, $\tilde{x}$ becomes

$$\tilde{x} = \begin{cases} x, & x \leq x_0 \\ x_r + jx_i \ (x_i \neq 0), & x > x_0 \end{cases} \tag{5.8}$$

Introducing (5.8) into the plane wave solution propagating to the right in (5.7) leads to

$$A \exp\left(-jk_x x_r\right) \exp\left(k_x x_i\right), \tag{5.9}$$

such that the wave is exponentially damped if x_i is negative for $x > x_0$. Thus, the new medium acts as a PML.

5.2.3 PML layers in the BIE-MoM

After discretization of the scatterers in MoM, the begin- and endpoints of each segment are transformed according to the stretching formalism of Sec. 5.2.2. A reinterpretation of geometrical quantities such as segment length, tangent vector, etc. imposes itself. First, the distance function appearing in (5.3) has to be adjusted. For complex vectors $\tilde{\boldsymbol{r}}$ and $\tilde{\boldsymbol{r}}'$, the "distance" function becomes

$$\begin{aligned} d(\tilde{\boldsymbol{r}}, \tilde{\boldsymbol{r}}') &= \sqrt{(\tilde{x} - \tilde{x}')^2 + (y - y')^2} \\ &= \big[(x_r - x_r')^2 - (x_i - x_i')^2 + (y - y')^2 \\ &\quad + 2j(x_r - x_r')(x_i - x_i')\big]^{1/2}. \end{aligned} \tag{5.10}$$

Note that, by the conventional definition of the square root function for complex arguments, the sign of the imaginary part of $d(\tilde{\boldsymbol{r}}, \tilde{\boldsymbol{r}}')$ and the sign of the imaginary part inside the square brackets of the right-hand side of (5.10) are the same. Thus, to obtain a negative imaginary part for $d(\tilde{\boldsymbol{r}}, \tilde{\boldsymbol{r}}')$, which is required given (5.9), x_i must be monotonically decreasing and x_r is logically chosen to be monotonically increasing in function of x. Naturally, the proposed square root function does not represent a distance measure, as it is complex-valued. With a slight abuse of terminology, we will continue to use the term "distance function", as has been done previously elsewhere [16].
The concept of tangential and normal vectors must also be generalized to complex coordinates. The concept of a line between two vectors $\tilde{\boldsymbol{p}}_0$ and $\tilde{\boldsymbol{p}}_1$ is now extended for complex vectors as the collection of complex vectors $\tilde{\boldsymbol{p}}$ fulfilling

$$\tilde{\boldsymbol{p}} = (1 - s)\tilde{\boldsymbol{p}}_0 + s\tilde{\boldsymbol{p}}_1 \equiv \tilde{\boldsymbol{p}}_0 + s\tilde{l}\,\tilde{\boldsymbol{t}}, \tag{5.11}$$

with $s \in [0, 1]$, $\tilde{l} = d(\tilde{\boldsymbol{p}}_0, \tilde{\boldsymbol{p}}_1)$ and $\tilde{\boldsymbol{t}} = 1/\tilde{l}\,(\tilde{\boldsymbol{p}}_1 - \tilde{\boldsymbol{p}}_0)$. $\tilde{\boldsymbol{t}}$ is the extension of the definition of a tangential vector along a line. The extension of the definition of

a vector $\tilde{\boldsymbol{n}}$ normal to $\tilde{\boldsymbol{t}}$ follows naturally: $\tilde{\boldsymbol{n}} = \pm(\hat{z} \times \tilde{\boldsymbol{t}})$.
Using (5.5), the normal derivatives appearing in (5.1) and (5.2) are now replaced in the following way:

$$\frac{\partial}{\partial n} = \boldsymbol{n} \cdot \nabla \to \tilde{\boldsymbol{n}} \cdot \left(\frac{1}{\tilde{\chi}(x)} \frac{\partial}{\partial x} \hat{x} + \frac{\partial}{\partial y} \hat{y} \right). \tag{5.12}$$

Lastly, in a classical Galerkin-MoM, pulse and hat functions are normalized such that the area below the function measures unity. Here, the normalization factors are adjusted by a formal integration over complex limits, leading to identical expressions as traditional results, where segment lengths are replaced by their complex counterparts.
Equipped with these changes to the MoM solver, a PML layer is easily integrated into already existing simulation software. The influence of the part of the scatterers that reside inside the PML will be damped, thus creating the possibility to efficiently focus on the scattering properties of only part of the structure.

5.2.4 Coordinate stretching functions

There are several types of stretching functions that fulfill the requirements posed by (5.9) and (5.10). We investigate three different types, based on previously published results [12], [17], [18]. Table 5.1 summarizes the $\tilde{\chi}(x)$ function and the resulting stretched $\tilde{x}$ for each type inside the PML layer ($x > x_0$). For $x \leq x_0$, no stretching is applied ($\tilde{\chi}(x) = 1$ and $\tilde{x} = x$).

Table 5.1: The three different types of coordinate stretching used in this work for $x > x_0$. Here, $\sigma(x) = \sigma_{max} \left(\frac{x-x_0}{D}\right)^m$.

	type I	type II	type III
$\tilde{\chi}(x)$	$1 - j\alpha$	$e^{-j\theta}$	$1 - j(1+m)\sigma(x)$
x_r	x	$x_0 + \cos\theta(x - x_0)$	x
x_i	$-\alpha(x - x_0)$	$-\sin\theta(x - x_0)$	$-\sigma(x)(x - x_0)$
	$\alpha > 0$	$\theta \in]0, \pi/2[$	$m \in \mathbb{N}$ $\sigma_{max} > 0$ $D > \sup(x - x_0)$

5.3 Results

5.3.1 Optimization of the PML parameters

For reasons of efficiency, the computational domain inside the PML is kept as small as possible. By making the attenuation parameters (type I: α, type II: θ,

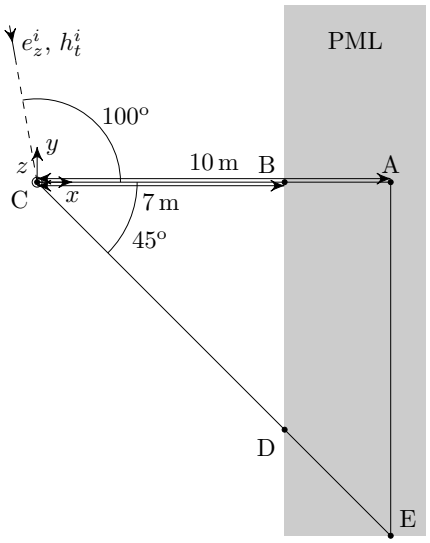

Figure 5.3: Geometry used for the optimization tests of the PML layer.

type III: σ_{max}) large, interactions inside the PML are damped faster. It is known, however, that discretization introduces reflections at the free space/PML interface. In [19], it is shown, for an FEM solver and employing a type I stretching, that a reflection at the free space/PML interface arises of magnitude proportional to $\alpha^2\Delta^2$, with Δ the discretization length. Consequently, the attenuation parameter cannot be chosen arbitrarily large. Some trade-off is required.

An optimization test for the attenuation parameters is performed using the geometry shown in Fig. 5.3. A PEC wedge of inner opening angle 45° is truncated at $x = 10\,\mathrm{m}$. A PML layer is added at $x = 7\,\mathrm{m}$ to damp the influence of the right side and the two right tips. A unit-amplitude, TM_z-polarized, plane wave with wavelength $\lambda = 1\,\mathrm{m}$, coming in at an angle of 100° with the x-axis, illuminates the wedge.

The dominant scattering mechanisms are the reflection at the upper face and the diffraction at the left tip of the wedge. As a reference, we employ the analytical solution for the scattering at an infinite PEC wedge with exterior opening angle $\nu\pi$ by a unit-amplitude, TM_z-polarized plane wave, coming in at angle ϕ_0 with the positive x-axis. The z-oriented current on the upper face of the wedge, at distance r from the tip, is given by [7]

$$j_z(r) = -\frac{4j}{\nu r\omega\mu}\sum_{l=1}^{\infty}\frac{l}{\nu}\exp\left(j\frac{l\pi}{2\nu}\right)J_{l/\nu}(kr)\sin\left(\frac{l}{\nu}\phi_0\right), \qquad (5.13)$$

and the currents at the lower side by

$$j_z(r) = -\frac{4j}{nr\omega\mu}\sum_{l=1}^{\infty}(-1)^{l+1}\frac{l}{\nu}\exp\left(j\frac{l\pi}{2\nu}\right)J_{l/\nu}(kr)\sin\left(\frac{l}{\nu}\phi_0\right). \tag{5.14}$$

We truncated this series at 200 terms.

Figs. 5.4(a)-5.4(c) show the current amplitude on the two faces of the wedge for each stretching type and for different values of the attenuation parameter. The abscissas correspond to the pertinent positions shown in Fig. 5.3. For all three stretching types, increasing the value of the attenuation parameter leads to better damping of the current density near the undesired tips A and E at $x = 10\,\mathrm{m}$. For high values of the attenuation parameter of stretching types I and III, a peak in the current density is observed on the segments just inside the PML layer, close to the interface B.
To assess the fitness of the different stretching formalisms, we investigate in more detail the trade-off between these two apparently counteracting demands, i.e. the damping of the PML versus the accuracy of the solution at the free space/PML interface. In Fig. 5.5, the current at the tip A, which is a measure for the damping of the PML layer, is plotted against the RE of the solution at B, just to the left of the free space/PML interface. Compared to the analytical reference result (5.13), this RE is defined as follows:

$$RE = \left|\frac{\text{solution} - \text{reference}}{\text{reference}}\right|. \tag{5.15}$$

The two competing demands plotted in Fig. 5.5 form Pareto fronts. Type I and type II stretching are both linear stretching formalisms, i.e. the imaginary part of the stretched coordinate increases linearly with increasing x. As such, they perform similarly over a certain range of their respective PML parameters. Damping by types I and II is negligible over the range of parameters that lead to an RE<10%. More damping can only be achieved at the cost of a worse RE. The nonlinear stretching of type III provides gradual damping, leading to the much better results, i.e. a high level of damping can be achieved while maintaining a low RE. Nonlinear stretching has been used extensively in the past due to its better trade-off of damping and accuracy [12], [18], [19].
In Fig. 5.6, the RE is shown for the z-component of the total electric field in the shadow zone of the wedge, obtained by using a type III stretching PML layer, with $m = 3$, $\sigma_{max} = 10$ and $D = 4$, when compared to the analytical solution [7]. These parameters correspond to the stretching that provides the best combination of high damping and low RE at the free space/PML interface in Fig. 5.5. In the shadow zone, where the only field contribution is due to the diffraction at the tip C under study, the RE remains below 3%, even very close to the diffracting tip and also near the free space/PML interface. In the other zones, the dominant contributions stem from the incident and/or reflected waves, leading to even better accuracy.

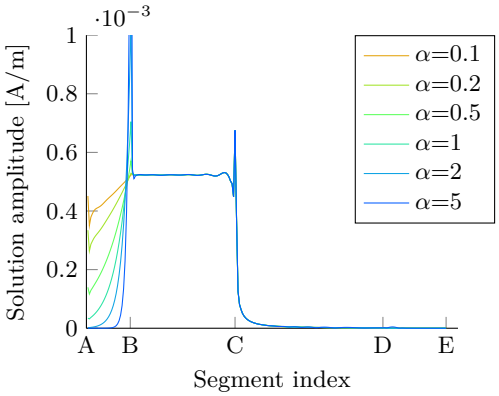

(a) Type I results

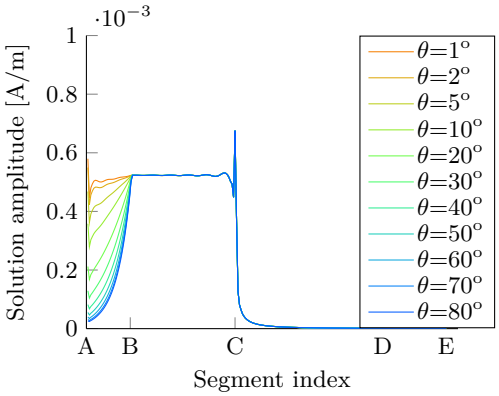

(b) Type II results

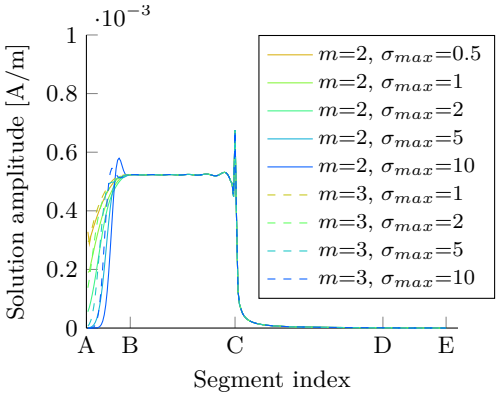

(c) Type III results

Figure 5.4: Results of the optimization tests. The points A-E correspond to the pertinent points in Fig. 5.3. For type III stretching, $D = 4$.

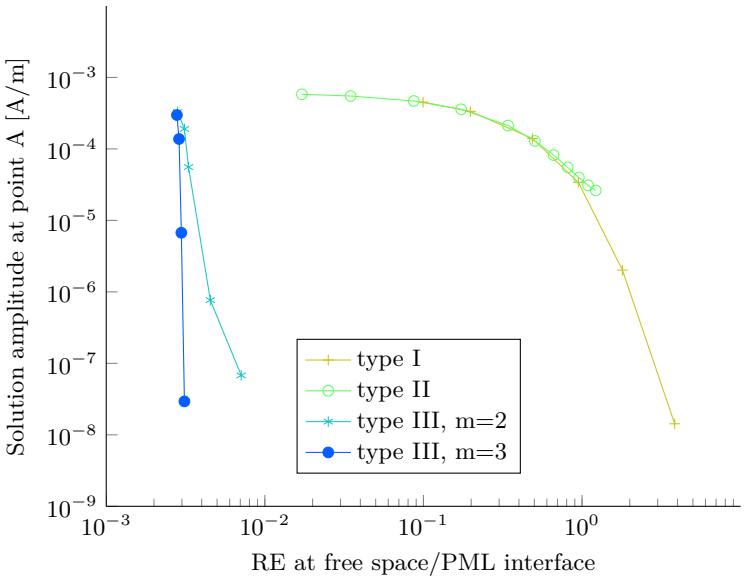

Figure 5.5: Pareto fronts for demands on accuracy and damping when adding a PML layer.

5.3.2 Dielectric wedge

A similar example as in Sec. 5.3.1, now with a lossy dielectric silicon wedge, is investigated next. The wedge has a relative dielectric permittivity $\epsilon_r = 11.9$. The wavelength λ is 1 m. For the PML layer, a type III stretching is used with $m = 3$, $D = 4\lambda$ and $\sigma_{max} = 10$. An asymptotic analytical solution for scattering at an infinitely extended dielectric wedge, called the Malyuzhinets solution, serves as reference [8]. Also a traditional MoM simulation in free space is performed. To this end, a wedge with inner opening angle 45° and ϵ_r =11.9 is truncated by closing the wedge with a vertical back-end at 100 m from the tip. The truncation length is chosen based on a previous publication in which traditional MoM solvers are used to investigate scattering at wedges [6]. For this large structure, the computation is accelerated with MLFMM. The same illumination as in Fig. 5.3 is used.
The computational resources used in the two simulations are summarized in Tab. 5.2. The large structure modeled by MLFMM is discretized with almost ten times more unknowns than the structure modeled with the novel MoM-PML technique. Despite the acceleration with MLFMM, for this example this results in the use of twice as much memory and a large increase in the solution time compared to the PML truncated MoM simulation.
The field values at 100 equidistant angles on a circle with radius 5 m around the tip are shown in Fig. 5.7. The vertical lines at observation angles 80° and 280°

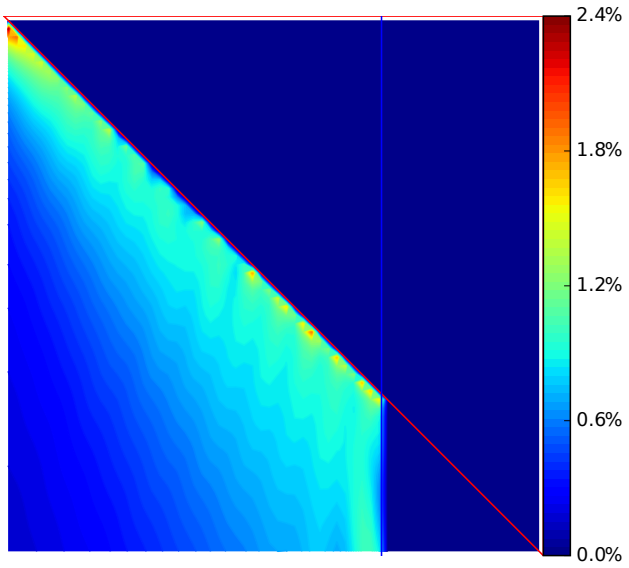

Figure 5.6: RE on the z-oriented electric field compared to the analytical solution.

are so-called *transition regions*. In these regions, the Malyuzhinets solution is not valid. Both methods produce similar results over the entire circular region and are comparable to the reference solution, except for the transition regions.

Table 5.2: Computational resources for the simulation of a dielectric wedge.

	MoM truncated by PML	MLFMM free space
unknowns	2356	23558
memory	85 MB	172 MB
iterations	45	1929
solution time	4 s	9 m 5 s

5.3.3 Diffraction of a plane wave at a thick PEC plate

This section illustrates the isolation of individual diffraction mechanisms by our method. We focus on the example of a thick PEC plate illuminated by a plane wave as shown in Fig. 5.8. Owing to the practical relevance of this canonical geometry, several contributions in the literature focused on the theoretical derivation of a diffraction coefficient for a semi-infinite thick PEC plate. Ideally, this diffraction coefficient describes the doubly diffracted rays originating from both diffraction tips. For the geometry in Fig. 5.8, in the case of TM illumination,

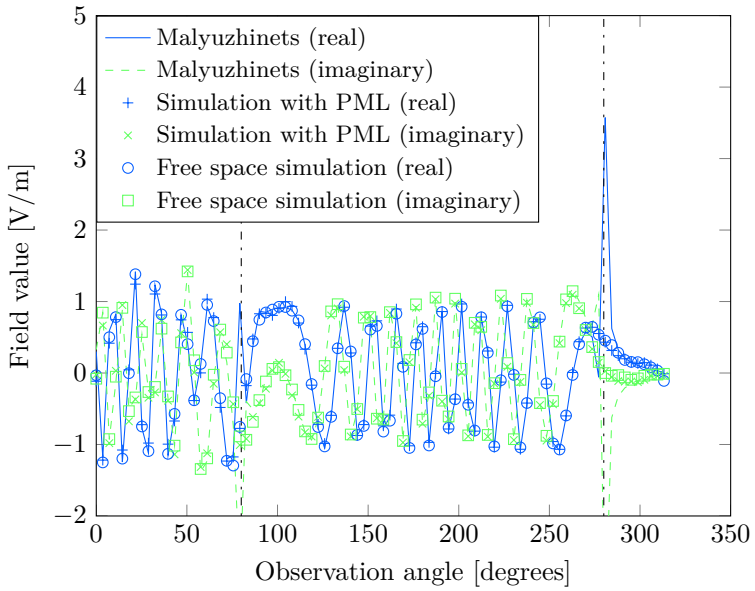

Figure 5.7: Field values for scattering at dielectric wedge. The dash-dotted lines indicate transition regions, in which the Maluyzhinets reference solution is not valid.

the singly diffracted field from the upper tip is zero along the left side of the slab. Thus, it is not possible to describe the entire diffraction using traditional UTD methods. For TE illumination, the diffracted field is non-zero and UTD can still be used [20], in a similar way as was done in Sec. 3.3.4. Therefore, we will only consider the more intricate case of TM illumination in this example.

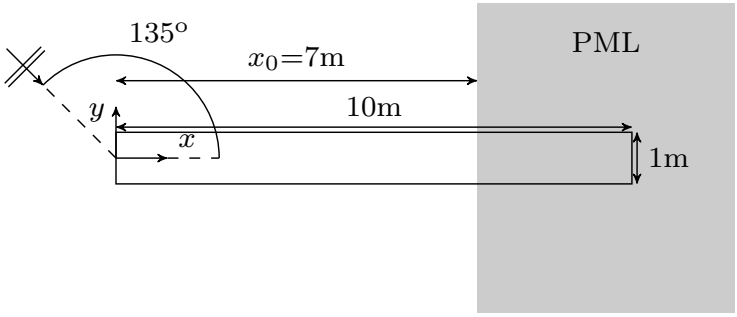

Figure 5.8: Plane wave excitation of a thick PEC plate.

In this TM case, a higher-order diffraction mechanism becomes relevant, called *slope diffraction*, which is related to the normal derivative of the incoming

field [21]–[24]. The theory of slope diffraction is only applicable when the PEC plate is sufficiently thick, such that the two diffracting tips are sufficiently far apart. More intricate techniques, that are also applicable when the plane wave is near grazing incidence with respect to the left side, are either based on STD [25], [26] or PTD [27]. More recently, an exact solution was derived by using conformal mapping [28].
We write the total field E_z^{tot} for the geometry shown in Fig. 5.8 ($\lambda = 1\,\mathrm{m}$) as follows:

$$E_z^{tot} = E_z^{inc} + E_z^{refl} + E_z^{UTD} + E_z^{rest}, \tag{5.16}$$

where E_z^{inc} is the incoming field (here a plane wave), E_z^{refl} is the field that is reflected by the left and upper side, E_z^{UTD} is the sum of the singly diffracted fields at both tips and the remaining part, including double diffractions, is given by E_z^{rest}. E_z^{refl} can be described by GO and E_z^{UTD} can be described by UTD for a PEC wedge. In Fig. 5.9(a), the amplitude of E_z^{tot} is shown as computed by our advocated MoM method. Figs. 5.9(b)-5.9(d) show the amplitude of the remaining field after consecutively subtracting E_z^{inc}, E_z^{refl} and E_z^{UTD} from E_z^{tot}. Fig. 5.9(d) may thus be regarded as the amplitude of the numerical approximation of E_z^{rest}. This result can be further used to derive a numerical diffraction coefficient for higher-order diffractions, which in turn can be leveraged in simulation software such as the MLFMM-UTD formalism presented in Chapter 4.

5.3.4 Dielectric slab

The following test concerns the coupling of a Gaussian beam into a silica glass slab waveguide. The geometry is shown in Fig. 5.10. A TM-polarized Gaussian beam with wavelength $5\,\mu$m and beam waist $4\,\mu$m at $x = -2.5\,\mu$m, propagating along the positive x-axis, excites a slab waveguide that starts at $x = 0$. At the wavelength of $5\,\mu$m, silica glass has a relative permittivity of $\epsilon_r = 11.9$ and a loss tangent of 0.0057 [29]. The waveguide is modeled twice: once without taking the losses into account and once as a lossy dielectric. The slab of width $4\,\mu$m is modeled by a rectangle of length $50\,\mu$m and a PML layer is added, starting at $x = 35\,\mu$m, to avoid reflections from the back-end. A type III stretching formalism is used with $m = 3$, $D = 20\,\mu$m and $\sigma_{max} = 10$. As a reference, the slab waveguide is modeled in free space by a rectangular slab of length $500\,\mu$m using an MLFMM accelerated solver.
The amplitude of the z-component of the electric field along the long symmetry axis of the waveguide is shown in Fig. 5.11. Note that in the lossless case and for the solution in free space, the sinusoidal behavior in the field amplitude is the result of reflections at the backend, leading to a standing wave pattern. This would still appear, even when a waveguide of a larger length is modeled. This erroneous behavior is avoided by the use of a PML layer. We highlight

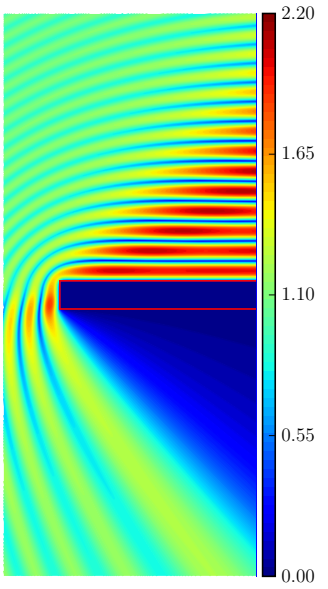

(a) total field $|E_z^{tot}|$

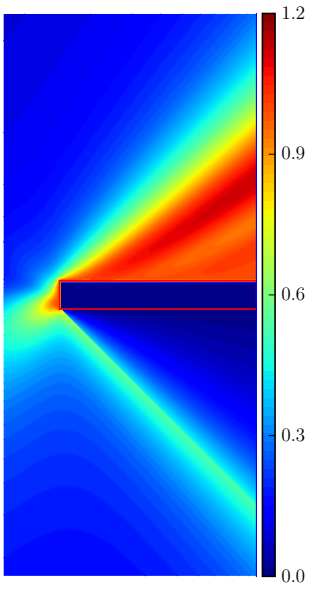

(b) scattered field $|E_z^{tot} - E_z^{inc}|$

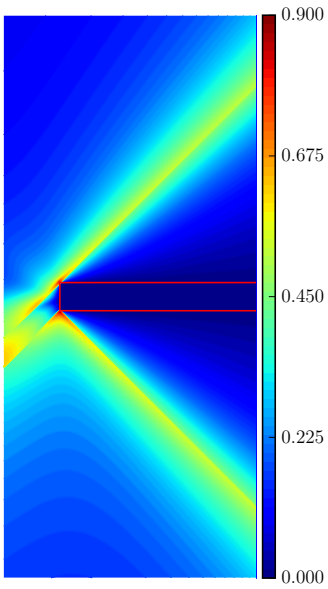

(c) diffracted field $|E_z^{tot} - E_z^{inc} - E_z^{refl}|$

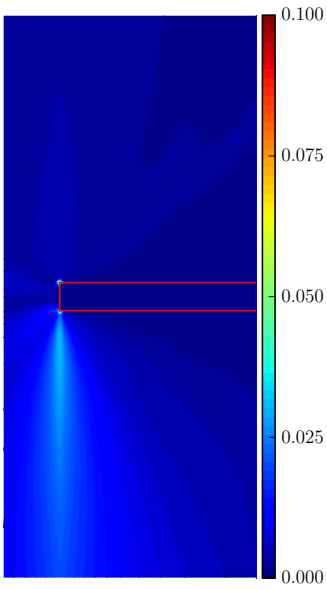

(d) higher-order diffraction $|E_z^{rest}|$

Figure 5.9: Amplitude of different field contributions (in V/m) for plane wave illumination of a PEC slab.

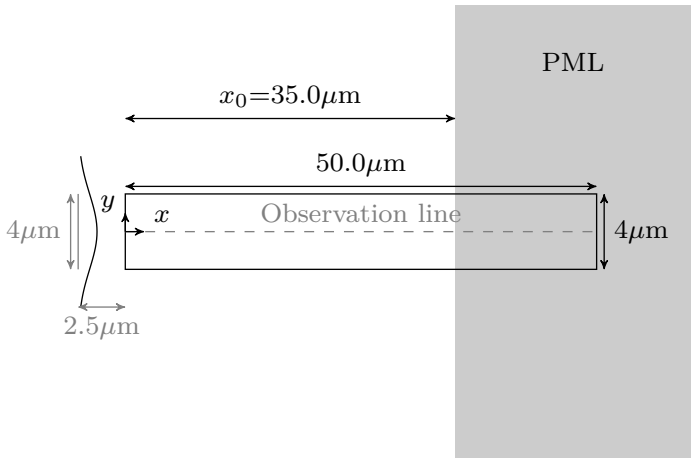

Figure 5.10: Excitation of a dielectric slab by a Gaussian beam.

this to show that a naive truncation at a large distance from the scattering center of interest does not always lead to a correct solution. Thus, the method described in [6] cannot be used to investigate scattering at a dielectric wedge.

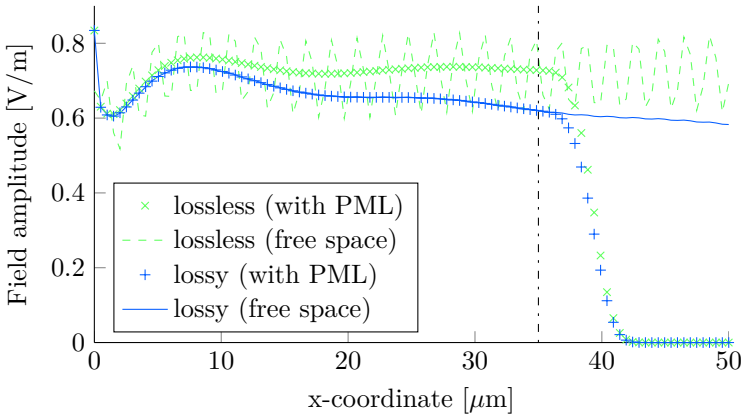

Figure 5.11: Fields along the axis of a dielectric slab. The PML interface is indicated by the vertical dash-dotted line.

5.3.5 Polarization beam splitter

As an application example, we investigate the silicon polarization beam splitter (PBS) schematically shown in Fig. 5.12. The design is based on a prototype consisting of silicon-on-insulator (SOI) nanowires reported elsewhere [30]. Sig-

nals of both TM_x and TE_x polarization are coupled in the PBS at wavelength $\lambda = 1550\,\text{nm}$ at the left boundary of the upper slab. Note that in this example TM and TE refer to the axis of beam propagation instead of the axis of invariance, in contrast to the previous sections, to conform with the convention most often used in waveguide theory. The widths w_1 (narrow upper and lower slabs) and w_2 (wide middle slab) are designed such that the phase matching between TM_x modes of the narrow slabs and the wider slab is optimally satisfied and this is not the case for TE_x modes. This allows to transfer TM_x polarized beams from the upper slab to the lower slab, while ensuring that TE_x polarized beams remain confined in the upper slab. The permittivity of the slabs in Fig. 5.12 is $\epsilon_r = 11.9$ and are surrounded by free space.

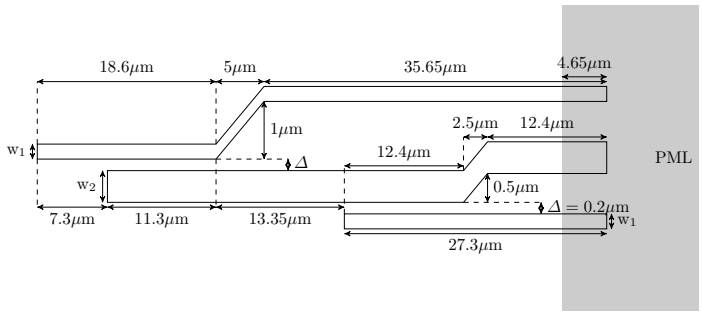

Figure 5.12: Polarization beam splitter with three silicon slabs.

Modeling the fields inside the PBS is not possible with MoM without damping the effect of the extraneous backends added when truncating the dielectric slabs, as back-reflections would occur independently of the truncation size. Therefore, the structure is terminated by a PML with the same parameters as in the previous example.

In order to choose an appropriate pair of slab widths w_1 and w_2, first the effective index n_{eff} of the propagating modes in a dielectric slab waveguide is computed in function of the slab's width. The result is shown in Fig. 5.13. Then, for a fixed w_1, w_2 ($>w_1$) is thus chosen that n_{eff} of the $TM_{x,1}$ mode in the wide slab corresponds to n_{eff} of the $TM_{x,0}$ mode of the narrow slab (lower horizontal line in Fig. 5.13). Moreover, for the same pair of widths, n_{eff} of the $TE_{x,0}$ mode of the narrow slab does not correspond to n_{eff} of any of the modes of the wide slab. Therefore, the PBS shown in Fig. 5.12 is expected to split the propagating $TE_{x,0}$ and $TM_{x,0}$ modes in the upper slab.

In Fig. 5.14, the fields are shown when the upper slab of the PBS is excited at its left side by a Gaussian beam with width equal to w_1. For TM excitation in Fig. 5.14(a), the coupling of the beam from the upper slab to the lower slab is clearly visible. For TE excitation, shown in Fig. 5.14(b), the beam remains confined in the upper slab.

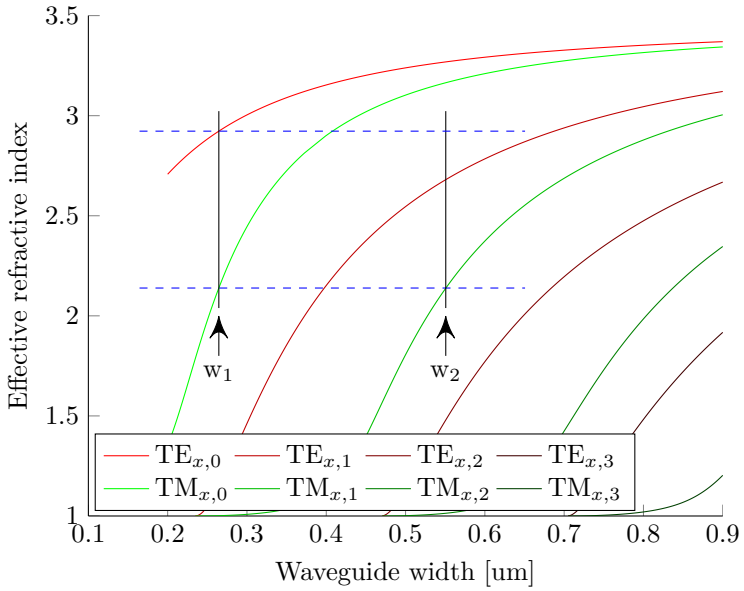

Figure 5.13: Effective indices of guided modes in a silicon slab waveguide.

5.4 Conclusion

We have integrated the coordinate stretching of PMLs, as used in FEM, into a MoM solver to damp the influence of extraneous scattering centers on a structure. This allows studying the scattering at isolated parts of a complex structure by BIE techniques. The necessary adjustments to already existing MoM solvers are minimal. The technique proves to be efficient. Even with a truncation at less than 10 wavelengths from the scattering center, a good accuracy compared to pertinent analytical solutions is achieved. Non-linear stretching provided the best results in terms of damping and accuracy of the solution close to the free space/PML interface. The method is verified for perfect conductors, dielectrics and lossy dielectrics.

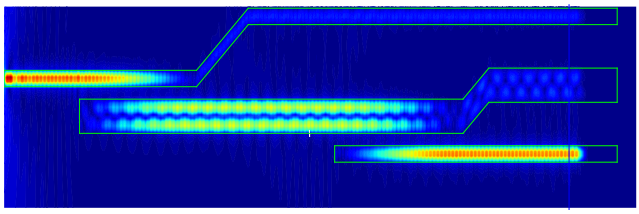

(a) TM_x excitation (H_z amplitude).

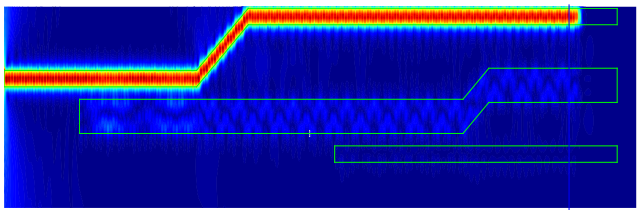

(b) TE_x excitation (E_z amplitude).

Figure 5.14: Field density in a polarization beam splitter with three optical waveguides.

References

[1] G. Karagounis, D. De Zutter, and D. Vande Ginste, "Full-wave Simulation of Optical Waveguides via Truncation in the Method of Moments Using PML Absorbing Boundary Conditions", *Optics Express*, submitted, 2016.

[2] G. Karagounis, D. De Zutter, and D. Vande Ginste, "Numerical Derivation of Diffraction Coefficients Using a Method of Moments with Incorporated Absorbing Boundaries", *IEEE Antennas Wireless Propag. Lett.*, submitted, 2016.

[3] P. H. Pathak, G. Carluccio, and M. Albani, "The Uniform Geometrical Theory of Diffraction and Some of Its Applications", *IEEE Antennas and Propagation Magazine*, vol. 55, no. 4, pp. 41–69, 2013.

[4] R. G. Kouyoumjian and P. H. Pathak, "A Uniform Geometrical Theory of Diffraction for an Edge in a Perfectly Conducting Surface", *Proc. IEEE*, vol. 62, no. 11, pp. 1448–1461, 1974.

[5] G. F. Herrmann, "Numerical Computation of Diffraction Coefficients", *IEEE Trans. Antennas Propagat.*, vol. 35, no. 1, pp. 53–61, 1987.

[6] G. Apaydin and L. Sevgi, "A Novel Wedge Diffraction Modeling Using Method of Moments (MoM)", *Applied Computational Electromagnetics Society Journal*, vol. 30, no. 10, pp. 1053–1058, 2015.

[7] P. Y. Ufimtsev, "Fast Convergent Integrals for Nonuniform Currents on Wedge Faces", *Electromagnetics*, vol. 18, no. 3, pp. 289–313, 1998.

[8] A. V. Osipov and A. N. Norris, "The Malyuzhinets Theory for Scattering from Wedge Boundaries: A Review", *Wave Motion*, vol. 29, no. 4, pp. 313–340, 1999.

[9] M. Albani, "A Uniform Double Diffraction Coefficient for a Pair of Wedges in Arbitrary Configuration", *IEEE Trans. Antennas Propagat.*, vol. 53, no. 2, pp. 702–710, 2005.

[10] M. Albani, G. Carluccio, and P. H. Pathak, "A Uniform Geometrical Theory of Diffraction for Vertices Formed by Truncated Curved Wedges", *IEEE Trans. Antennas Propagat.*, vol. 63, no. 7, pp. 3136–3143, 2015.

[11] J. H. Chang and A. Taflove, "Three-Dimensional Diffraction by Infinite Conducting and Dielectric Wedges Using a Generalized Total-Field/Scattered-Field FDTD Formulation", *IEEE Trans. Antennas Propagat.*, vol. 53, no. 4, pp. 1444–1454, 2005.

[12] W. C. Chew, J. M. Jin, and E. Michielssen, "Complex Coordinate Stretching as a Generalized Absorbing Boundary Condition", *Microwave and Optical Technology Letters*, vol. 15, no. 6, pp. 363–369, 1997, issn: 0895-2477.

[13] J. Fostier and F. Olyslager, "A GRID Computer Implementation of the Multilevel Fast Multipole Algorithm for Full-Wave Analysis of Optical Devices", *IEICE Transactions on Communications*, vol. E90B, no. 9, pp. 2430–2438, 2007, issn: 0916-8516.

[14] F. Olyslager, D. De Zutter, and K. Blomme, "Rigorous Analysis of the Propagation Characteristics of General Lossless and Lossy Multiconductor Transmission Lines in Multilayered Media", *IEEE Transactions on Microwave Theory and Techniques*, vol. 41, no. 1, pp. 79–88, 1993.

[15] L. Knockaert and D. De Zutter, "On the Stretching of Maxwell's Equations in General Orthogonal Coordinate Systems and the Perfectly Matched Layer", *Microwave and Optical Technology Letters*, vol. 24, no. 1, pp. 31–34, 2000.

[16] R. Torretti, *Philosophy of Geometry from Riemann to Poincaré*. Dordrecht, Holland: Springer Netherlands, 1978.

[17] D. Pissoort, D. Vande Ginste, and F. Olyslager, "Including PML-Based Absorbing Boundary Conditions in the MLFMA", *IEEE Antennas Wireless Propagat. Lett.*, vol. 4, pp. 312–315, 2005, issn: 1536-1225.

[18] S. D. Gedney, "An Anisotropic Perfectly Matched Layer-Absorbing Medium for the Truncation of FDTD Lattices", *IEEE Trans. Antennas Propagat.*, vol. 44, no. 12, pp. 1630–1639, 1996.

[19] F. Collino and P. B. Monk, "Optimizing the Perfectly Matched Layer", *Computer Methods in Applied Mechanics and Engineering*, vol. 164, no. 1-2, pp. 157–171, 1998, issn: 0045-7825.

[20] P. Mariage, P. Fiorot, and P. Degauque, "Improvement of the Uniform Theory of Diffraction Applied in a Conventionnal Manner to the Double Diffraction by Joined or Disjoined Wedges in Regions of Overlapping of the Transition Zones", *Annales Des Télécommunications*, vol. 53, pp. 406–417, 1998, issn: 1958-9395.

[21] R. Kouyoumjian, "The Geometrical Theory of Diffraction and Its Application", in *Numerical and Asymptotic Techniques in Electromagnetics*, R. Mittra, Ed., SpringerLink, 1975, ch. 6, pp. 165–215.

[22] R. J. Luebbers, "A Heuristic UTD Slope Diffraction Coefficient for Rough Lossy Wedges", *IEEE Trans. Antennas Propagat.*, vol. 37, pp. 206–211, 1989, issn: 0018-926X.

[23] M. B. Tabakcioglu and A. Kara, "Improvements on Slope Diffraction for Multiple Wedges", *Electromagnetics*, vol. 30, pp. 285–296, 2010, issn: 02726343.

[24] C. Balanis, *Advanced Engineering Electromagnetics*, Second edition. Wiley & Sons, Inc., 2012.

[25] L. Polka, C. Balanis, and A. Polycarpou, "High-Frequency Methods for Multiple Diffraction Modeling: Application and Comparison", *Journal of Electromagnetic Waves and Applications*, vol. 8, pp. 1223–1246, 1994.

[26] R. Tiberio, G. Manara, G. Pelosi, and R. G. Kouyuoumjian, "High-Frequency Electromagnetic Scattering of Plane Waves from Double Wedges", *IEEE Trans. Antennas Propagat.*, vol. 37, pp. 1172–1180, 1989.

[27] A. Michaeli, "A Closed Form Physical Theory of Diffraction Solution for Electromagnetic Scattering by Strips and 90° Dihedrals", *Radio Science*, vol. 19, pp. 609–616, 1984, issn: 1944-799X.

[28] M. V. Vesnik, "Use of the Generalized Eikonal in the Analytic Solution of the Problem of Electromagnetic-Wave Diffraction by a 2D Perfectly Conducting Half-plate", *Journal of Communications Technology and Electronics*, vol. 53, pp. 131–142, 2008, issn: 1555-6557.

[29] R. Kitamura, L. Pilon, and M. Jonasz, "Optical Constants of Silica Glass from Extreme Ultraviolet to Far Infrared at Near Room Temperature", *Applied Optics*, vol. 46, no. 33, pp. 8118–8133, 2007.

[30] D. Dai, "Silicon Polarization Beam Splitter Based on an Asymmetrical Evanescent Coupling System With Three Optical Waveguides", *Journal of Lightwave Technology*, vol. 30, no. 20, pp. 3281–3287, 2012, issn: 0733-8724.

6
Conclusions

Concluding remarks

In this work, we have investigated the combination of MLFMM with the high-frequency UTD method. The hybrid method is especially suitable for the numerical study of large scattering problems, where some parts of the simulation domain with fine geometrical details should be treated as accurately as possible. Currently, the well-established MoM-UTD hybrid method is commercially available to investigate such environments, but this method inherits the poor efficiency of its MoM part. Earlier approaches to combine MLFMM and UTD were based on the assumption that there is a very large distance between the MLFMM boxes and the UTD scatterer, limiting the applicability of the method. To our knowledge, in this work, we have presented for the first time a rigorous derivation of a UTD formulation that is fully compatible with MLFMM.

The hybridization of MLFMM and UTD has proven a challenging task. UTD canonical solutions are only available for a limited number of illumination sources, such as plane-waves, line sources and point sources and cannot be used to describe the scattering of radiation patterns in MLFMM. This necessitated the generalization of UTD for arbitrary sources, as described in Chapter 3. The novel method only requires samples of the source field on a contour surrounding the source and as such does not require any knowledge of the source's geometry. Efficiency is achieved by the extensive use of FFT. The proposed method increases the applicability range of UTD to all excitation types and canonical geometries for which UTD diffraction coefficients exist.

Starting from the generalization of UTD, a new full MLFMM translator for diffraction was introduced in Chapter 4. Despite the full translator, by allowing

MLFMM boxes on different levels in the MLFMM tree to interact with each other, it is shown, both theoretically and experimentally, that the complexity of the MLFMM remains unaffected for densely filled volumetric scatterers, i.e. the complexity scales as $\mathcal{O}(N)$, N being the number of discretized elements. Reflections at straight PEC surfaces were treated by a MLFMM formulation that leverages image source theory, thus ensuring that reflections are taken exactly into account with the same computational complexity as traditional MLFMM. Several numerical experiments have shown a very good correspondence between results of the novel MLFMM-UTD and MoM-UTD, even in shadow regions. It is also shown that another MLFMM-UTD approach, presented in literature, is in fact an asymptotic approximation of the scheme advocated in this work.

The newly developed hybrid solver, but also all other solvers that employ UTD, rely on the availability of canonical solutions in terms of diffraction coefficients. Unfortunately, UTD solutions only exist for a handful of canonical geometries. Therefore, in Chapter 5, we have introduced a method to derive numerical solutions for more intricate geometries (e.g., a semi-infinite PEC slab with finite thickness, which can serve as a model for a reflective wall). To model canonical structures, which are often assumed to be semi-infinite, with the MoM we have truncated the simulation domain with a PML, leveraging a complex coordinate stretching formalism as is often used in FEM. Only minimal changes to already existing MoM software are necessary. Good correspondence with analytic results for a PEC wedge were obtained by truncating the wedge at merely ten wavelengths from the diffraction tip, yielding a very efficient technique. The practical interest of a MoM solver supplemented with a PML layer extends beyond the numerical modeling of canonical UTD solutions. The appositeness of the technique was further demonstrated by applying it to the simulation of optical waveguides.

Future research

As EM modeling has to deal with simulation domains of ever increasing size, investigation and development of high-frequency simulation tools will remain important. In particular, when parts of the large domain, such as antennas, need to be treated very accurately, hybrid methods, such as the one presented in this work, become indispensable. Despite the presented advance in the development of an accurate MLFMM-UTD hybrid solver, several improvements are the subject of further research.

First, in some cases, it is necessary to include higher-order scattering effects, such as, e.g., a diffraction followed by a reflection or double diffractions. The current theoretical framework of the novel, hybrid MLFMM-UTD is not able to deal yet with these higher-order effects, except for the limited number of

cases for which a UTD canonical solution exists, e.g. for double diffraction at two connected PEC wedges. The treatment of higher-order scattering may be necessary before the proposed algorithm can be used in commercial software.

Second, although efficient for compact scatterers, the proposed method exhibits the same computational complexity as MoM-UTD for sparse scatterers. In Chapter 4, we already proposed a solution by approximating the elements of the full translation matrix by means of an asymptotic series expansion. It was argued that this expansion leads to the desired $\mathcal{O}(N \log N)$ complexity at loss of accuracy. Another possibility that was investigated briefly, is the use of the Complex Source Beam (CSB)-MoM method described in [1]. With this method, the interactions between well-separated groups are treated in a manner similar to FMM, but the radiation patterns of the groups are described by highly directive CSBs. The directive property of CSBs is expected to lead to a sparse MLFMM-UTD translator.

Third, an extension to 3-D imposes itself. The first two steps of the formalism described in Chapter 4, i.e. *(i)* introduction of equivalent sources around the source box and a multipole expansion for the source field and *(ii)* identification of the harmonics expansion coefficients for the equivalent source distribution with the expansion coefficients of the source field, can be repeated in 3-D after introduction of Debye potentials. The efficiency of the 2-D scheme presented in this work heavily depends on the Fourier decomposition of the equivalent sources on the circular contour around the source and observation regions. It remains a subject of study whether a decomposition in spherical harmonics, the equivalent of a Fourier decomposition in 3-D, can be performed without jeopardizing the computational complexity.

References

[1] K. Tap, P. H. Pathak, and R. J. Burkholder, "Complex Source Beam-Moment Method Procedure for Accelerating Numerical Integral Equation Solutions of Radiation and Scattering Problems", *IEEE Trans. Antennas Propagat.*, vol. 62, no. 4, pp. 2052–2062, 2014.

A

Derivation of UTD diffraction coefficients

A.1 Asymptotic integrals

Asymptotic integral analysis is of primary importance to the derivation of uniform diffraction coefficients. A short overview of asymptotic integral analysis is presented here. For detailed information, the reader is referred to [1], [2].

A.1.1 Watson's lemma

Consider an integral, depending on a real-valued positive parameter κ, of the form

$$I(\kappa) = \int_0^T \mathrm{d}t \, \exp(-\kappa t) t^\sigma g(t), \tag{A.1}$$

where $T > 0$, $\sigma > -1$ and $g(t)$ is infinitely differentiable in the neighborhood of $t = 0$. For large κ, the integrand quickly decreases. An asymptotic expression for the integral for $\kappa \to \infty$ is obtained by changing the upper integration limit to $+\infty$ and expanding $g(t)$ in a Taylor series around $t = 0$, also called a McLaurin series. The result is:

$$I(\kappa) \sim \sum_{n=0}^{\infty} \frac{g^{(n)}(0)}{n!} \int_0^{\infty} \mathrm{d}t \, \exp(-\kappa t) t^{\sigma+n} \sim \sum_{n=0}^{\infty} \frac{g^{(n)}(0)}{n!} \frac{\Gamma(\sigma+n+1)}{\kappa^{\sigma+n+1}}, \tag{A.2}$$

with $g^{(n)}(0)$ the n-th derivative of $g(t)$ at $t = 0$. For $\sigma = 0$, the expression further simplifies to

$$I(\kappa) \sim \sum_{n=0}^{\infty} \frac{g^{(n)}(0)}{\kappa^{\sigma+n+1}}. \tag{A.3}$$

A similar reasoning for the following integral:

$$I(\kappa) = \int_{-\alpha}^{\beta} \mathrm{d}t \, \exp(-\kappa t^2) g(t), \tag{A.4}$$

where $\alpha, \beta > 0$ (and can be ∞), where $g(t)$ is an absolutely integrable function over the interval $[-\alpha, \beta]$, leads to

$$I(\kappa) \sim \sqrt{\frac{\pi}{\kappa}} \sum_{n=0}^{\infty} \frac{1}{2^{2n} n!} \frac{g^{(2n)}(0)}{\kappa^n}. \tag{A.5}$$

A.1.2 Laplace's method

Laplace's method provides asymptotic approximations of integrals with more general exponential functions in the integrand. Consider the integral

$$I(\kappa) = \int_{\alpha}^{\beta} \mathrm{d}t \, \exp(\kappa h(t)) g(t), \tag{A.6}$$

where $\alpha, \beta > 0$, $g(t)$ is an absolutely integrable function over the interval $[\alpha, \beta]$, and $h(t)$ is a real-valued function that is twice differentiable within the integration domain. Assume now that $h(t)$ reaches a maximum h_{max} at $t = t_{max} \in]\alpha, \beta[$. This also implies that $h'(t_{max}) = 0$ and $h''(t_{max}) < 0$[1]. Then,

$$I(\kappa) = \exp(\kappa h_{max}) \int_{\alpha}^{\beta} \mathrm{d}t \, \exp(\kappa (h(t) - h_{max})) g(t). \tag{A.7}$$

The term is $h(t) - h_{max}$ is negative. It is now mapped to the real axis as follows

$$-\mu^2 \equiv h(t) - h_{max} \approx \frac{h''(t_{max})}{2} (t - t_{max})^2, \tag{A.8}$$

in which a Taylor expansion for $h(t)$ at $t = t_{max}$ was introduced. It is clear that $\mu = 0$ corresponds to $t = t_{max}$. By choosing μ to be negative to correspond with $t < t_{max}$ and positive to correspond with with $t > t_{max}$, we obtain

[1] The following derivation can easily be adjusted if the maximum occurs at the boundary points $t = \alpha$ or $t = \beta$ [1].

$$\frac{\mathrm{d}t}{\mathrm{d}\mu} \approx \sqrt{\frac{-2}{h''(t_{max})}} \tag{A.9}$$

Introducing (A.8) and (A.9) into (A.7), and stretching the integration domain to the real axis, yields

$$I(\kappa) \approx \exp(\kappa h_{max}) \int_{-\infty}^{\infty} \mathrm{d}\mu \, \exp(-\kappa\mu^2) G(\mu), \tag{A.10}$$

where

$$G(\mu) = \sqrt{\frac{-2}{h''(t_{max})}} g(t(\mu)).$$

(A.10) now satisfies the requirements of Watson's lemma (A.5). If only the highest order term in κ is retained, the approximation becomes

$$I(\kappa) \sim \exp(\kappa h_{max}) g(t_{max}) \kappa^{-1/2} \sqrt{\frac{-2\pi}{h''(t_{max})}}. \tag{A.11}$$

A.1.3 Method of steepest descent

The method of steepest descent (STD) concerns the asymptotic approximation of integrals over a path in the complex plane. Consider the integral

$$I(\kappa) = \int_{\gamma} \mathrm{d}z \, \exp(\kappa h(z)) g(z), \tag{A.12}$$

where $g(z)$ and $h(z)$ are complex valued functions and γ is a path that connects $z = z_0$ with $z = z_1$ (z_0 and z_1 coincide if γ is a closed contour). $h(z) = u(z) + jv(z)$ is holomorphic in an open domain Ω, with $\gamma \subset \Omega$. $g(z)$ is allowed to have a number of simple poles z_{p_k} ($k = 1, \ldots, N_p$) in $\Omega \setminus \gamma$. Except for these simple poles, $g(z)$ is holomorphic in Ω.
The integration path can be mapped to the real axis by introducing a new variable t such that $z = z(t)$ with $t \in [\alpha, \beta]$. Obviously, $z(\alpha) = z_0$ and $z(\beta) = z_1$.
If the imaginary part of $h(z)$ remains constant along γ, i.e. $v(z) \equiv v_0 \; \forall z \in \gamma$, then

$$I(\kappa) = \exp(j\kappa v_0) \int_{\alpha}^{\beta} \mathrm{d}t \, \exp(\kappa u(z(t))) G(t), \tag{A.13}$$

where

$$G(t) = g(z(t))z'(t).$$

The function $u(z(t))$ is bounded on the interval $[\alpha, \beta]$ because of the holomorphicity of $h(z)$. If the maximum of $u(z)$, u_{max}, is reached at $t_{max} \in]\alpha, \beta[$ and $z_{max} = z(t_{max})$, then the integral in (A.13) can be approximated by Laplace's method, such that

$$I(\kappa) \sim \exp(\kappa h(z_{max}))g(z_{max})\kappa^{-1/2}\sqrt{\frac{-2\pi}{r''(z_{max})}}. \tag{A.14}$$

The most general case, with $v(z)$ not a constant, has to be treated on an individual basis. However, based on the previous asymptotic approximation, some guidelines become apparent. Suppose that the path γ could be deformed into a path $\gamma' \subset \Omega$, along which $v(z)$ is constant, then the above procedure could be repeated for path γ'. This is possible due to the residue theorem, which states that for an analytic function in the domain enclosed by contour $\mathcal{C}$, except for P simple poles at z_i $(i = 1, \ldots, P)$, the integral over the contour becomes[2]

$$\oint_{\mathcal{C}} \mathrm{d}z\, f(z) = 2\pi j \sum_{n=1}^{P} \mathrm{Res}(f, z_n), \tag{A.15}$$

where

$$\mathrm{Res}(f, z_n) = \lim_{z \to z_n} (z - z_n) f(z). \tag{A.16}$$

Thus, if $\mathcal{C} = \gamma \cup \gamma'$, the integrals over γ and γ' are connected through (A.15). In general, one path will not be sufficient to ensure that $v(z)$ remains constant between $z = z_0$ and $z = z_1$. This is obviously the case when $v(z_0) \neq v(z_1)$. The contour is then deformed into a set of contiguous paths, and for each path either $v(z)$ or $u(z)$ remains constant. Often, the paths with constant $u(z) = u_0$ are chosen so that u_0 is large in amplitude and negative. Consequently, the contributions of these paths are negligible and can be discarded.
Due to the Cauchy-Riemann equations for holomorphic functions, the gradients of $u(x, y)$ and $v(x, y)$ are perpendicular for every $z = x + jy \in \Omega$. This implies that along a path with constant $v(x, y)$, $u(x, y)$ changes at a maximal rate. If the path is transversed in the direction opposite to the gradient of $u(x, y)$, the path is called the *steepest descent path* (SDP).
Many exponential integrals are defined on contours $\mathcal{C}$ without endpoints, either

[2]It is assumed $\mathcal{C}$ is traversed counter-clockwise.

because the contour is closed or because its endpoints tend to infinity. In the absence of endpoints, the asymptotic contributions all stem from the neighborhoods of maxima of $u(x, y)$. These maxima correspond to the critical points of $h(z)$, i.e. points for which $h'(z) = 0$ due to the Cauchy-Riemann equations. Critical points of $h(z)$, $z \in \Omega$, are *saddle points* of $u(x, y)$ and $v(x, y)$, i.e. they are not local extrema of $u(x, y)$ or $v(x, y)$. In practice, the contours are deformed to pass through the critical points, in the direction of steepest descent. The integral can then be approximated by (A.14).

A.1.4 Modified Pauli-Clemmow method of steepest descent

Up to now, the asymptotic approximations of Sec. A.1.2 and Sec. A.1.3 have been derived for smooth $g(z)$ at the critical points of $h(z)$. Integrals of the form (A.13), when $g(z)$ becomes singular in the neighborhood of a critical point of $h(z)$, can be treated with the Pauli-Clemmow modified STD (PCM). Consider the exponential integral (A.13), where

- $h(z)$ has a critical point at $z = z_s$, i.e. $h'(z_s) = 0$, $h''(z) \neq 0$.
- $g(z)$ has a simple pole at $z = z_p$, with z_p in the neighborhood of z_s.

Along the path of steepest descent, the function $h(z)$ can be mapped onto the real axis through $h(z) = h(z_s) - s^2$, $s \in \mathbb{R}$. The integration with relation to the new variable s is extended to the entire real axis. Thus,

$$I(\kappa) \sim \exp(\kappa h(z_s)) \int_{-\infty}^{\infty} \mathrm{d}s\, g(z(s)) \frac{\mathrm{d}z}{\mathrm{d}s} \exp(-\kappa s^2). \tag{A.17}$$

The Pauli-Clemmow method approximates the function $g(z(s))\, dz/ds$ by a product of a function that takes the singular behavior at $z = z_p \equiv z(s_p)$ into account and an analytic function $f(s)$, i.e.

$$g(z(s)) \frac{\mathrm{d}z}{\mathrm{d}s} = \frac{f(s)}{s - s_p}. \tag{A.18}$$

$f(s)$ is expanded into a Taylor series around $s = 0$,

$$f(s) = \sum_{n=0}^{\infty} a_n s^n. \tag{A.19}$$

Introducing (A.18) and (A.19) into (A.17) and multiplication of nominator and denominator in the integrand with $s + s_p$, yields

$$I(\kappa) \sim \exp(\kappa h(z_s)) \sum_{n=0}^{\infty} a_n \int_{-\infty}^{\infty} \mathrm{d}s\, s^n \frac{s+s_p}{s^2-s_p^2} \exp(-\kappa s^2). \tag{A.20}$$

Note that the integrand in (A.20) vanishes for uneven powers of s. Retaining only the term for $n = 0$,

$$I(\kappa) \sim \exp(\kappa h(z_s)) s_p a_0 \int_{-\infty}^{\infty} \mathrm{d}s\, \frac{\exp(-\kappa s^2)}{s^2-s_p^2}. \tag{A.21}$$

a_0 is given by

$$a_0 = \lim_{s\to 0} g(z(s)) \frac{\mathrm{d}z}{\mathrm{d}s}(s-s_p) \approx -s_p g(z_s) \left| \sqrt{\frac{-2}{h''(z_s)}} \right| \exp(j\phi_s), \tag{A.22}$$

where a similar approximation as in (A.9) is introduced and $\exp(j\phi_s)$ is a phase factor corresponding to the square root function. The remaining integrand, i.e.

$$A(\kappa) \equiv \int_{-\infty}^{\infty} \mathrm{d}s\, \frac{\exp(-\kappa s^2)}{s^2-s_p^2}, \tag{A.23}$$

can be written in terms of the well-known Fresnel function. Thereto, s_p^2 is replaced by $-j\alpha$, such that

$$A(\kappa) = \exp(j\kappa\alpha) \int_{-\infty}^{\infty} \mathrm{d}s\, \frac{\exp(-\kappa(s^2+j\alpha))}{s^2+j\alpha}. \tag{A.24}$$

Note that

$$\begin{aligned} \frac{\mathrm{d}}{\mathrm{d}\kappa} A(\kappa)\exp(-j\kappa\alpha) &= -\exp(-j\kappa\alpha) \int_{-\infty}^{\infty} \mathrm{d}s\, \exp(-\kappa s^2) \\ &= -\sqrt{\frac{\pi}{\kappa}} \exp(-j\kappa\alpha). \end{aligned} \tag{A.25}$$

Integration over κ results in

$$\int_{\kappa}^{\infty} \mathrm{d}\kappa' \frac{\mathrm{d}}{\mathrm{d}\kappa'} [A(\kappa')\exp(-j\kappa'\alpha)] = -\sqrt{\pi} \int_{\kappa}^{\infty} \mathrm{d}\kappa' \frac{\exp(-j\kappa'\alpha)}{\sqrt{\kappa'}}. \tag{A.26}$$

Since $A(\infty) = 0$, this leads to

$$A(\kappa) = \sqrt{\pi\alpha} \exp(j\kappa\alpha) \int_{\kappa}^{\infty} \mathrm{d}\kappa' \frac{\exp(-j\kappa'\alpha)}{\sqrt{\kappa'\alpha}}. \tag{A.27}$$

The integration variable is changed to τ, with $\tau^2 = \alpha\kappa'$, such that

$$A(\kappa) = \frac{1}{j\alpha}\sqrt{\frac{\pi}{\kappa}}F\big(\pm\sqrt{\kappa\alpha}\big), \tag{A.28}$$

where

$$F(z) = 2jz\exp(jz^2)\int_z^\infty \mathrm{d}\tau\ \exp(-j\tau^2). \tag{A.29}$$

The branch cut for the square root in (A.28) must be chosen along the positive imaginary axis. The plus sign must be used for $-3\pi/4 < \arg\sqrt{\alpha} < \pi/4$ and the minus sign for $\pi/4 < \arg\sqrt{\alpha} < 5\pi/4$ [3].
The integral in the last expression is the well-known Fresnel integral and efficient schemes exist for its computation [4]. For complex arguments, the Fresnel integral can be computed using the error function, through [5]

$$\int_\zeta^\infty \mathrm{d}\tau\ \exp(-j\tau^2) = \sqrt{\frac{\pi}{2}}\frac{1-j}{2}\left[1-\mathrm{erf}\left(\frac{1+j}{\sqrt{2}}\zeta\right)\right], \tag{A.30}$$

where the error function $\mathrm{erf}(z)$ is

$$\mathrm{erf}(z) = \frac{2}{\sqrt{\pi}}\int_0^z \mathrm{d}\tau\ \exp(-\tau^2). \tag{A.31}$$

Introducing (A.22) and (A.28) into (A.21), the following asymptotic PCM approximation for $I(\kappa)$ is finally obtained:

$$I(\kappa) \sim \exp(\kappa h(z_s))g(z_s)\left|\sqrt{\frac{-2\pi}{\kappa h''(z_s)}}\right|\exp(j\phi_s)F(\pm\sqrt{\kappa\alpha}), \tag{A.32}$$

A.2 UTD diffraction coefficient for an impenetrable wedge

Consider an impenetrable wedge with opening angle ψ of Fig. A.1. The Green's function in the presence of the wedge is given by [6]

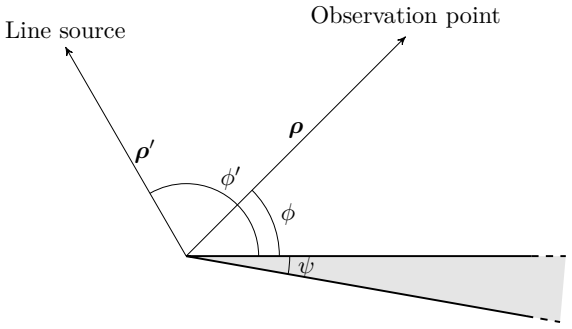

Figure A.1: Geometry of an impenetrable wedge.

$$\begin{aligned} G_{s,h}(\boldsymbol{\rho};\boldsymbol{\rho}') &= -\frac{j}{4\nu}\sum_{m=0}^{\infty}\epsilon_m J_{m/\nu}(k\rho'_<)H_0^{(2)}(k\rho_>)\Big[\cos\Big(\frac{m}{\nu}(\phi-\phi')\Big) \\ &\quad \pm\cos\Big(\frac{m}{\nu}(\phi+\phi')\Big)\Big] \\ &\equiv u(\rho,\rho',\beta^-)\pm u(\rho,\rho',\beta^+) \end{aligned} \tag{A.33}$$

where k is the wavenumber, $\rho'_< = \min(\rho,\rho')$, $\rho'_> = \max(\rho,\rho')$ and $\psi = (2-\nu)\pi$. Also, $\epsilon_m = 1$ if $m = 0$ and $\epsilon_m = 2$ otherwise. The series converges uniformly for $\rho \neq \rho'$. The minus sign is used when Dirichlet boundary conditions apply at the surface of the wedge, and the plus sign when Neumann boundary conditions apply. Further, $\beta^\pm = \phi \pm \phi'$.
An equivalent integral form is [7]

$$\begin{aligned} u(\rho,\rho',\beta^\pm) = \frac{1}{4\pi^2\nu}\int_{\Gamma-\Gamma'}\mathrm{d}t\,\frac{1}{2j}\cot\Big(\frac{\xi+\beta^\pm}{2\nu}\Big) \\ \cdot K_0\Big(jk\sqrt{\rho^2+\rho'^2-2\rho\rho'\cos\xi}\Big), \end{aligned} \tag{A.34}$$

where the zeroth-order modified cylindrical Bessel function of the second kind K_0 is given by

$$K_0(z) = \frac{j\pi}{2}\begin{cases} H_0^{(2)}(jz), & -\pi \le \arg(z) \le \pi/2 \\ -H_0^{(2)}(-jz), & -\pi/2 \le \arg(z) \le \pi \end{cases} \tag{A.35}$$

and the integration path is shown in Fig. A.2.

The large argument expansion (2.29) is now introduced into (A.34), which yields

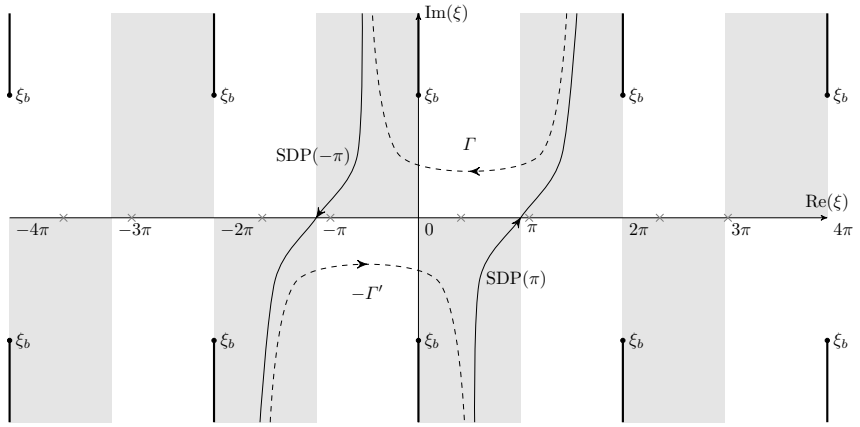

Figure A.2: The complex ξ-plane. The poles indicated by crosses ($\times$) correspond to parameters $\psi = 10^{\circ}$, $\phi' = 60^{\circ}$ and $\phi = 135^{\circ}$.

$$u(\rho,\rho',\beta^{\pm}) \approx \frac{1}{8j\pi^2\nu}\int_{\Gamma-\Gamma'} \mathrm{d}t\, \cot\left(\frac{\xi+\beta^{\pm}}{2\nu}\right) \cdot\sqrt{\frac{\pi}{2jk(\rho^2+\rho'^2-2\rho\rho'\cos\xi)^{1/2}}}\exp\left(-jk\big(\rho^2+\rho'^2-2\rho\rho'\cos\xi\big)^{1/2}\right). \quad \text{(A.36)}$$

The exponential is approximated by

$$\begin{aligned}&\exp\left(-jk\big(\rho^2+\rho'^2-2\rho\rho'\cos\xi\big)^{1/2}\right)\\ &= \exp\left(-jk\big((\rho+\rho')^2-2\rho\rho'(1+\cos\xi)\big)^{1/2}\right)\\ &\approx \exp\left(-jk(\rho+\rho')\right)\exp\left(jk\frac{\rho\rho'}{\rho+\rho'}(1+\cos\xi)\right).\end{aligned} \quad \text{(A.37)}$$

The above approximation will be justified shortly. Through this approximation, the integral (A.36) is in the proper form (A.12) for evaluation by STD, with

$$\begin{aligned}\kappa &\to k\frac{\rho\rho'}{\rho+\rho'}\\ h(z) &\to h(\xi) = j(1+\cos\xi)\\ g(z) &\to g(\xi) = \sqrt{\frac{\pi}{2jk(\rho^2+\rho'^2-2\rho\rho'\cos\xi)^{1/2}}}\cot\left(\frac{\xi+\beta^{\pm}}{2\nu}\right)\exp\left(-jk(\rho+\rho')\right)\end{aligned}$$

The critical points are the zeros of $h'(\xi) = -\sin\xi$, i.e. $\xi = l\pi$, with $l \in \mathbb{Z}$. Using this, together with the information about the integration path $\Gamma - \Gamma'$ in Fig. A.2, a good choice seems to be the integration over the SDPs at $\xi = \pi$ and $\xi = -\pi$, deforming the SDPs so that they asymptotically coincide with path $\Gamma - \Gamma'$. Note that in the neighborhood of the critical points, $\cos\xi \approx -1$, justifying the approximation in (A.37).
The resulting contour $\mathcal{C} = \Gamma \cup \mathrm{SDP}(-\pi) \cup -\Gamma' \cup \mathrm{SDP}(\pi)$ is closed and Cauchy's theorem can be employed. The function $u(\rho, \rho', \beta^{\pm})$ is thus also given by

$$u(\rho, \rho', \beta^{\pm}) \approx 2j\pi \sum_{\xi_k} \mathrm{Res}(g(\xi)\exp(h(\xi)), \xi_k) - u_{\mathrm{SDP}(-\pi)}(\rho, \rho', \beta^{\pm}) \\ - u_{\mathrm{SDP}(\pi)}(\rho, \rho', \beta^{\pm}).$$

$g(z)$ exhibits poles at the zeros ξ_b of the denominator square root function's argument. From there, branch cuts parallel to the imaginary axis must be introduced, as shown in Fig. A.2. These poles do not contribute to the integration over the contour $\mathcal{C}$. Furthermore, $g(z)$ has simple poles due to the cotangens function, i.e.

$$\frac{\xi_p + \beta^{\pm}}{2\nu} = N\pi \Leftrightarrow \xi_p = -\beta^{\pm} + 2\nu N\pi,\ N \in \mathbb{Z}. \tag{A.38}$$

The corresponding residues are

$$-\frac{j}{4}\sqrt{\frac{2j}{\pi k(\rho^2 + \rho'^2 - 2\rho\rho'\cos\left(-\beta^{\pm} + 2\nu N\pi\right))^{1/2}}} \\ \exp\left(-jk(\rho + \rho')\right) H(\pi - \left|-\beta^{\pm} + 2\nu N\pi\right|), \tag{A.39}$$

where $H(.)$ is the Heaviside function, ensuring that the residue is only taken into account if the pole resides inside the contour. Only for the pole $N = 0$ the Heaviside is possibly non-zero. Thus, the only pole contributions are

$$-\frac{j}{4}\sqrt{\frac{2j}{\pi k(\rho^2 + \rho'^2 - 2\rho\rho'\cos\beta^{\pm})^{1/2}}}\exp\left(-jk(\rho + \rho')\right) H(\pi - \left|\beta^{\pm}\right|). \tag{A.40}$$

From (2.29), the residue contribution for β^{-} can also be identified with the large argument expansion of the incoming field. The contribution for β^{+} corresponds to the large argument expansion of the reflected field. Equipped with this information, (A.33) becomes

$$\begin{aligned} G_{s,h}(\boldsymbol{\rho};\boldsymbol{\rho}') \approx G^{inc}(\boldsymbol{\rho};\boldsymbol{\rho}') + G^{refl}(\boldsymbol{\rho};\boldsymbol{\rho}') \\ + \big[- u_{\mathrm{SDP}(\pi)}(\rho,\rho',\beta^-) - u_{\mathrm{SDP}(-\pi)}(\rho,\rho',\beta^-) \\ \pm \big(-u_{\mathrm{SDP}(\pi)}(\rho,\rho',\beta^+) - u_{\mathrm{SDP}(-\pi)}(\rho,\rho',\beta^+)\big)\big], \end{aligned} \tag{A.41}$$

i.e. the Green's function consists of three contributions within this approximation: the incoming field, the reflected field and a remaining term. The last term will be found to be related to diffraction and will be denoted $G^{diff}_{s,h}(\boldsymbol{\rho};\boldsymbol{\rho}')$. Depending on the distance of the poles in (A.38) from the critical points $\xi = \pm\pi$, it may be justified to use traditional STD to obtain an approximation of the integrals over the SDPs. At *transition regions*, however, the poles are near the critical points and via the STD approximation, the GTD diffraction coefficients are obtained that are singular at these transition regions. Therefore, we will use PCM to obtain uniform diffraction coefficients that remain accurate at the transition regions. The pole that is closest to one of the critical points $\xi = \pm\pi$ corresponds to the integer $N^{\pm}$ that most closely satisfies the following relation:

$$N^{\pm} = \frac{\pm\pi + \beta}{2\pi\nu}. \tag{A.42}$$

Some interesting values for the use of the PCM method are:

$$\begin{aligned} h(\pm\pi) &= 0 \\ g(\pm\pi) &= \sqrt{\frac{\pi}{2jk(\rho+\rho')}}\cot\left(\frac{\pm\pi+\beta}{2\nu}\right)\exp\left(-jk(\rho+\rho')\right) \\ h''(\pm\pi) &= j \\ \phi_s(\pi) &= \pi/4,\ \phi_s(-\pi) = -3\pi/4 \\ \alpha^{\pm}(\beta) &= j(h(\pm\pi) - h(\xi_p)) = 1 + \cos(\xi_p) = 2\cos^2\left(\frac{2\nu N^{\pm}\pi - \beta}{2}\right) \end{aligned}$$

Hence, approximating $G^{diff}(\boldsymbol{\rho};\boldsymbol{\rho}')$ with PCM, yields

$$G_{s,h}^{diff}(\boldsymbol{\rho};\boldsymbol{\rho}') \sim -\frac{1}{8j\pi^2\nu}\sqrt{\frac{\pi}{2jk(\rho+\rho')}}e^{-jk(\rho+\rho')}\sqrt{\frac{2\pi(\rho+\rho')}{k\rho\rho'}}$$
$$\Bigg[\cot\left(\frac{\pi+\beta^-}{2\nu}\right)e^{j\frac{\pi}{4}}F(kL\alpha^+(\beta^-)) + \cot\left(\frac{-\pi+\beta^-}{2\nu}\right)e^{-j\frac{3\pi}{4}}F(kL\alpha^-(\beta^-))$$
$$\pm\Bigg(\cot\left(\frac{\pi+\beta^-}{2\nu}\right)e^{j\frac{\pi}{4}}F(kL\alpha^+(\beta^-))$$
$$+\cot\left(\frac{-\pi+\beta^-}{2\nu}\right)e^{-j\frac{3\pi}{4}}F(kL\alpha^-(\beta^-))\Bigg)\Bigg], \tag{A.43}$$

where $L = \rho\rho'/(\rho+\rho')$. After introduction of the high-frequency approximation for the incoming field at the tip

$$G_{far}^{inc}(0;\boldsymbol{\rho}') \sim -\frac{j}{4}\sqrt{\frac{2j}{\pi k}}\frac{e^{-jk\rho'}}{\sqrt{\rho'}} \tag{A.44}$$

into (A.43) and some rearrangement of terms, one gets the well-known UTD solution

$$G_{s,h}^{diff}(\boldsymbol{\rho};\boldsymbol{\rho}') = G_{far}^{inc}(0;\boldsymbol{\rho}')D_{s,h}\frac{e^{-jk\rho}}{\sqrt{\rho}} \tag{A.45}$$

with

$$D_{s,h} = -\frac{\exp(-j\pi/4)}{2\nu\sqrt{2\pi k}}$$
$$\Bigg[\cot\left(\frac{\pi+\beta^-}{2\nu}\right)F(kL\alpha^+(\beta^-)) + \cot\left(\frac{\pi-\beta^-}{2\nu}\right)F(kL\alpha^-(\beta^-))$$
$$\pm\left(\cot\left(\frac{\pi+\beta^+}{2\nu}\right)F(kL\alpha^+(\beta^+)) + \cot\left(\frac{\pi-\beta^+}{2\nu}\right)F(kL\alpha^-(\beta^+))\right)\Bigg]. \tag{A.46}$$

References

[1] P. D. Miller, *Applied Asymptotic Analysis (Graduate Studies in Mathematics)*. American Mathematical Society, 2006.

[2] D. Bouche, F. Molinet, and R. Mittra, *Asymptotic Methods in Electromagnetics*. Springer-Verlag Berlin Heidelberg, 1997.

[3] P. C. Clemmow, *The Plane Wave Spectrum Representation of Electromagnetic Fields*. Pergamon Press, 1966.

[4] K. D. Mielenz, "Computation of Fresnel integrals. II", *Journal of Research of the National Institute of Standards and Technology*, vol. 105, no. 4, pp. 589–590, 2000.

[5] *NIST Digital Library of Mathematical Functions*, http://dlmf.nist.gov/, Release 1.0.5 of 2012-10-01. [Online]. Available: `http://dlmf.nist.gov/`.

[6] J. G. Van Bladel, *Electromagnetic Fields, 2nd edition*. Wiley-IEEE press, 2007.

[7] P. Pathak and R. Kouyoumjian, "The Dyadic Diffraction Coefficient for a Perfectly Conducting Wedge", Electroscience Laboratory at the Ohio State University, Tech. Rep., 1970.